# DETERMINATION VIA COMPUTATIONAL MODELING OF THE STRUCTURE-PROPERTIES RELATIONSHIPS IN INTERCLATED POLYMER:FULLERENE BLENDS FOUND IN BULK-HETEROJUNCTION SOLAR CELLS

A Dissertation
Presented to
The Academic Faculty

by

Eunkyung Cho

In Partial Fulfillment
of the Requirements for the Degree
Doctor of Philosophy in the
School of Materials and Science Engineering

Georgia Institute of Technology
December 2012

# DETERMINATION VIA COMPUTATIONAL MODELING OF THE STRUCTURE-PROPERTIES RELATIONSHIPS IN INTERCLATED POLYMER:FULLERENE BLENDS FOUND IN BULK-HETEROJUNCTION SOLAR CELLS

Approved by:


Dr. Jean-Luc Brédas, Advisor
School of Chemistry and Biochemistry
*Georgia Institute of Technology*

Dr. Seung Soon Jang
School of Materials Science and Engineering
*Georgia Institute of Technology*

Dr. Haskell W. Beckham, Co-Advisor
School of Materials Science and Engineering
*Georgia Institute of Technology*

Dr. Yonathan S. Thio
School of Chemical and Biomolecular Engineering
*Georgia Institute of Technology*

Dr. David G. Bucknall
School of Materials Science and Engineering
*Georgia Institute of Technology*



Date Approved: November 06, 2012

# ACKNOWLEGMENTS

First and foremost, I would like to express my respectful gratitude to my advisor, Prof. Jean-Luc Brédas, for his support, helpful guidance, valuable scientific insight, and enthusiastic encouragement throughout the research. I was fortunate to have him as my advisor and it was an absolute pleasure to work with him. I also would like to thank my committee members, Prof. Haskell W. Beckham, Prof. David G. Bucknall, Prof. Seung Soon Jang, and Prof. Yonathan S. Thio, for their support and advice.

I would like to extend my thanks and appreciation to collaborators, Prof. Dag W. Breiby, Dr. R. Joseph Kline, Dr. Michael F. Toney, Dr. Roman Gysel, Dr. Nichole Cates Miller, Sean Sweetman, Prof. Michael D. McGehee, Prof. Bradley F. Chmelka, and Dr. Denis Andrienko, for their tremendous efforts, discussions, and cooperation with me. Furthermore, I would like to express my gratitude to all of the group members (Bredators), past and present, for their friendships and great working environment as well as helpful discussions. My special sincere thanks go to Dr. Veaceslav Coropceanu, Dr. Chad Risko, and, Dr. Hong Li for their insightful discussions, suggestions, and assistance. I am also thankful to Dawn Franklin and Ginelle Tingler for all their kind assistance.

Finally, I would like to thank my husband, Seokwon Jung, my little son, Daniel Jihoon Jung, my family, and my friends for their endless love, continued support, and belief in me.

# TABLE OF CONTENTS

Page

# LIST OF TABLES

Page

# LIST OF FIGURES

Page

# LIST OF ABBREVIATIONS

| | |
|---|---|
| A | Electron Acceptor |
| AP | Adiabatic Potential |
| AEA | Adiabatic Electron Affinity |
| BHJ | Bulk-heterojunction |
| CG | Coarse Grained |
| CT | Charge Transfer |
| D | Electron Donor |
| D/A | Donor-Acceptor |
| DFT | Density Functional Theory |
| DFTB | Density Functional-based Tight Binding |
| EA | Electron Affinity |
| FF | Force Field |
| GGA | Generalized-Gradient Approximation |
| GIXD | Grazing Incidence X-ray Diffraction |
| GMH | Generalized Mulliken-Hush |
| HF | Hartree-Fock |
| HOMO | Highest Occupied Molecular Orbital |
| $IC_{60}BA$ | Indene-$C_{60}$-Bis Adduct |
| $IC_{60}MA$ | Indene-$C_{60}$-Mono Adduct |
| IR | Infra-red |
| ITO | Indium Tin Oxide |

| | |
|---|---|
| LC | Liquid Crystalline |
| LDA | Local Density Approximation |
| LJ | Lennard-Jones |
| LUMO | Lowest Unoccupied Molecular Orbital |
| MD | Molecular Dynamics |
| MDMO-PPV | poly(2-methoxy-5-(3′,7′-dimethyloctyloxy)-p-phenylene vinylene) |
| MM | Molecular Mechanics |
| NEXAFS | Near Edge X-ray Absorption Fine Structure |
| NM | Normal Mode |
| NMR | Nuclear Magnetic Resonance |
| ODCB | *o*-dichlorobenzene |
| ODF | Orientational Distribution Functions |
| OFET | Organic Field-Effect Transistor |
| OTFT | Organic Thin-Film Transistor |
| OPV | Organic Photovoltaics |
| PAW | Projector-Augmented Wave |
| PBM | Phenyl Butyric acid Methyl ester |
| PBTTT- $C_n$ | Poly (2,5-bis (3–alkylthiophene–2–yl) thieno[3,2-b]thiophene) |
| $PC_{61}BM$ | [6,6]-phenyl-$C_{61}$-butyric acid methyl ester |
| $PC_{71}BM$ | [6,6]-phenyl-$C_{71}$-butyric acid methyl ester |
| PCE | Power Conversion Efficiency |
| PCM | Polarizable Continuum Model |
| QEq | Charge Equilibration |

| | |
|---|---|
| QM | Quantum Mechanics |
| rr-P3HT | Regioregular poly(3-hexylthiophene) |
| TDDFT | Time-Dependent Density Functional Theory |
| UFF | Universal Force Field |
| VEA | Vertical Electron Affinity |
| XRD | X-Ray Diffraction |

# SUMMARY

The intrinsic performance of a polymer-based bulk-heterojunction (BHJ) solar cell is principally influenced by the molecular-scale packing formed through the blending of electron-donor polymers and fullerene acceptor molecules, as well as the intrinsic properties of each component. An intriguing example of such mixing is the intercalation of fullerene molecules amongst the side chains of the donor polymers, which leads to a bimolecular crystal that significantly affects the film nanostructure.

In this dissertation, we use a number of computational methods, ranging from quantum mechanics through molecular mechanics and molecular dynamics along with X-ray diffraction simulations, to investigate the structure-property relationships of intercalated polymer:fullerene blends. Chapter 1 provides a brief overview of the polymer:fullerene blend system and its use in bulk-heterojunction solar cells. Chapter 2 presents a review of the computational methodologies used in this dissertation, from quantum mechanics (*e.g.*, Hartree-Fock theory and Density Functional Theory) through atomistic molecular mechanics and dynamics simulations as well as the general concepts and simulations of grazing incidence X-ray diffraction (GIXD) patterns.

We then turn to the main results of the dissertation. Chapter 3 discusses the molecular packing structure and electronic properties of the highly-oriented polymer, poly (2,5-bis (3–alkyl thiophene–2–yl) thieno [3,2-b] thiophene) (PBTTT), as a function of alkyl side-chain length. Chapter 4 deals with the determination of the relationship between detailed

packing structure and electronic properties in a polymer:fullerene blend formed between PBTTT and the substituted fullerene, phenyl-$C_{71}$-butyric acid methyl ester ($PC_{71}BM$). Chapter 5 focuses on the vibrational properties of the pristine polymer and a series of derivatized fullerenes, as well their redox and optical properties. Finally, a synopsis of the work and further considerations are given in Chapter 6.

# CHAPTER 1

# INTRODUCTION

## 1.1 Organic photovoltaics (OPV)

The photovoltaic process, in which the optical energy supplied by the sun is converted into electrical energy, has been widely recognized as an attractive renewable energy source. Organic-based photovoltaics (OPV) that make use of organic semiconductors have numerous potential advantages compared to traditional silicon-based photovoltaics, including: low production costs, ease of processing, flexible forms, and light-weight devices.[1,2] Moreover, the optical and electrical properties of the device can be readily changed by modifying the chemical and electronic structures of the organic materials and/or the processing methods/conditions, such as solution deposition vs vapor deposition/solvent, thermal annealing, and solution concentration.[3,4] The OPV process has been extensively investigated through both experimental and theoretical approaches to understand the underlying physical mechanisms and optimize device performance.[5-7]

### 1.1.1 Device architecture

The general structure of an OPV cell generally consists of a transparent electrode as an anode (typically indium-tin oxide (ITO)) coated on a (glass) substrate, an active layer made from two different organic semiconductors, and a second electrode as a cathode (generally aluminum), Figure 1.1. The active layer contains an electron-donor (D) molecule or polymer with a low ionization potential and an electron-acceptor (A)

molecule or polymer with a high electron affinity. The two main geometries generally considered for the active layer in an OPV are the i) bilayer and ii) bulk-heterojunction (BHJ) architectures, which are determined by how the electron donor and acceptor materials are processed, Figure 1.1. The interface between the two materials plays an important role in determining the efficiency of charge separation. A bilayer device has a single interface between distinct layers of donor and acceptor, which generally leads to limited charge separation and rather low efficiency devices. In a bulk-heterojunction (BHJ) device, on the other hand, there exists an interpenetrating and bicontinuous network of the donor and acceptor phases, which maximizes interfacial area and can improve device performance.[7,8]

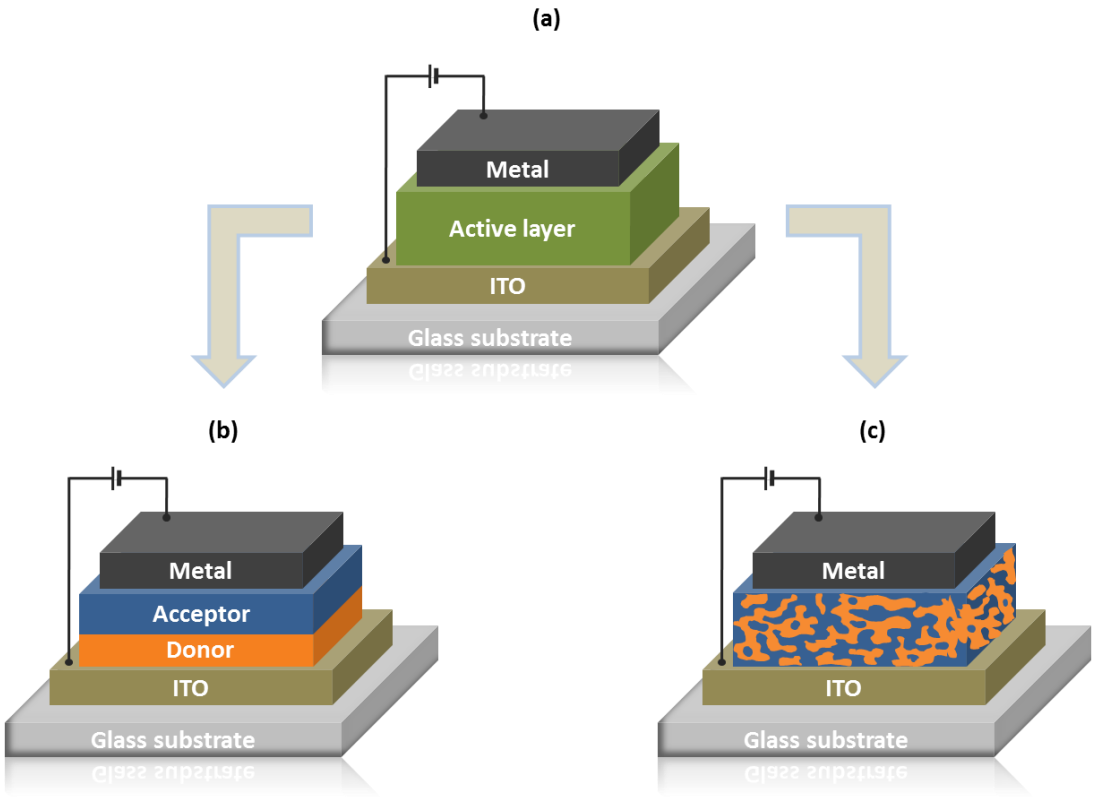


Figure 1.1 Schematic structure of (a) an general organic photovoltaic cell, (b) a bilayer device, and (c) a bulk-heterojunction device.

### 1.1.2 Electronic processes

The fundamental electronic processes in organic solar cells include (i) photon absorption and exciton formation, (ii) exciton migration, (iii) interfacial exciton dissociation, (iv) charge migration, and (v) charge collection.[9] As shown in Figure 1.2, photons absorbed inside the active layers excite the donor (or the acceptor), leading to the creation of an exciton, i.e., a bound electron-hole pair with a typical binding energy on the order of a few tenths of an eV. The absorption spectrum of the active layer determines the generated photocurrent density. The excitons diffuse within the donor phase to the donor-acceptor (D/A) interface where they can dissociate into negative (electron) and positive (hole) charges. The amount of excitons that can reach the D/A interface is characterized by the exciton diffusion length (in general 5-10 nm in typical conjugated polymer)[10,11] and the location where excitons are created with respect to the nearest dissociation center. At the D/A interface, the dissociated charges need to overcome the Coulombic potential binding them together in order to be separated into free charge carriers. The separated free electrons and holes can then migrate through acceptor and donor domains towards the electrodes where they are collected to produce the photocurrent. However, there are several processes after photoexcitation, such as exciton recombination or charge trapping, that can prevent the electrons and holes from being collected at the electrodes, leading to a decrease in the device performance.

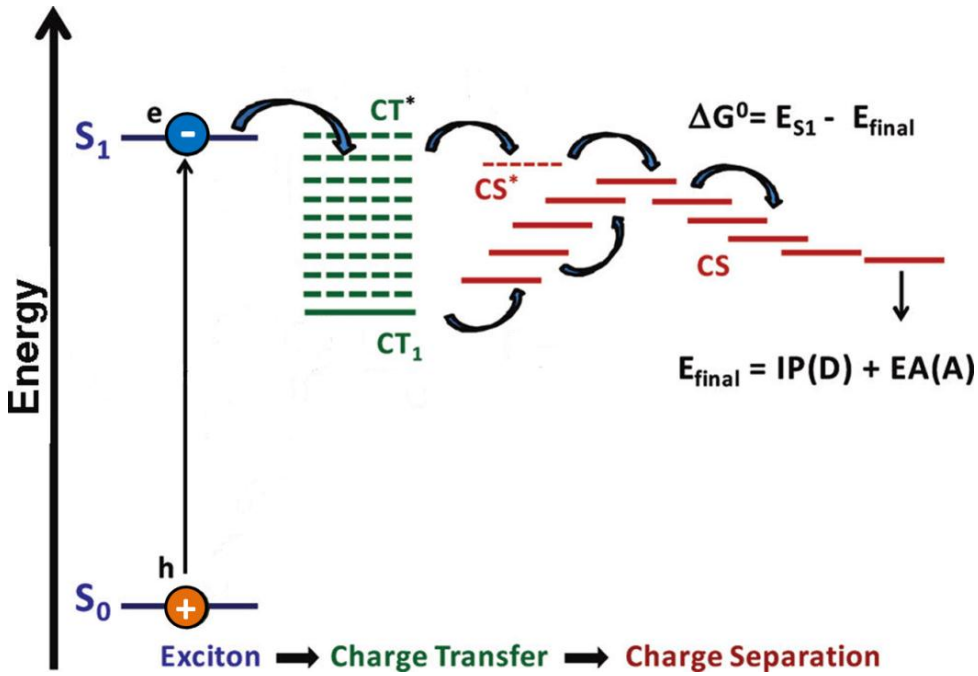


Figure 1.2 Schematic diagram of electronic state describing operation processes in an organic photovoltaic cell. $S_0$ and $S_1$ denote the singlet ground state and the first singlet excited state of materials, respectively. At the D/A interface, intermolecular charge transfer leads to charge-transfer (CT) states, where the hole (h) is on donor materials and the electron (e) is on acceptor materials. $CT_1$ represents the lowest energy charge-transfer state and $CT^*$ represents excited levels of the CT/CS manifolds. The final state is a charge-separated state (CS), where the hole in the donor layer and the electron in the accepter layer are free from one another. IP(D) and EA(A) represent ionization potential of the donor and electron affinity of the acceptor, respectively. This figure is adapted from the literature.[6]

While there are five steps that determine the operation of OPVs, the actual physical mechanisms governing these processes are still not completely understood. Nevertheless, it is clear that the performance of an organic photovoltaic cell is influenced by not only the intrinsic properties of the individual organic semiconductors, but also the interfacial morphology and supra-molecular organization introduced by how the materials interact and assemble at the interface.

### 1.1.3 Device performance

The performance of the organic photovoltaics can be characterized by three main parameters as:

$$PCE = \frac{V_{oc}J_{sc}FF}{P_{in}} \quad (1.1)$$

where PCE, the power conversion efficiency, represents the efficiency of the cell under illumination by the standard light source (A.M. 1.5) described by the amount of power produced by a solar cell relative to the incident power ($P_{in}$). $V_{oc}$, $J_{sc}$, and FF are open-circuit voltage, short-circuit current, and fill factor, respectively, determined from the illuminated J-V curve as shown in Figure 1.3.

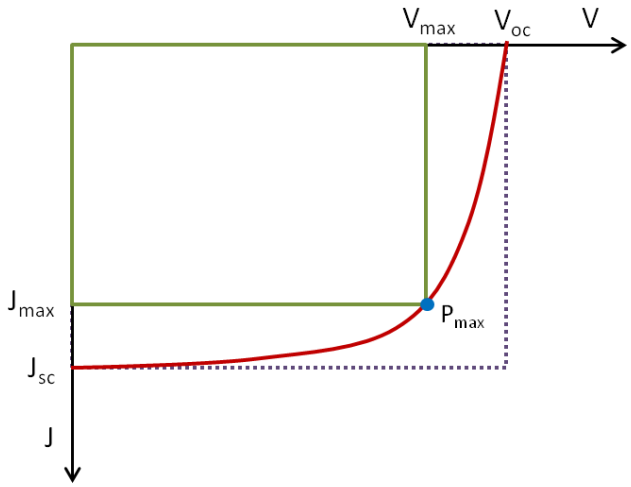


Figure 1.3 Typical current (J) – voltage (V) characteristics of a BHJ solar cell.

The open-circuit voltage ($V_{oc}$) is the maximum voltage the device generates at zero current, which depends on the material energetic.[12,13] Recently, it has been reported that $V_{oc}$ is influenced by the lifetimes of charge carriers within the blend, such as charge

photogeneration and recombination kinetics.[14,15] Short-circuit current ($J_{sc}$) is the maximum current the device generates when the voltage across the device is zero, which is influenced by the absorption efficiency, exciton dissociation efficiency, and charge collection efficiency in the device.[16] Thus, $J_{sc}$ is governed by the three-dimensional morphology formed by a network of donor and acceptor materials, as well as overlap between absorption in the device and solar spectrum, and thicknesses of the absorbing layers.[17,18] Fill factor (FF) is defined as:

$$FF = \frac{J_{max}V_{max}}{V_{oc}J_{sc}} \quad (1.2)$$

FF is the ratio of actual maximum power output the device generates to theoretical power output, which is mainly influenced by the serial electrical resistance of the device. In order to increase the power conversion efficiency, therefore, it is required to improve these three parameters.

### 1.1.4 Bulk-heterojunction solar cells

Bulk-heterojunction solar cells are based on blends of an electron-donor material (D), such as a conjugated polymer or small molecule, and an electron-acceptor material (A), typically a fullerene derivative. For the donor material, most polymers of interest consist of two distinct constituents: i) π-conjugated backbones that can lead to favorable π-orbital interactions, which primarily determine the intrinsic electronic/optical properties and deliver structural rigidity; and ii) non-conjugated side groups that impart solubility to the polymer but also impact the packing structure, morphology, and microstructure of the

polymer film. Importantly, the packing structure, morphology, and microstructure are both kinetically and thermodynamically driven during deposition from solution.[3,19,20]

The most widely used conjugated polymers in OPVs to date are based on polythiophene derivatives, such as regioregular poly(3-hexylthiophene) (rr-P3HT).[21] Polythiophene thin films generally consist of ordered lamellar structures that define the material charge-transport pathways – typically along the linear conjugated backbones (intramolecular) and through the stacked π-conjugated backbones (intermolecular). Therefore, the polymer-chain orientation with respect to the electrodes can have considerable influence on the (opto)electronic characteristics of the device. In general, P3HT self-assembles into two-dimensional sheets in one of two primary orientations with respect to the substrate: i) edge-on, where the lamella are parallel to the substrate; or ii) face-on, where the lamella are perpendicular to the substrate. The orientation of the crystalline regions in the polymer film affects the charge-carrier mobilities measured in organic field effect transistor (OTFT) architectures: high mobilities of 0.05 - 0.1 $cm^2V^{-1}s^{-1}$ are observed for the edge-on orientation (as the π-π stacking direction is parallel to the substrate), while films with face-on orientation tend to have a limited mobility of $2\times10^{-4}$ $cm^2V^{-1}s^{-1}$.[22]

Recently, poly (2,5-bis (3–alkyl thiophene–2–yl) thieno [3,2-b] thiophene) (PBTTT-$C_n$) has been reported as a promising polymer semiconductor for organic electronics (mostly OFET applications) due to a large hole mobility (up to 1 $cm^2V^{-1}s^{-1}$) and highly-ordered structure.[23,24] PBTTT-$C_n$ monomer consists of a thienothiophene unit appended on each side by a single thiophene unit that contains a long alkyl side chain (typically ranging

from $C_8H_{17}$ to $C_{18}H_{37}$). The alkyl side chains are relatively well-ordered allowing for interdigitation and the formation of closely packed lamellar structures with edge-on orientation. PBTTT shows a liquid-crystalline (LC) phase and has reduced side-chain density compared to P3HT, which provides for more regularly-ordered lamellae morphology after thermal annealing.

Poly([2-methoxy-5-[(3,7-dimethyloctyl)oxy]phenylene]vinylene) (MDMO-PPV) is one of the amorphous conjugated polymer intensively studied in bulk-heterojunction solar cells, as it exhibits an increase in hole mobility by several orders of magnitude when it is mixed with $PC_{61}BM$.[25,26] Regiospecific MDMO-PPV has a higher hole mobility than the regiorandom configuration, which could improve the charge-transport properties and power conversion efficiency in organic solar cells.[27]

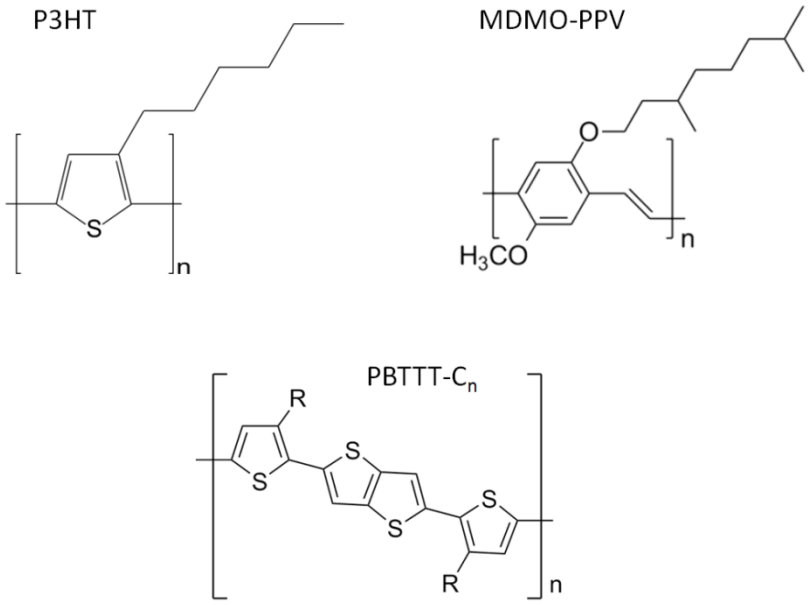


Figure 1.4 Chemical structures of conjugated polymers used in bulk heterojunction solar cells.

For the acceptor material, the electron affinity must be high enough to provide the energy to dissociate the exciton into free charge carriers. Well-known acceptor materials are based on fullerenes, such as $C_{60}$ and $C_{70}$, due to large electron affinity and stability induced by the high symmetry, and their corresponding derivatives, the functionalized fullerenes to improve solubility and processibility (see Figure 1.5). The most widely used fullerene derivatives as the acceptor are methanofullerene phenyl-$C_{61}$-butyric acid methyl ester ($PC_{61}BM$) and phenyl-$C_{71}$-butyric acid methyl ester ($PC_{71}BM$). PCBM provides good solubility in common organic solvents, acceptable electron mobilities, and large electron affinities, which leads to ultrafast exciton dissociation and improved solar cell performance. Recently, new fullerene derivatives, indene-$C_{60}$-monoadduct ($IC_{60}MA$) and indene-$C_{60}$-bisadduct ($IC_{60}BA$), have been introduced as a promising acceptor for high-performance organic solar cells comparable to or even better than with PCBM. Solar cells made with P3HT and indene fullerene derivatives show enhanced $V_{oc}$ and PCE of the solar cell compared to PCBM.[28]

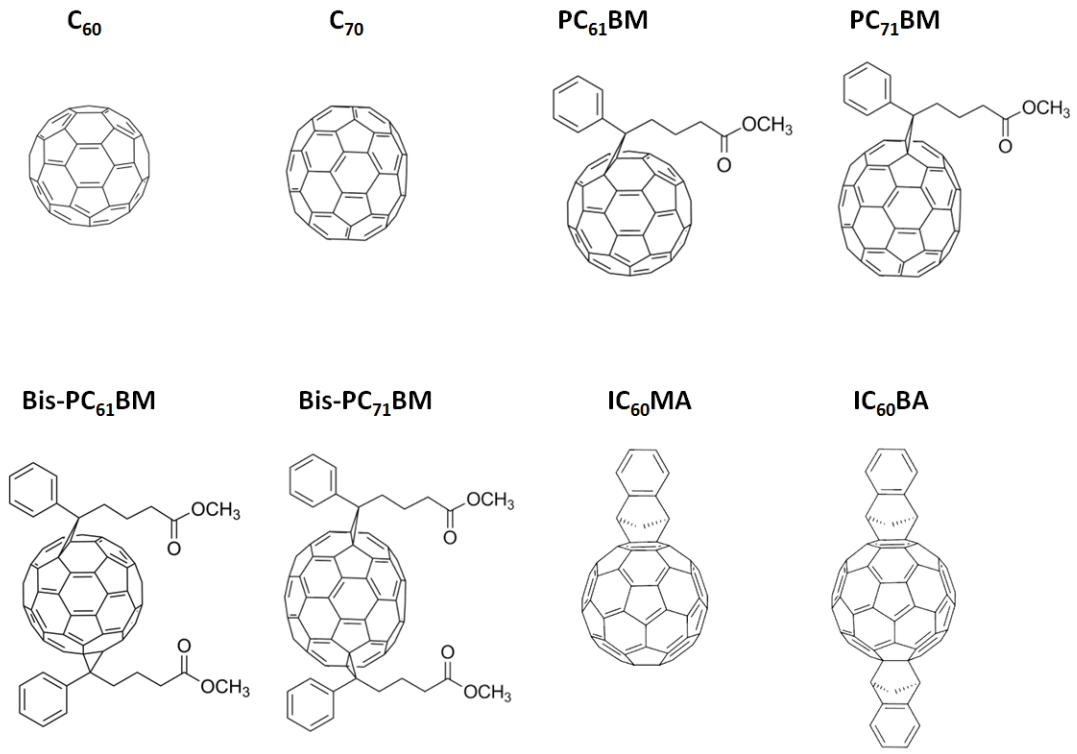


Figure 1.5 Chemical structures of a few prominent fullerene-based electron acceptors for bulk-heterojunction solar cells.

The bulk-heterojunction architecture features three dimensional interpenetrating networks between two materials with different electron affinities and ionization potentials, and has led to promising power conversion efficiencies greater than 9%.[29-31] The performance of BHJ solar cells is strongly influenced by the morphology controlled by the blend ratio and processing conditions, such as solvent, thermal annealing, solution concentration, and processing additives, as well as the properties of the electron donor material, such as regioregularity, molecular weight, and crystallinity of the polymers. For instance, a blend of P3HT and $PC_{61}BM$ exhibits a power conversion efficiency of 5.0 % at a P3HT/$PC_{61}BM$ weight ratio of 1.0:0.8~1.0.[32,33] A blend of poly(2-methoxy-5-(3′,7′-dimethyloctyloxy)-p-phenylene vinylene) (MDMO-PPV) and $PC_{61}BM$ in 1:4 weight ratio

yields a power conversion efficiency of 2.5% that has been improved to 3.5 % through the optimization of the processing conditions.[34,35] This suggests that the nanostructures of the D-A networks formed at various blend ratios can have a significant impact on the exciton dissociation, recombination, and charge transport.

More recently, it was revealed that in a blend of polymer and fullerene, for instance P3HT and $PC_{61}BM$ or MDMO-PPV and $PC_{61}BM$, there are i) mixed polymer-fullerene phases, ii) pure fullerene domains, and iii) ordered pure polymer domains.[13,36] The mixed phases indicate an interdiffusion of significant amounts of PCBM molecules within the amorphous polymer regions, which suggest favorable intermixing in polymer:fullerene blend. The resulting morphology might be promising for charge-carrier percolation. Therefore, it is important to understand morphology at the interface of D and A for improving the charge-transfer properties and further device performance.

### 1.1.5 Intercalated polymer:fullerene blends

Recently, intercalation of fullerene molecules amongst the polymer side chains has been observed in blends of PBTTT-$C_n$, importantly, no fullerene intercalation of the fullerenes is observed in blends of P3HT.[37] Moreover, it was shown that intercalation can occur in blends of amorphous polymer, such as MDMO-PPV.[38] In the case of blends with amorphous polymers, structure determination is very challenging because it cannot be simply measure structural properties using X-ray diffraction. For blends of semicrystalline PBTTT-$C_n$, on the other hand, Mayer *et al.* used grazing incidence X-ray diffraction (GIXD) techniques to determine the morphology of the blend as a function of

PCBM content and found that the intercalated blend constitutes a "bimolecular" crystal, an ordered and thermodynamically stable structure formed by two distinct chemical species. At a 1:1 weight ratio, fullerenes fully intercalate within the polymer side chains. Additional pure fullerene crystalline domains start showing at higher fullerene loading, which facilitates electron transport in the device. As a result, OPV efficiencies of 2.3% and 2.5% are obtained for the solar cell made at 1:4 blend of PBTTT-$C_{14}$ and PBTTT-$C_{16}$ with $PC_{71}BM$, respectively.[39,40] This indicates that the ability of fullerenes to intercalate into the polymer side-chains can significantly influence the optimal blend ratio of polymer and fullerene compared to that of non-intercalated polymer:fullerene blends (in general, around 1:1 weight ratio) since fullerenes must fill all available space between the polymer side chains prior to the formation of a pure fullerene phase in blends. Therefore, intercalation can further affect morphology and overall performance in the device. While $PC_{71}BM$ intercalation is a critical factor in controlling the nanostructures of the blend, it has not been clearly resolved how the polymer and fullerene interact to form the bimolecular crystal or how the bimolecular crystal influences charge transport and device performance.

## 1.2 Computational modeling

In the fields of science and engineering, computer simulations have been widely used to investigate and understand the microscopic and macroscopic properties of a variety of systems.[41] Various simulation techniques have been developed from quantum mechanics to molecular mechanics or dynamics and extensively applied in biology, chemistry, physics, and materials engineering.

Quantum mechanics (QM)[42] calculations are based on the Schrödinger equation for a system of atoms and include the interactions of nuclei and electrons. To describe molecular properties, a wave function can be calculated by several mathematical methods that use approximations in dealing with electron and nuclear motions. QM is useful in describing the structure and behavior of molecules as a function of electron distribution, and is the only computation method that can calculate the geometries and properties of transition states and excited states. While highly accurate, QM techniques require significant computational costs compared to molecular mechanics techniques.

Molecular mechanics (MM)[43] techniques minimize the energy of a system with respect to the nuclear coordinates by using a force field founded in classical mechanics. The lowest energy state can be found after several or thousands of iterations, and depends on the size or initial geometry of the model and nature of the algorithm. The advantages of these techniques include their simplicity, versatility, and short calculation times, which have led to their wide applications in conformational analysis, crystalline/amorphous structure modeling, and mechanical properties of polymers. MM methods do have limitations: they obtain time-independent property and ignore the electron motions in the systems as they only account for nuclear positions.

Molecular dynamics (MD)[44,45] techniques account for the atomic motions of large-scale systems for a certain time period, pressure, and temperature. During MD simulations, the atomic trajectories of the system are obtained by numerical integration of Newton's equations of motion for the entire system. MD can provide information concerning

individual particle motions as a function of time and lead to predictions of microscopic behavior, and structure and energy of the molecular systems. However, MD techniques also ignore electron motions in the system and are computationally expensive compared to other simulation techniques as they are typically applied to systems with large numbers of atoms.

These various computational methods have been extensively used to understand the morphology, vibronic, and electronic properties in the polymer:fullerene blend. Specifically, in the case of PBTTT, density functional theory (DFT) calculations were used to evaluate the tilt angle of the conjugated backbone with respect to the substrate normal[46] or to determine the electronic and charge-transport properties of the polymer.[47] Molecular mechanics and X-ray diffraction simulations were carried out to study the molecular packing of PBTTT-$C_{12}$, with a focus on the supra-organization of the polymer chains in lamellae.[48] These earlier simulations focused on the pristine PBTTT-$C_n$; to date, there are only few theoretical studies of the PBTTT-$C_n$ /PCBM blend. Lee *et al.* have developed a coarse grained (CG) MD simulation to reveal the correlation between solubility of PCBM in the polymer and optimal blend ratio of the polymer and fullerene.[49] Importantly, however, the exact structure of the polymer and PCBM in the bimolecular crystal is still not clearly understood.

## 1.3 Thesis objectives and outline

The device performance of an intercalated polymer:fullerene blend can be significantly influenced by how polymer and fullerene assemble and interact at the interface, as well as intrinsic properties of each component. In this dissertation, we aim to understand the formation of a bimolecular crystal structure, derived from conjugated polymers and fullerenes, and investigate the relationship between packing morphology, electronic properties, and charge-transport properties using a series of computational approaches that range from quantum mechanics to molecular mechanics and dynamics and simulations of 2D X-ray diffraction patterns. This dissertation offers to lead to a better understanding of the interaction and morphology of donor and acceptor materials, and to elucidate the relationship between microstructure and electronic properties of the blend.

Herein, we focus on a blend of poly (2,5-bis (3–alkyl thiophene–2–yl) thieno [3,2-b] thiophene) (PBTTT-$C_n$) and phenyl $C_{71}$-butyric acid methyl ester ($PC_{71}BM$). Before studying the bimolecular crystal structure, pristine PBTTT-$C_n$ systems are investigated in terms of molecular packing structure to then better comprehend how $PC_{71}BM$ interact PBTTT-$C_n$ and how $PC_{71}BM$ with various molar ratios affects the microstructure of the polymer. Finally we examine the charge-transport properties of each component, i.e., pristine polymers and fullerenes to better understand charge-carrier transport in the bimolecular crystal.

In Chapter 2, we review the computational methods used throughout the thesis. First, basic descriptions of the quantum mechanics (QM) calculations are provided, as these are

used to evaluate the electronic and vibrational properties of the systems under study. Second, molecular mechanics (MM) and molecular dynamics (MD) are introduced, as these calculations are performed to determine the crystal packing structure and degree of (dis)order in the system. Finally, we take a look at basic concepts of X-ray diffraction (XRD) and a simulation method for generating grazing incidence X-ray diffraction (GIXD) patterns that allows us to establish a robust model for the bimolecular crystal through comparison with experimental data.

In Chapter 3, pure PBTTT-$C_n$ systems with n=12, 14, and 16 are investigated in terms of molecular packing structure and electronic properties. With a comparison to the experimental data for both uniaxially and biaxially aligned films, we determine the molecular packing structure of PBTTT-$C_{14}$ using molecular mechanics (MM) and 2D grazing incidence X-ray diffraction (GIXD) simulations. We examine the influence of various alkyl side-chain lengths on the packing, orientations, and electronic properties of the polymers.

In Chapter 4, the detailed packing structure of the bimolecular crystal of PBTTT-$C_{14}$:$PC_{71}BM$ is revealed using a combination of simulations and experimental 2D GIXD and 2D solid-state nuclear magnetic resonance (NMR) data. We confirm molecular disorder in the blend using molecular dynamics (MD) based on the construction of a super cell, and determine the relationship between packing structure and electronic properties in the intercalated blend. Finally we aim to understand the thermodynamic

processes that lead to the formation of the blend system by evaluating the driving forces for molecular mixing in the bimolecular crystal.

In Chapter 5, the intrinsic vibrational, redox, and optical properties of PBTTT and a series of fullerenes, as a function of redox state, are evaluated quantum mechanically. The data are important in order to evaluate and better understand the relationship between the spectroscopic changes and the properties of the polymer:fullerene blends.

This work combines several computational methods to understand the complex properties of the bulk-heterojunction solar cells. The results could suggest ways to design the molecular structure of donor polymers to control the placement of fullerenes or other electron accepting materials. Moreover, our studies will assist in understanding the morphology of D and A materials and charge transport in organic electronics applications.

## 1.4 References


(1) Coakley, K. M.; McGehee, M. D. *Chem. Mat.* **2004**, *16*, 4533.

(2) Kroon, R.; Lenes, M.; Hummelen, J. C.; Blom, P. W. M.; De Boer, B. *Polym. Rev.* **2008**, *48*, 531.

(3) Chabinyc, M. L. *Polym. Rev.* **2008**, *48*, 463.

(4) Mayer, A. C.; Scully, S. R.; Hardin, B. E.; Rowell, M. W.; McGehee, M. D. *Mater. Today* **2007**, *10*, 28.

(5) Hoppe, H.; Sariciftci, N. S. *J. Mater. Res.* **2004**, *19*, 1924.

(6) Bredas, J. L.; Norton, J. E.; Cornil, J.; Coropceanu, V. *Acc. Chem. Res.* **2009**, *42*, 1691.

(7) Thompson, B. C.; Frechet, J. M. J. *Angew. Chem.-Int. Edit.* **2008**, *47*, 58.

(8) Blom, P. W. M.; Mihailetchi, V. D.; Koster, L. J. A.; Markov, D. E. *Adv. Mater.* **2007**, *19*, 1551.

(9) Kippelen, B.; Bredas, J. L. *Energy Environ. Sci.* **2009**, *2*, 251.

(10) Brabec, C. J.; Gowrisanker, S.; Halls, J. J. M.; Laird, D.; Jia, S. J.; Williams, S. P. *Adv. Mater.* **2010**, *22*, 3839.

(11) Clarke, T. M.; Durrant, J. R. *Chem. Rev.* **2010**, *110*, 6736.

(12) Brabec, C. J.; Cravino, A.; Meissner, D.; Sariciftci, N. S.; Fromherz, T.; Rispens, M. T.; Sanchez, L.; Hummelen, J. C. *Adv. Funct. Mater.* **2001**, *11*, 374.

(13) Gadisa, A.; Svensson, M.; Andersson, M. R.; Inganas, O. *Appl. Phys. Lett.* **2004**, *84*, 1609.

(14) Maurano, A.; Hamilton, R.; Shuttle, C. G.; Ballantyne, A. M.; Nelson, J.; O'Regan, B.; Zhang, W. M.; McCulloch, I.; Azimi, H.; Morana, M.; Brabec, C. J.; Durrant, J. R. *Adv. Mater.* **2010**, *22*, 4987.

(15) Cowan, S. R.; Roy, A.; Heeger, A. J. *Phys. Rev. B* **2010**, *82*, 245207.

(16) Forrest, S. R. *MRS Bull.* **2005**, *30*, 28.

(17) Geens, W.; Martens, T.; Poortmans, J.; Aernouts, T.; Manca, J.; Lutsen, L.; Heremans, P.; Borghs, S.; Mertens, R.; Vanderzande, D. *Thin Solid Films* **2004**, *451*, 498.

(18) Koster, L. J. A.; Mihailetchi, V. D.; Xie, H.; Blom, P. W. M. *Appl. Phys. Lett.* **2005**, *87*, 203502.

(19) Kline, R. J.; McGehee, M. D. *Polym. Rev.* **2006**, *46*, 27.

(20) Salleo, A.; Kline, R. J.; DeLongchamp, D. M.; Chabinyc, M. L. *Adv. Mater.* **2010**, *22*, 3812.

(21) Linares, M.; Scifo, L.; Demadrille, R.; Brocorens, P.; Beljonne, D.; Lazzaroni, R.; Grevin, B. *J. Phys. Chem. C* **2008**, *112*, 6850.

(22) Sirringhaus, H.; Brown, P. J.; Friend, R. H.; Nielsen, M. M.; Bechgaard, K.; Langeveld-Voss, B. M. W.; Spiering, A. J. H.; Janssen, R. A. J.; Meijer, E. W.; Herwig, P.; de Leeuw, D. M. *Nature* **1999**, *401*, 685.

(23) McCulloch, I.; Heeney, M.; Bailey, C.; Genevicius, K.; Macdonald, I.; Shkunov, M.; Sparrowe, D.; Tierney, S.; Wagner, R.; Zhang, W. M.; Chabinyc, M. L.; Kline, R. J.; McGehee, M. D.; Toney, M. F. *Nat. Mater.* **2006**, *5*, 328.

(24) Chabinyc, M. L.; Toney, M. F.; Kline, R. J.; McCulloch, I.; Heeney, M. *J. Am. Chem. Soc.* **2007**, *129*, 3226.

(25) Mihailetchi, V. D.; Xie, H. X.; de Boer, B.; Koster, L. J. A.; Blom, P. W. M. *Adv. Funct. Mater.* **2006**, *16*, 699.

(26) Tuladhar, S. M.; Sims, M.; Choulis, S. A.; Nielsen, C. B.; George, W. N.; Steinke, J. H. G.; Bradley, D. D. C.; Nelson, J. *Org. Electron.* **2009**, *10*, 562.

(27) Mozer, A. J.; Denk, P.; Scharber, M. C.; Neugebauer, H.; Sariciftci, N. S. *J. Phys. Chem. B* **2004**, *108*, 5235.

(28) He, Y. J.; Chen, H. Y.; Hou, J. H.; Li, Y. F. *J. Am. Chem. Soc.* **2010**, *132*, 5532.

(29) Peet, J.; Kim, J. Y.; Coates, N. E.; Ma, W. L.; Moses, D.; Heeger, A. J.; Bazan, G. C. *Nat. Mater.* **2007**, *6*, 497.

(30) Park, S. H.; Roy, A.; Beaupre, S.; Cho, S.; Coates, N.; Moon, J. S.; Moses, D.; Leclerc, M.; Lee, K.; Heeger, A. J. *Nat. Photonics* **2009**, *3*, 297.

(31) Liang, Y. Y.; Xu, Z.; Xia, J. B.; Tsai, S. T.; Wu, Y.; Li, G.; Ray, C.; Yu, L. P. *Adv. Mater.* **2010**, *22*, E135.

(32) Ma, W. L.; Yang, C. Y.; Gong, X.; Lee, K.; Heeger, A. J. *Adv. Funct. Mater.* **2005**, *15*, 1617.

(33) Kim, J. Y.; Kim, S. H.; Lee, H. H.; Lee, K.; Ma, W. L.; Gong, X.; Heeger, A. J. *Adv. Mater.* **2006**, *18*, 572.

(34) Shaheen, S. E.; Brabec, C. J.; Sariciftci, N. S.; Padinger, F.; Fromherz, T.; Hummelen, J. C. *Appl. Phys. Lett.* **2001**, *78*, 841.

(35) Brabec, C. J.; Shaheen, S. E.; Winder, C.; Sariciftci, N. S.; Denk, P. *Appl. Phys. Lett.* **2002**, *80*, 1288.

(36) He, Z. C.; Zhong, C. M.; Huang, X.; Wong, W. Y.; Wu, H. B.; Chen, L. W.; Su, S. J.; Cao, Y. *Adv. Mater.* **2011**, *23*, 4636.

(37) Mayer, A. C.; Toney, M. F.; Scully, S. R.; Rivnay, J.; Brabec, C. J.; Scharber, M.; Koppe, M.; Heeney, M.; McCulloch, I.; McGehee, M. D. *Adv. Funct. Mater.* **2009**, *19*, 1173.

(38) Cates, N. C.; Gysel, R.; Dahl, J. E. P.; Sellinger, A.; McGehee, M. D. *Chem. Mat.* **2010**, *22*, 3543.

(39) Parmer, J. E.; Mayer, A. C.; Hardin, B. E.; Scully, S. R.; McGehee, M. D.; Heeney, M.; McCulloch, I. *Appl. Phys. Lett.* **2008**, *92*, 113309.

(40) Cates, N. C.; Gysel, R.; Beiley, Z.; Miller, C. E.; Toney, M. F.; Heeney, M.; McCulloch, I.; McGehee, M. D. *Nano Lett.* **2009**, *9*, 4153.

(41) McHaney, R. W. *Computer simulation: A practical perspective*; Academic Press: San Diego, 1991.

(42) Shanker, R. *Principles of quantum mechanics*; 2nd ed.; Springer: New York, 1994.

(43) RAPPE, A. K.; CASEWIT, C. J. *Molecular mechanics across chemistry*; University Science Books: Sausalito, 1997.

(44) Allen, M. P.; Tildesley, D. J. *Computer simulation of liquids*; Oxford University Press: New York, 1989.

(45) Frenkel, D.; Smit, B. *Understanding molecular simulation*; 2nd ed.; Academic Press: San Diego, CA, 2002.

(46) DeLongchamp, D. M.; Kline, R. J.; Lin, E. K.; Fischer, D. A.; Richter, L. J.; Lucas, L. A.; Heeney, M.; McCulloch, I.; Northrup, J. E. *Adv. Mater.* **2007**, *19*, 833.

(47) Milian Medina, B.; Van Vooren, A.; Brocorens, P.; Gierschner, J.; Shkunov, M.; Heeney, M.; McCulloch, I.; Lazzaroni, R.; Cornil, J. *Chem. Mat.* **2007**, *19*, 4949.

(48) Brocorens, P.; Van Vooren, A.; Chabinyc, M. L.; Toney, M. F.; Shkunov, M.; Heeney, M.; McCulloch, I.; Cornil, J.; Lazzaroni, R. *Adv. Mater.* **2009**, *21*, 1193.

(49) Lee, C. K.; Pao, C. W. *J. Phys. Chem. C* **2012**, *116*, 12455.

# CHAPTER 2

# COMPUTATIONAL METHODOLOGY

In this chapter, we introduce the fundamental concepts and theories for a series of computational methods we use in this dissertation. First we present quantum mechanics (QM) methods used to evaluate the electronic, vibrational, optical properties of the system.[1-3] Then we describe classical mechanics methods, molecular mechanics (MM) and molecular dynamics (MD), used to determine the molecular structure and morphological disorder of the system, respectively.[4,5] Finally, we discuss the X-ray diffraction simulations which are a key in determining the detailed packing structure of the system.[6]

## 2.1 Quantum mechanics (QM)

### 2.1.1 Schrödinger equation

The time -independent Schrödinger equation for a system is given by:

$$\hat{H}\Psi(r_1, r_2, \cdots, r_N; R_1, R_2, \cdots, R_M) = E\Psi(r_1, r_2, \cdots, r_N; R_1, R_2, \cdots, R_M) \qquad (2.1)$$

where $\Psi$ is the wavefunction of the system of particles with *N* electrons and *M* nuclei; *E*, the energy of the system; $\hat{H}$, the Hamiltonian operator that is a sum of the kinetic energy operator and the potential energy operator. In atomic units, the Hamiltonian operator can be written as:

$$\hat{H} = -\frac{1}{2M_A}\sum_{A=1}^{M} \nabla_{\mathrm{A}}^2 - \frac{1}{2}\sum_{i=1}^{N} \nabla_{\mathrm{i}}^2 + \sum_{A=1}^{M}\sum_{B>1}^{M} \frac{Z_A Z_B}{R_{AB}} + \sum_{i=1}^{N}\sum_{j>1}^{N} \frac{1}{r_{ij}} - \sum_{i=1}^{N}\sum_{A=1}^{M} \frac{Z_A}{r_{iA}} \qquad (2.2)$$

where *i* and *j* refer to electrons and *A* and *B* refer to nuclei. $R_{AB} = |R_A - R_B|$ is the distance between the *A*th nucleus and *B*th nucleus; $r_{ij} = |r_i - r_j|$, the distance between the *i*th electron and *j*th electron; $r_{iA} = |r_i - R_A|$, the distance between the *i*th electron and *A*th nucleus; $M_A$, the ratio of the mass of nucleus *A* to mass of an electron; $Z_A$ or $Z_B$, the atomic number of nucleus *A* or *B*; $\nabla_A^2$ and $\nabla_i^2$, Laplacian operators, a second partial derivative in the coordinates of the *A*th nucleus and *i*th electron, respectively. The first and second terms represent the nuclear kinetic energy and electronic kinetic energy, respectively, while the third, fourth, and fifth terms denote the nuclear-nuclear repulsion energy, the electron-electron repulsion energy, and the electron-nuclear attraction energy, respectively. The exact solution of this equation can be presently limited to hydrogen and hydrogenoid atoms. Therefore, common and reasonable approximations are required to reduce the computational complexity to solve the equation. Since the nuclei have much larger masses than the electrons, it can be assumed that the electrons move within as assembly of fixed nuclei, the Born-Oppenheimer approximation. This approximation allows us to consider nuclear and electronic motions separately. Thus, the nuclear kinetic energy (the first term) can be neglected and the nuclear-nuclear repulsion interaction (the third term) can be considered a constant. As a result, the wavefunction is reduced to the electronic wavefunction ($\Psi_{el}$) that depends on the electronic coordinates at the given nuclear coordinates:

$$\widehat{H}_{el}\Psi_{el}(r_i; R_A) = E_{el}\Psi_{el}(r_i; R_A) \tag{2.3}$$

$$\widehat{H}_{el} = -\frac{1}{2}\sum_{i=1}^{N} \nabla_{\mathrm{i}}^2 + \sum_{i=1}^{N}\sum_{j>1}^{N}\frac{1}{r_{ij}} - \sum_{i=1}^{N}\sum_{A=1}^{M}\frac{Z_A}{r_{iA}} \tag{2.4}$$

### 2.1.2 Hartree-Fock (HF) approximation

Solving the electronic Schrödinger equation is still very complex since in many-electron systems the motion of every electron is coupled to the motion of all other electrons. Thus, additional approximations are required. The Hartree-Fock approximation is a common approximation widely used for solving many-body problems. Here, each electron can be treated independently but the effect of all the other electrons is included in an average way, *i.e.*, the mean-field approximation. Thus, the wavefunction is given by a single Slater determinant of *N* spin-orbitals that satisfies antisymmetry (Pauli exclusion principle):

$$\Psi(1,\cdots,N) = \frac{1}{\sqrt{N!}}\begin{vmatrix} \chi_1(1) & \chi_2(1) & \cdots & \chi_{\mathrm{n}}(1) \\ \chi_1(2) & \chi_2(2) & \cdots & \chi_{\mathrm{n}}(2) \\ \vdots & \vdots & \ddots & \vdots \\ \chi_1(\mathrm{N}) & \chi_2(\mathrm{N}) & \cdots & \chi_{\mathrm{n}}(\mathrm{N}) \end{vmatrix} \tag{2.5}$$

where $\chi_i$ is the one-electron wavefunction called a spin-orbital, a product of a spatial orbital ($\psi_i$) and a spin function ($\alpha$ or $\beta$). The full Hartree-Fock equation and the Hartree-Fock operator can be written in terms of occupied spatial orbitals as:

$$\hat{h}^{HF}(r_i)\chi_i(r_i) = \epsilon_i\chi_i(r_i) \tag{2.6}$$

$$\hat{h}^{HF} = -\frac{1}{2}\nabla_i^2 - \sum_A\frac{Z_A}{r_{iA}} + \sum_j^{occ} 2J_j(r_i) - \sum_j^{occ} K_j(r_i) \tag{2.7}$$

$$\text{where } J_j(r_i)\chi_i(r_i) = \left(\int d\, r_j \frac{\chi_j(r_j)\chi_j(r_j)}{r_{ij}}\right)\chi_i(r_i) \tag{2.8}$$

$$K_j(r_i)\chi_i(r_i) = \left(\int d\, r_j \frac{\chi_j(r_j)\chi_i(r_j)}{r_{ij}}\right)\chi_j(r_i) \tag{2.9}$$

Here, the first and second terms are the kinetic energy and nuclear attraction energy, respectively, and are related to the non-interacting electrons in the system. The third and fourth terms are the repulsive Coulomb potential energy including the electron-electron interactions, and exchange interaction energy arising from the antisymmetry requirement of the wavefunction.

To solve the spatial HF equation, solutions are usually found by expanding the spin-orbitals as:

$$\chi_i(r_i) = \sum_k^M C_{ik}\phi_k(r_i) \tag{2.10}$$

As a result, the unknown Hartree-Fock orbitals, $\chi_i$, are written as a linear combination expansion in $M$ known basis functions $\phi_k$ with a set of expansion coefficients $C_{ik}$. By inserting eq. (2.8) into the spatial HF equation, this leads to:

$$\hat{h}^{HF}(r_i)\sum_k^M C_{ik}\phi_k(r_i) = \epsilon_i \sum_k^M C_{ik}\phi_k(r_i) \tag{2.11}$$

By multiplying by $\phi_\mu^*(r_i)$ on the left on each side, this yields the following matrix form as:

$$\sum_k F_{k\mu} C_{ik} = \epsilon_i \sum_k S_{k\mu} C_{ik} \quad (2.12)$$

$$\text{where } F_{k\mu} = \int d\tau\, \phi_\mu^*(r_i) \hat{h}^{HF}(r_i) \phi_k(r_i) \quad (2.13)$$

$$S_{k\mu} = \int d\tau\, \phi_\mu^*(r_i) \phi_k(r_i) \quad (2.14)$$

$F_{k\mu}$ is the Fock matrix element and $S_{k\mu}$ is the overlap matrix element. This result can be written as a single matrix equation, known as the Hartree-Fock-Roothaan equation:

$$FC = SC\varepsilon \quad (2.15)$$

Here, $\varepsilon$ is a diagonal matrix of the orbital energies $\varepsilon_i$ and $C$ is an M×M coefficient matrix.

The HF equation must be solved iteratively by using an initial guess of the C matrix, referred to as the self-consistent field (SCF) procedure.

### 2.1.3 Density functional theory (DFT)

Density functional theory (DFT) is an alternative to Hartree-Fock methods. The main idea of DFT is to utilize the electron density to determine the energy of the ground state in the many-body system. The electron density $\rho(r)$ is defined as the integral over the spin coordinates of all electrons, and over all but one of the spatial variables

$$\rho(r) = N \int \cdots \int |\Psi(x_1, x_1, \cdots, x_N)|^2 ds_1 dx_2 \cdots dx_N \quad (2.16)$$

The integral of the electron density gives rise to the total number of electrons.

$$\int \rho(r)dr = N \tag{2.17}$$

2.1.3.1 The Hohenberg-Kohn theorems

For the system of interacting electrons in an external potential, the total energy of the system can be defined in terms of the electron density and expressed as:

$$E[\rho] = T[\rho] + V_{ext}[\rho] + V_{ee}[\rho] \tag{2.18}$$

where $T[\rho]$ denotes the kinetic energy of the system, $V_{ext}[\rho]$ denotes the electron-nuclear attraction called the external potential in DFT, and $V_{ee}[\rho]$ denotes the electron-electron interaction energy. The exact ground state is the global minimum value of this functional. The external potential $V_{ext}[\rho]$ is (to within a constant) a unique functional of $\rho(r)$, which is trivial:

$$V_{ext}[\rho] = \int V_{ext}\,\rho(r)dr \tag{2.19}$$

The sum of the kinetic and electron-electron interaction energies is defined as the Hohenberg-Kohn functional:

$$E_{HK}[\rho] = T[\rho] + V_{ee}[\rho] \tag{2.20}$$

This equation is the key in DFT. If the exact functional $E_{HK}[\rho]$ can be found, then the system can be solved exactly.

2.1.3.2 The Kohn-Sham equations

Kohn and Sham proposed the following approach to approximate the kinetic and electron-electron interaction terms: the exact kinetic energy of the original interacting system can be replaced by that of the non-interacting system. For the system of N non-interacting electrons, the kinetic energy is the sum of the individual electronic kinetic energies

$$T_s = -\frac{1}{2}\sum_i^N \langle \phi_i | \nabla^2 | \phi_i \rangle \tag{2.21}$$

where $T_s$ denotes the Kohn-Sham kinetic energy and $\phi_i$ represents the Kohn-Sham orbital.

The density for the system is written by:

$$\rho(r) = \sum_i^N |\phi_i(r)|^2 \tag{2.22}$$

The total energy of a system is expressed as a functional of the density as:

$$E[\rho] = T_s[\rho] + V_{ext}[\rho] + V_H[\rho] + E_{XC}[\rho] \tag{2.23}$$

where $T_s$ represents the Kohn-Sham kinetic energy (that is not the true kinetic energy but is that of a system of non-interacting electrons); $V_{ext}$, the external potential on the interacting system; $V_H$, the Hartree energy (or Coulomb energy); and $E_{xc}$, the exchange-correlation energy. The exchange-correlation energy is defined as:

$$E_{XC}[\rho] \equiv (T[\rho] - T_s[\rho]) + (V_{ee}[\rho] - J[\rho]) \tag{2.24}$$

By introducing non-interacting orbitals, the minimized energy can be obtained by solving the following equation:

$$\left[-\frac{1}{2}\nabla^2 + V_{ext}(r) + \int \frac{\rho(r')}{|r-r'|}dr' + V_{xc}(r)\right]\phi_i(r) = \varepsilon_i\phi_i(r) \qquad (2.25)$$

where $V_{xc} \equiv \frac{\delta E_{xc}[\rho]}{\delta\rho}$ represents the exchange-correlation potential. This equation provides a theoretically exact method for finding the ground-state energy of an interacting system if the form of $E_{xc}$ is known. However, $E_{xc}$ is in general unknown and its exact value has been calculated for only a few very simple systems. In electronic structure calculations, therefore, $E_{xc}$ is most commonly approximated within the local density approximation (LDA), generalized-gradient approximation (GGA), or hybrid functionals that incorporate a portion of exact HF exchange in the DFT functionals. One of the most popular hybrid functional is B3LYP (Becke, 3-parameter, Lee-Yang-Parr).[7-9]

## 2.2 Atomistic simulations

In a classical mechanics description, such as molecular mechanics (MM) and molecular dynamics (MD), molecules are considered as a series of balls (atoms) connected by springs (bonds). Newton's equation of the motion is the key formula in these methods. Both MM and MD describe the potential energy surface of a molecular system as a function of the nuclear positions to provide the structures and properties of the system. A set of equations is employed to obtain the potential energy surface, referred to as a force field (FF). The force fields contain the functional forms with parameters for each type of atoms; they are determined by fits to experimental data or by incorporating results of high

level quantum mechanics (QM) calculations. Therefore, the force fields are the essential infrastructure in MM and MD simulations.

### 2.2.1 Force fields (FF)

Various force fields have been developed and widely used for numerous applications. Classical force fields, also called first-generation force fields, were mainly designed for biological molecules, such as proteins and nucleic acids, and include AMBER,[10] CHARMM,[11] and GROMOS.[12] Second-generation force fields include CFF,[13] COMPASS,[14] MM2,[15] and MM3,[16] and were adapted to large and complex systems, such as organic/inorganic molecules and polymers. These allow for the prediction of properties for many diverse systems. Generic force fields, such as the Universal Force Field (UFF)[17] and Dreiding,[18] have a broad range of applications for the full periodic table, and are useful for predicting the structures and dynamics of organic, biological, and inorganic systems. There are in addition special-purpose force fields applied to particular types of models. ENZYMIX,[19] for example, is the first polarizable force field that has been used in many applications to biological systems.

Generally, the potential energy for a molecule in the force field is expressed as sum of valence or bonded interactions ($E_{valence}$) and non-bonded interactions ($E_{non\text{-}bonded}$):

$$E_{tot} = E_{valence} + E_{non-bonded} \tag{2.26}$$

$$E_{valence} = E_R + E_\theta + E_\phi + E_\omega \quad (2.27)$$

$$E_{non-bonded} = E_{el} + E_{vdw} \quad (2.28)$$

The valence interactions relate to atoms linked directly by covalent bonds, and consist of bond stretching ($E_R$), bond angle bending ($E_\theta$), dihedral angle torsion ($E_\phi$), and inversion terms ($E_\omega$). The non-bonded interactions consist of the long-range electrostatic terms ($E_{el}$) and van der Waals ($E_{vdw}$) terms.

2.2.1.1 Valence interactions

*Bond stretch*

As shown in Figure 2.1, the two-body bond stretch terms represent the necessary energy to stretch or compress the bond, and is described by a harmonic oscillator (equation 2.29) or Morse potential function (equation 2.30):

$$E_R = \frac{1}{2} K_{ij}(r - r_{ij})^2 \quad (2.29)$$

$$E_R = D_{ij}\left[e^{-\alpha(r-r_{ij})} - 1\right]^2 \quad (2.30)$$

where $K_{ij}$ represents the force constant in units of (kcal/mol)/Å$^2$; $r_{ij}$, the natural (equilibrium) bond length in Å; $D_{ij}$, the bond dissociation energy (kcal/mol); and $\alpha = (\frac{K_{ij}}{2D_{ij}})^{1/2}$. The harmonic potential is a simple form for bond stretching and does not allow bond breaking. In contrast, the Morse function is a more accurate description as it is an anhormonic potential function that can lead to a finite energy for breaking bonds.

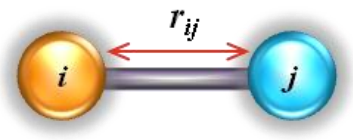


Figure 2.1 Schematic illustration of bond stretch.

*Angle bend*

The basic mathematical form for describing the three-body angle bend term is a harmonic potential:

$$E_\theta = \sum \frac{1}{2} K_{ijk}(\theta - \theta_0)^2 \qquad (2.31)$$

where $K_{ijk}$ denotes the force constant of the particular angle; $\theta_0$, the natural bond angle (equilibrium angle); and $\theta$, the valence angle between bonds *ij* and *jk* as shown in Figure 2.2. For angle deformations far from the equilibrium value, a higher polynomial is used for a better description:

$$E_\theta = \sum K_{ijk}(\theta - \theta_0)^2 + K_{ijk}'(\theta - \theta_0)^3 + K_{ijk}''(\theta - \theta_0)^4 + \cdots \qquad (2.32)$$

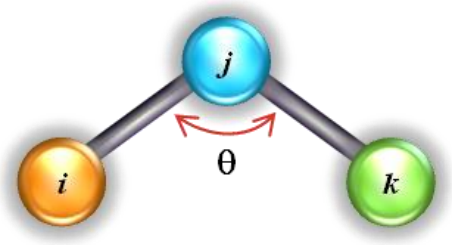


Figure 2.2 Schematic illustration of angle bend.

*Torsion*

The four-body torsion terms for two bonds *ij* and *kl* connected via a common bond *jk*, shown in Figure 2.3, are expressed as a cosine Fourier expansion:

$$E_{\phi} = K_{ijkl} \sum_{n=0}^{m} C_n \cos(n\phi) \tag{2.33}$$

where $\phi$ represents the dihedral angle, i.e. angle between the *ijk* and *jkl* planes, and $\phi$=0 corresponds to the *cis*-configuration. $K_{ijkl}$ and the coefficients $C_n$ are determined by the rotational barrier ($V_\phi$), the periodicity of the potential ($n$), and equilibrium angle ($\theta_0$) by the following relationship:

$$C_0 = 1,\ C_n = -\cos(n\phi_0),\ K_{ijkl} = \frac{1}{2}V_{\phi} \tag{2.34}$$

Using equation (2.34), equation (2.33) can then be represented as:

$$E_{\phi} = \frac{1}{2}V_{\phi}\left[1 - \cos(n\phi_0)\cos(n\phi)\right] \tag{2.35}$$

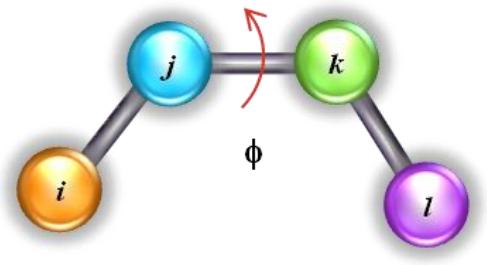


Figure 2.3 Schematic illustration of torsion.

*Inversion (out-of-plane)*

For an atom *i* bonded exactly to three other atoms *j*, *k*, and, *l*, as shown in Figure 2.4, it is required that a four-body inversion term be added to describe the energy associated with maintaining the bonds in the same plane. The expression of inversion terms for UFF writes as:

$$E_{\omega} = K_{ijkl}[C_0 + C_1\cos(\omega) + C_2\cos(2\omega)] \quad (2.36)$$

where $K_{ijkl}$ denotes the force constant in (kcal/mol); $C_n$, one of the coefficients explained above; and ω, the angle between one *il* bond and the *ijk* plane.

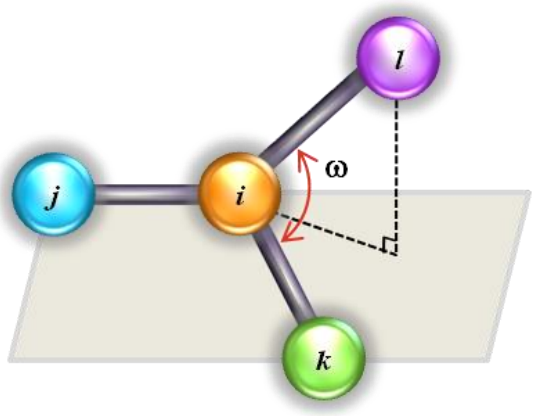


Figure 2.4 Schematic illustration of inversion.

2.2.1.2 Non-bonded interactions

The non-bonded energy terms represent the pair-wise sum of the energies of all possible interactions of non-bonded atoms *i* and *j*, shown in Figure 2.5.

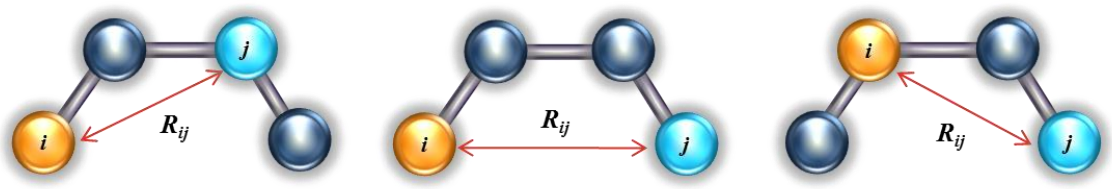


Figure 2.5 Schematic illustration of non-bonded interactions.

*Electrostatic interactions*

The simulation of polar and ionic molecules is dominated by the electrostatic energies. Electrostatic interactions play an important role in determining the crystalline organization of π-conjugated systems, although the interactions in such systems are weak compared to polar compounds. Accordingly, high-level QM calculations have been applied for further improvement and appropriate treatment of the long-range electrostatic potential.

In general, electrostatic interactions are calculated using a Coulombic potential:

$$E_{el} = C_0 \left( \frac{q_i q_j}{\varepsilon R_{ij}} \right) \qquad (2.37)$$

where $q_i$ and $q_j$ represent the atomic point charges in electron units; ε, the dielectric constant that accounts for the attenuation of electrostatic interaction by the environment; $R_{ij}$, the inter-atomic distance between atom $i$ and $j$ in Å; and the conversion factor $C_0$ = 332.0637 ensures that energies are in kcal/mol. In the case of UFF, the default dielectric constant is 1 and partial charges are obtained by the charge equilibration (QEq) scheme.[20]

*Van der Waals interactions*

Van der Waals interactions describe the repulsion or attraction between non-bonded atoms. At very short range, this interaction is strongly repulsive, while at intermediate range the interaction is attractive. The most common description for van der Waals interactions is a 6-12 Lennard-Jones (LJ) potential:

$$E_{vdw}^{LJ} = D_{ij}\left\{-2\left(\frac{R_0}{R_{ij}}\right)^6 + \left(\frac{R_0}{R_{ij}}\right)^{12}\right\} \tag{2.38}$$

where $D_{ij}$ represents the depth of the potential well; $R_0$, the equilibrium van der Waals distance in Å; and $R_{ij}$, the inter-atomic distance between atoms $i$ and $j$. The $R_{ij}^{-6}$ is the attractive part, whereas the $R_{ij}^{-12}$ is the repulsive term.

Another common expression for the van der Waals term is the Buckingham exponential-6 form (X6) based on the short-range exponential repulsion explained by Pauli's exclusion principle and the long-range $R_{ij}^{-6}$ induced dipole-induced dipole dispersive attraction.

$$E_{vdw}^{X6} = Ae^{-BR_{ij}} - C/{R_{ij}}^6 \tag{2.39}$$

where $A$, $B$, and $C$ denote adjustable model parameters of the potential.

### 2.2.2 Molecular dynamics (MD)

2.2.2.1 Equation of motion

Newton's classical equation of motion is described by:

$$F_i = m_i a_i \tag{2.40}$$

where $F_i$ represents the force exerted on particle $i$; $m_i$, the mass of particle $i$; and $a_i$, the acceleration of particle $i$. The force can be expressed as the gradient of the potential energy ($V$):

$$F_i = -\nabla_i V \tag{2.41}$$

Combining these two equation yields:

$$-\frac{dV}{dr_i} = m_i \frac{d^2 r_i}{dt^2} \tag{2.42}$$

Therefore, the equation of motion is associated with the derivative of the potential energy with respect to the changes in position ($r_i$) as a function of time ($t$).

2.2.2.2 Integration algorithms

The integration algorithm is a key component in MD simulations where it is required to integrate the equation of motion of the interacting particles and follow their trajectory. There are several widely used algorithms. In all integration algorithms, the positions, velocities, and accelerations can be approximated by a Taylor series expansion.

The most commonly used integration algorithm is the Verlet algorithm:

$$r(t + \delta t) = 2r(t) - r(t - \delta t) + a(t)\delta t^2 \tag{2.43}$$

The Verlet method uses the positions and accelerations at time $t$ and the positions at time $t$-$\delta t$ to generate new positions at time $t$+$\delta t$. Thus, this algorithm is straightforward to

implement and time reversible. However, the velocities do not appear explicitly in the algorithm and are calculated only after $r(t+\delta t)$ are known as written below:

$$v(t) = \frac{r(t+\delta t) - r(t-\delta t)}{2\delta t} \tag{2.44}$$

The Leap-frog algorithm is a modified version of the Verlet algorithm. The velocities are first calculated at time $t+\delta t/2$ by the current acceleration and the velocity at the previous half-time interval, and used to determine the positions at time $t+\delta t$ with the position at time *t*. The velocity at time t is the average velocity of the velocities at time $t+\delta t/2$ and time $t-\delta t/2$.

$$r(t+\delta t) = r(t) + v\left(t + \frac{\delta t}{2}\right)\delta t \tag{2.45}$$

$$v\left(t + \frac{\delta t}{2}\right) = v\left(t - \frac{\delta t}{2}\right) + a(t)\delta t \tag{2.46}$$

$$v(t) = \frac{v\left(t+\frac{\delta t}{2}\right)v + \left(t-\frac{\delta t}{2}\right)}{2} \tag{2.47}$$

The advantage of this algorithm is that the velocities are explicitly calculated. However, the velocities are not obtained at the same time as the positions and depend on velocity averaging at different time intervals.

The velocity Verlet algorithm can start with positions, velocities and accelerations at time *t* to yield the same quantities at time $t+\delta t$:

$$r(t+\delta t) = r(t) + v(t)dt + \frac{1}{2}a(t)\delta t^2 \quad (2.48)$$

$$v(t+\delta t) = v(t) + \frac{1}{2}[a(t) + a(t+\delta t)]\delta t \quad (2.49)$$

This algorithm can solve the disadvantages in the Verlet algorithm and leap-frog algorithms. It is numerically stable and requires less computer memory because only one set of positions, forces and velocities need to be generated at one time.

2.2.2.3 Ensembles

An ensemble is an infinite collection of independent microscopic states within an identical macroscopic or thermodynamic state. There are several ensembles with different characteristics. The microcanonical ensemble (NVE) represents a collection of states with a constant number of atoms (N), volume (V), and total energy (E), which corresponds to an isolated system. The canonical ensemble (NVT) is a collection of states with a fixed number of atoms (N), volume (V), and temperature, (T). In the isobaric-isothermal ensemble (NPT), the thermodynamic state is characterized by a constant number of atoms (N), pressure (P), and temperature (T), which corresponds to laboratory conditions with ambient temperature and pressure.

Averages corresponding to experimental observables (macroscopic sampling) with particular thermodynamic constraints can be defined in terms of ensemble averages given by:

$$\langle A \rangle_{ensemble} = \iint dp^N dr^N A(p^N, r^N)\rho(p^N, r^N) \quad (2.50)$$

where $A(p^N, r^N)$ is the observable of interest expressed as a function of momenta ($p$) and positions ($r$) in the system. The integration runs over all possible variables of $p$ and $r$. $\rho(p^N, r^N)$ is the probability density of the ensemble described as:

$$\rho(p^N, r^N) = \frac{1}{Q} \exp[-H(p^N, r^N)/K_B T] \tag{2.51}$$

where $H$ represents the Hamiltonian; $T$, the temperature; $K_B$, Boltzmann's constant; and $Q$, the partition function:

$$Q = \frac{1}{N! h^{3N}} \iint dp^N dr^N \exp[-H(p^N, r^N)/K_B T].$$

In a molecular dynamics simulation, the points in the ensemble are calculated sequentially in time, so the measurable physical quantities are defined as time averages:

$$\langle A \rangle_{time} = \lim_{\tau \to \infty} \frac{1}{\tau} \int_0^\tau A(p^N(t), r^N(t)) dt \approx \frac{1}{M} \sum_{t=1}^{M} A(p^N, r^N) \tag{2.52}$$

where $t$ is the simulation time; $M$, the number of time steps in the simulation, and $A(p^N, r^N)$, the instantaneous value of $A$. By the Ergodic hypothesis, the time average is equal to the ensemble average.

$$\langle A \rangle_{time} = \langle A \rangle_{ensemble} \tag{2.53}$$

Here the basic idea is that the system will eventually pass through all possible states if the system evolves in time indefinitely. Therefore, MD simulations can in principle generate all possible microscopic states with particular thermodynamic constraints, which allows

us to determine the macroscopic observables corresponding to experimentally relevant quantities.

## 2.3 Grazing incidence X-ray diffraction (GIXD) simulations

### 2.3.1 General concepts for X-ray diffraction (XRD)

X-ray diffraction (XRD) is a useful technique for the identification of crystalline phases and orientations, and the determination of the structural properties of materials, such as lattice parameters, crystal grain sizes, and preferred orientations.[21] Diffraction in a crystal is a series of events involving both interference and coherent scattering. It is noteworthy that the kinematical approximation of single scattering is valid in most cases, since X-rays weakly interact with matter.

A crystalline material is constructed by periodically repeating a basic structural unit, which is referred to as the unit cell. A three-dimensional lattice is specified by a set of vectors of the form:

$$R_n = p\bar{a} + q\bar{b} + r\bar{c} \tag{2.54}$$

where $R_n$ represents the lattice vector; $(\bar{a}, \bar{b}, \bar{c})$, the basis vectors of the lattice; and ($p$, $q$, $r$), integers. Note that lattices occupied by the crystal in real space are known as direct lattices. XRD from a crystalline material can be considered as the scattering from atoms that lie within families of planes in the crystal. The most convenient way to describe the family of planes is the Miller indices (*hkl*), which are defined as the plane having

intercepts (*a/h, b/k, c/l*) on the axes $(\bar{a}, \bar{b}, \bar{c})$. The planes are equally spaced, so it is possible to define a lattice spacing $d_{hkl}$.

The reciprocal lattice basis vectors, shown in Figure 2.6, can be defined by:

$$\bar{a} \cdot \bar{a}^* = 2\pi, \qquad \bar{b} \cdot b^* = 2\pi, \qquad \bar{c} \cdot \bar{c}^* = 2\pi \tag{2.55}$$

$$\bar{a}^* = \frac{2\pi}{v}(\bar{b} \times \bar{c}), \quad b^* = \frac{2\pi}{v}(\bar{c} \times \bar{a}), \quad \bar{c}^* = \frac{2\pi}{v}(\bar{a} \times \bar{b}) \tag{2.56}$$

where $v = \bar{a} \cdot (\bar{b} \times \bar{c})$ denotes the volume of the unit cell.

Thus, the reciprocal lattice vector is represented by:

$$G = h\bar{a}^* + k\bar{b}^* + l\bar{c}^* \tag{2.57}$$

where *h, k, l* are (integer) Miller indices. If the scattering vector *Q* coincides with a reciprocal lattice vector, diffraction can occur, a condition known as the Laue condition. Here, the important features are that (i) the reciprocal lattice vector *G* is perpendicular to the (*hkl*) planes and (ii) the magnitude of *G* is related to the inverse of the lattice spacing $d_{hkl}$ of the (*hkl*) planes, $|G_{hkl}| = 2\pi/d_{hkl}$.

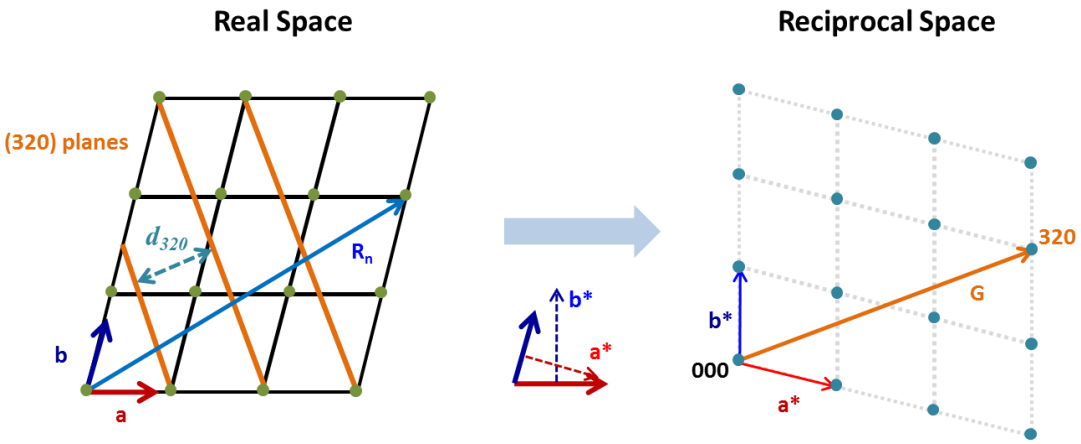


Figure 2.6 Example of the lattice in real space and reciprocal space.

### 2.3.2 Simulation of 2D grazing incidence X-ray diffraction (GIXD)

Grazing-incidence wide-angle X-ray diffraction (GIXD) illustrated in Figure 2.7 has been extensively used for structure characterization of thin films and surfaces. At incidence angles smaller than a critical angle, the X-ray beam is totally reflected from the surface and an evanescent wave parallel to the surface is created, which enhances the signal from the surface. Within this work, 2D GIXD simulations are carried out with the simDiffraction code.[22,23] The algorithm of the code is divided into three procedures. First, the reciprocal lattice vector $G_{hkl}$ of the crystal structure is calculated for defined crystallite orientation and lattice planes (*hkl*). Second, the scattering vector $Q$ is determined if the Laue condition $Q = G_{hkl}$ is satisfied by rotating $G_{hkl}$, and results in obtaining diffraction peaks. Finally, the peak intensity is calculated by integrating the geometrical correction factors, the form factor, and the structure factor.

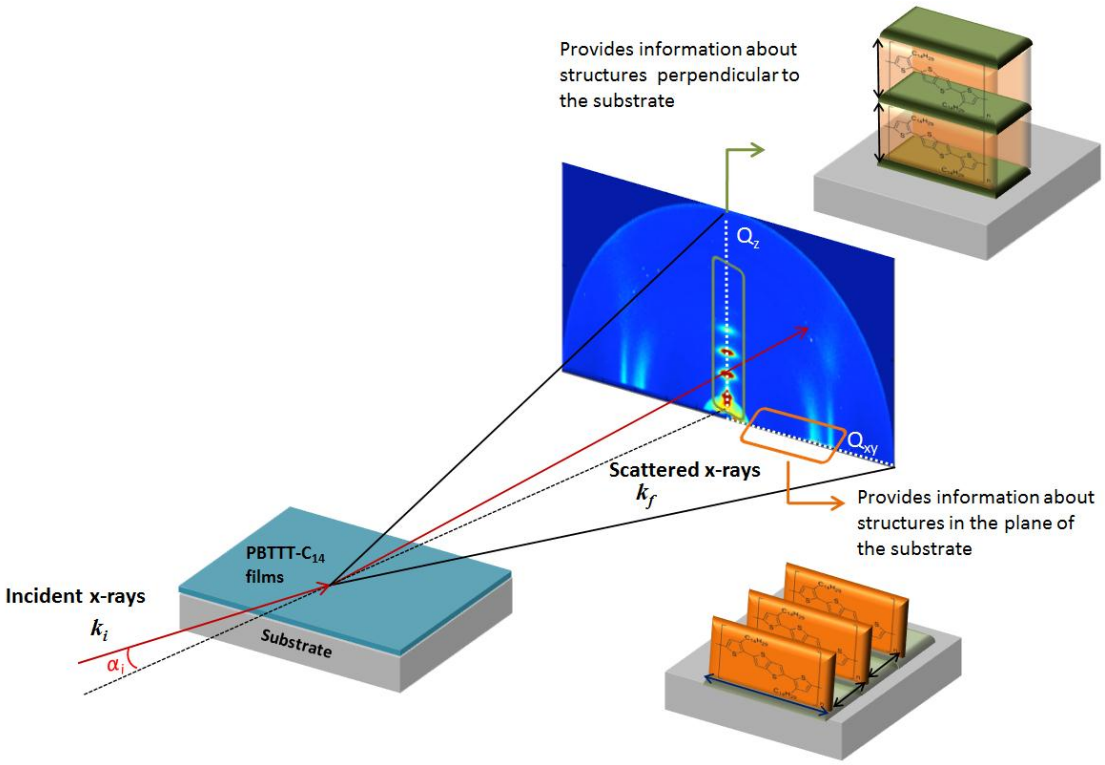


Figure 2.7 Schematic representation of grazing-incidence X-ray diffraction of PBTTT-$C_{14}$ thin films; $Q_{xy}$ and $Q_z$ are the components of the scattering vector parallel and perpendicular to the substrate, respectively; diffraction peaks along $Q_{xy}$ are due to periodic structures in the plane of the substrate (e.g., distance between the orange planes), and those along $Q_z$ are due to the structures perpendicular to the substrate.[24]

### 2.3.3 Calculation of the reciprocal lattice vector

A conventional 2+2 geometry with a monochromatic beam is applied, which has two angles for sample orientation, $\varphi$ (a sample azimuth) and $\alpha$ (an incidence angle), and two detector angles, $\gamma$ (in-plane) and $\delta$ (out-of-plane), as shown in Figure 2.8.[25,26]

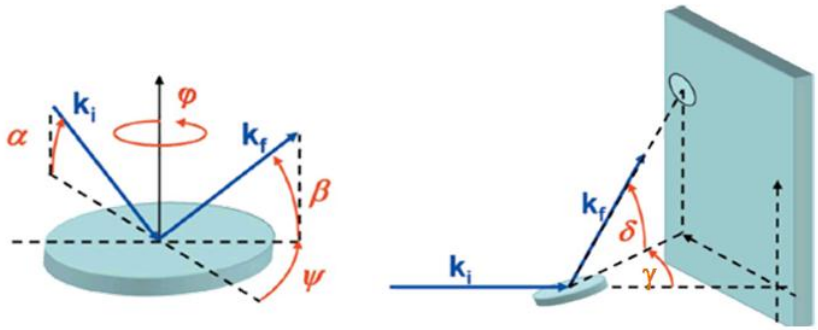


Figure 2.8 Scheme of the surface (left) and laboratory (right) reference frame: incident angle α, in-plane scattering angle ψ, exit angle β, azimuth angle φ, and scattering angles in the detection plane γ, δ.[25]

Given a crystal lattice with unit-cell parameters, *a*, *b*, *c*, *α*, *β*, and *γ*, the basis unit-cell vectors are calculated by employing the Protein Data Bank (PDB) convention,[27] resulting in:

$$\underline{a} = \begin{bmatrix} a \\ 0 \\ 0 \end{bmatrix}, \quad \underline{b} = \begin{bmatrix} b\cos(\gamma) \\ b\sin(\gamma) \\ 0 \end{bmatrix}, \quad \underline{c} = \begin{bmatrix} c\cos(\beta) \\ \{c\cos(\alpha) - c_x\cos(\gamma)\}/\sin(\gamma) \\ (c^2 - c_x^2 - c_y^2)^{1/2} \end{bmatrix} \tag{2.58}$$

The reciprocal lattice basis vectors $\bar{a}^*, \bar{b}^*,$ and $\bar{c}^*$ are easily obtained by using the general formula in equation (2.17). Finally the reciprocal lattice vector for an *(hkl)* plane can be indexed by:

$$G_0 = h\bar{a}^* + k\bar{b}^* + l\bar{c}^* \tag{2.59}$$

where $G_0$ lies parallel to the surface normal.

To describe crystallite domains for the dominant orientation, the rotation matrix R is employed, which defines the average of all crystallite orientations by taking the rotation angle about the *x*, *y*, and *z* axes. As a result, the reciprocal lattice vector for dominant (average) orientation, $G_D$, can be represented by:

$$G_D = R\, G_0(h,k,l) \tag{2.60}$$

In order to take into account all of the crystallite domains deviating from the dominant orientation, $W^i$ is used, which provides for orientational deviations of the *i*-th crystallite from the dominant orientation. For a single crystal, $\{W^i\}$=1, since there is only one domain. For polycrystalline systems, an appropriate set of values for $\{W^i\}$ should be considered based on the orientational distribution function of the films. In summary, a set of vectors $\{G_{hkl}\}$ is described by:

$$\{\, G_{hkl} \,\} = \{W^i\}\, R\, G_0(h,k,l) = \{W^i\} G_D \tag{2.61}$$

2.3.3.1 Determination of the scattering vector

The scattering vector is defined as $Q \equiv k_f - k_i$, where $k_i$ represents the incidence wave vector and $k_f$ represents the scattered wave vector. $Q$ is often decomposed into two components, $Q_{xy}$ and $Q_z$, respectively parallel and perpendicular to the substrate (see Figure 2.7). For elastic scattering, $Q \equiv |k_f| = |k_i| = 2\pi/\lambda$, where $\lambda$ represents the wavelength of the X-ray and $Q = |Q| = 2k\sin\theta$, where 2θ denotes the scattering angle. To satisfy the diffraction condition from a crystalline lattice, i.e. the Laue condition, $Q$

should coincide with the reciprocal lattice vector, $G_{hkl}$, which means a reciprocal lattice point should intersect the Ewald sphere, shown in Figure 2.9. For a sample with cylindrical symmetry, the reciprocal lattice point $G_{hkl}$ is decomposed into a ring of radius $G_{xy}$ and height $G_z$, which is a function of sample azimuth $\varphi$ as below:

$$G_{xy} = \left(G_x^2 + G_y^2\right)^{\frac{1}{2}}, \qquad G_z = G_z, \qquad G = \left(G_{xy}^2 + G_z^2\right)^{\frac{1}{2}}, \qquad G \cong |G_{hkl}|$$
$$G_x = G_{xy}\cos\varphi, \qquad G_y = -G_{xy}\sin\varphi \tag{2.62}$$

Here, angle $\varphi$ is defined to be zero on the $Q_{x,lab}$ axis and positive clockwise. $\varphi_E$ is obtained from the diffraction condition where the $G_{hkl}$ ring intersects the Ewald sphere by rotating $G_{hkl}$ about the sample plane normal:

$$\varphi_E = \arcsin\left(\frac{G^2}{G_{xy}}\frac{1}{\cos\alpha_i} - \frac{G_z}{G_{xy}}\tan\alpha_i\right) \tag{2.63}$$

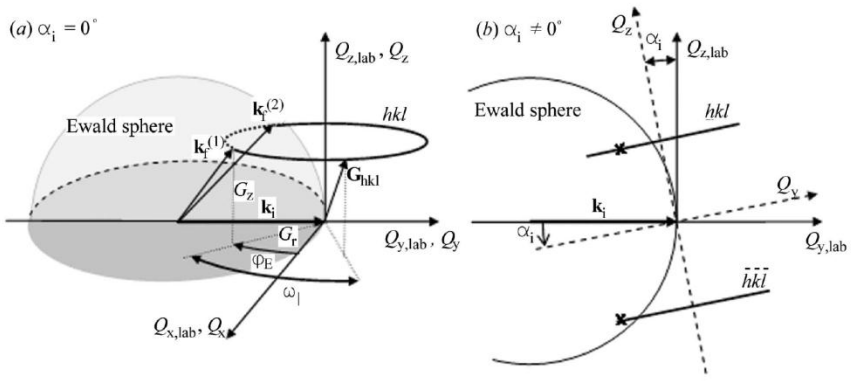


Figure 2.9 Diffraction condition for samples with cylindrical symmetry.[22]

Once $\varphi_E$ is obtained, the components $G_x$, $G_y$, and $G_z$ can be easily calculated from the above equations, resulting in the scattering vector, $Q_x$, $Q_y$, and $Q_z$. It is noticed that the diffraction techniques at grazing angle do not represent the intensity of the true Bragg scattering along $Q_z$, since the Bragg condition is not met for crystallites that are perfectly aligned with respect to the substrate normal.[28,29]

2.3.3.2 Intensity calculations

The intensity $I_{hkl}$ of the diffraction peaks in GIXD geometry can be described by the following equation:

$$I_{hkl}(Q) = \sum_{W^i}\left[C\ P\ L\ |F(Q)|^2\ M_j\ \Omega\right] \tag{2.64}$$

where the sum runs over all crystallite orientations $W^i$ and $C$ denotes a constant that depends on the incident flux along with other factors.

The Lorentz factor, $L$, corresponds to the Jacobian of the transformation from angular space to q space. For the in-plane diffraction and rod scans other than the specular rod, where the rocking angle is the azimuth $\varphi$, $L$ can be expressed as:

$$L = 1/[\cos\alpha \sin\psi \cos\beta] \tag{2.65}$$

Here, $\alpha$ represents the incidence angle; $\psi$, the in-plane scattering angle; and $\beta$, the exit angle (or out-of-plane scattering angle). For the specular rod *(h00)* with $\psi=0$, the rocking angle is the incident angle $\alpha$. Thus, the usual Lorentz factor can be used:

$$L = 1/\sin 2\alpha \tag{2.66}$$

The polarization factor, *P*, for a synchrotron source arises from the electrons in a synchrotron orbit in the horizontal plane, and accounts for the polarization of the emitted X-rays. The appropriate polarization factor for an unpolarized source, i.e. isotropic, is written as:

$$P = \frac{1}{2}(1 + \cos^2 2\theta) \tag{2.67}$$

For the vertical scattering geometry with the surface normal approximately parallel to the polarization vector, it can be expressed as:

$$P = \cos^2 \beta \cos^2 \psi + \sin^2 \beta \tag{2.68}$$

The structure factor, *F(Q)*, describes how an incident beam is scattered by the atoms of a crystal unit cell. *F(Q)* is given by the following equation:

$$F(Q) = \sum_i f_i(Q) \exp[2\pi i(hx_i + ky_i + lz_i] \tag{2.69}$$

where *Q*, the scattering vector; $\overline{r_i} = (x_i, y_i, z_i)$, the relative atomic positions; and *h*, *k*, *l* are the Miller indices. $f_i(Q)$ is the atomic form factor and the Fourier transform of the scattering density. Therefore, the atomic form factor is related to the scattering density distribution in an atom. A Cromer-Mann expansion approach is used to describe the

atomic form factor as a function of energy. Note that the structure factor squared is proportional to the intensity of the diffracted peaks.

$M_j$ in equation (2.64) is the Debye-Waller factor, also known as the temperature factor, and is equal to $exp(-Q^2\langle u^2\rangle)$. Here, $u$ is the input parameter defining the root mean square displacement of atoms induced by static disorder and thermal vibrations.

$\Omega$ in equation (2.64) is a correction for preferred orientation and can be described by two orientation angles, $\omega_{||}$ (azimuth) and $\omega_{\perp}$ (polar angle). $\omega_{||}$ and $\omega_{\perp}$ correspond to the angular deviations of the crystallites from the average orientation with respect to the in-plane axis of preferred orientation and sample normal, respectively, and are obtained from:

$$\omega_{\parallel} = \varphi_E - \varphi_0 = \varphi_E - \arctan\left(\frac{G_{hkl,y}}{G_{hkl,x}}\right) \tag{2.70}$$

$$\omega_{\perp} = \chi_E - \chi_0 = \chi_E - \arccos\left(\frac{G_{D,z}}{G_D}\right) \tag{2.71}$$

where $G_D$ is the reciprocal lattice vector for the average orientation. Therefore $\omega_{||}$ is the in-plane difference angle between the orientations that satisfy diffraction ($\varphi_E$) and the actual orientation ($\varphi_0$) and $\omega_{\perp}$ is the out-of-plane angle between the actual intersection with the Ewald sphere ($\chi_E$) and actual orientation ($\chi_0$).

For the biaxial model, the crystallite orientational distribution functions (ODF) can be given by the product of two Gaussian functions:

$$\Omega\,(W_{\parallel}, W_{\perp}) = \frac{1}{N}\exp(\frac{-2ln2\omega_{\parallel}^2}{W_{\parallel}^2})\exp(\frac{-2ln2\omega_{\perp}^2}{W_{\perp}^2}) \quad (2.72)$$

The parameters $W_{||}$ and $W_{\perp}$ are input values controlling the in-plane and out-of-plane degree of orientations, respectively, and $N$ is a normalization factor. $W_{||}$ and $W_{\perp}$ correspond to the FWHM (full-width at half-maximum) in Gaussian functions. For example, $W_{||}$ and $W_{\perp}$ go to infinity for an isotropic sample and zero for a single crystal. Uniaxial orientation with a preferred vertical axis is obtained by $W_{\parallel} \to \infty$ while moderate biaxial orientation is achieved by $W_{\parallel} \cong W_{\perp} \cong 5{\sim}30°$.

## 2.4 References


(1) Shanker, R. *Principles of quantum mechanics*; 2nd ed.; Springer: New York, 1994.

(2) Szabo, A.; Ostlund, N. S. *Modern quantum chemistry: Introduction to advanced electronic structure theory*; Dover Publications, Inc.: Mineola, NY, 1996.

(3) Cramer, C. J. *Essentials of computational chemistry: Theories and models.*; 2nd ed.; Wiley: Hoboken, NJ, 2004.

(4) Frenkel, D.; Smit, B. *Understanding molecular simulation*; 2nd ed.; Academic Press: San Diego, CA, 2002.

(5) Allen, M. P.; Tildesley, D. J. *Computer simulation of liquids*; Oxford University Press: New York, 1989.

(6) Patnaik, S. S.; Farmer, B. L. *Polymer* **1992**, *33*, 4443.

(7) Becke, A. D. *Phys. Rev. A* **1988**, *38*, 3098.

(8) Becke, A. D. *J. Chem. Phys.* **1993**, *98*, 5648.

(9) Lee, C.; Yang, W.; Parr, R. G. *Phys. Rev. B* **1988**, *37*, 785.

(10) Pearlman, D. A.; Case, D. A.; Caldwell, J. W.; Ross, W. S.; Cheatham, T. E.; Debolt, S.; Ferguson, D.; Seibel, G.; Kollman, P. *Comput. Phys. Commun.* **1995**, *91*, 1.

(11) Brooks, B. R.; Bruccoleri, R. E.; Olafson, B. D.; States, D. J.; Swaminathan, S.; Karplus, M. *J. Comput. Chem.* **1983**, *4*, 187.

(12) Scott, W. R. P.; Hunenberger, P. H.; Tironi, I. G.; Mark, A. E.; Billeter, S. R.; Fennen, J.; Torda, A. E.; Huber, T.; Kruger, P.; van Gunsteren, W. F. *J. Phys. Chem. A* **1999**, *103*, 3596.

(13) Hagler, A. T.; Huler, E.; Lifson, S. *J. Am. Chem. Soc.* **1974**, *96*, 5319.

(14) Sun, H.; Ren, P.; Fried, J. R. *Comput. Theor. Polym. Sci.* **1998**, *8*, 229.

(15) Allinger, N. L. *J. Am. Chem. Soc.* **1977**, *99*, 8127.

(16) Allinger, N. L.; Yuh, Y. H.; Lii, J. H. *J. Am. Chem. Soc.* **1989**, *111*, 8551.

(17) Rappe, A. K.; Casewit, C. J.; Colwell, K. S.; Goddard, W. A.; Skiff, W. M. *J. Am. Chem. Soc.* **1992**, *114*, 10024.

(18) Mayo, S. L.; Olafson, B. D.; Goddard, W. A. *J. Phys. Chem.* **1990**, *94*, 8897.

(19) Lee, F. S.; Chu, Z. T.; Warshel, A. *J. Comput. Chem.* **1993**, *14*, 161.

(20) Rappe, A. K.; Goddard, W. A. *J. Phys. Chem.* **1991**, *95*, 3358.

(21) Jens, A. N.; Des, M. *Elements of modern x-ray physics*; Wiley: New York 2001.

(22) Breiby, D. W.; Bunk, O.; Andreasen, J. W.; Lemke, H. T.; Nielsen, M. M. *J. Appl. Crystallogr.* **2008**, *41*, 262.

(23) Breiby, D. W.; Chin, P. T. K.; Andreasen, J. W.; Grimsrud, K. A.; Di, Z. Y.; Janssen, R. A. J. *Langmuir* **2009**, *25*, 10970.

(24) Cho, E.; Risko, C.; Kim, D.; Gysel, R.; Miller, N. C.; Breiby, D. W.; McGehee, M. D.; Toney, M. F.; Kline, R. J.; Bredas, J. L. *J. Am. Chem. Soc.* **2012**, *134*, 6177.

(25) Smilgies, D. M. *Rev. Sci. Instrum.* **2002**, *73*, 1706.

(26) Smilgies, D. M.; Blasini, D. R. *J. Appl. Crystallogr.* **2007**, *40*, 716.

(27) Busing, W. R.; Levy, H. A. *Acta Crystallogr* **1967**, *22*, 457.

(28) Chabinyc, M. L. *Polym. Rev.* **2008**, *48*, 463.

(29) Baker, J. L.; Jimison, L. H.; Mannsfeld, S.; Volkman, S.; Yin, S.; Subramanian, V.; Salleo, A.; Alivisatos, A. P.; Toney, M. F. *Langmuir* **2010**, *26*, 9146.

# CHAPTER 3

# MOLECULAR MODELING OF PACKING STRUCTURE AND ELECTRONIC PROPERTIES OF BIAXIALLY-ORIENTED POLY(2,5-BIS(3-ALKYLTHIOPHENE-2-YL) THIENO[3,2-B]THIOPHENE) FILMS

## 3.1 Introduction

Supramolecular organization of the conjugated semicrystalline polymers plays an important role in determining device performance of bulk-heterojunction (BHJ) solar cells. Poly (2,5-bis (3–alkyl thiophene–2–yl) thieno [3,2-b] thiophene) (PBTTT-$C_n$)[1-9] (see Figure 3.1) has been reported as a promising polymer semiconductor for organic electronics due to a large hole mobility (up to 1 $cm^2v^{-1}s^{-1}$)[10-12] and highly ordered structure. PBTTT-$C_n$ consists of conjugated backbones composed of a thienothiophene unit appended on each side by a single thiophene unit that contains a long alkyl side chain (typically ranging from $C_8H_{17}$ to $C_{18}H_{37}$). Here, the backbones play a critical role in the structural rigidity and electrical transport, and the side-chains provide for better solubility. PBTTT-$C_n$ can self-assemble into lamellar structures due to the presence of the long alkyl side-chains.[13] The alkyl side-chains on a polymer backbone lead to the formation of lamellar structures in thin films. This provides long-range π-stacking order in the films, which ultimately affects the charge-transport properties.[14] Therefore, understanding details concerning the polymer structure and packing is important to understand the relationships between crystalline structure and electrical properties.

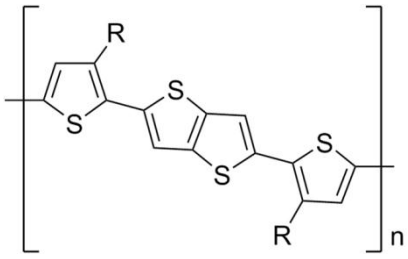


Figure 3.1 Chemical structure of poly (2,5-bis (3–alkyl thiophene–2–yl) thieno [3,2-b] thiophene) (PBTTT-$C_n$ with $C_n$=$C_8$-$C_{18}$).

In this study, we have established a detailed structural model of PBTTT-$C_n$ (n=12, 14, 16) using a combination of computational modeling and 2D grazing incidence X-ray diffraction (GIXD) simulations based on the experimental GIXD data of well-ordered (biaxially-aligned) polymer films. We note that all experimental GIXD data were obtained from Dr. R. Joseph Kline at the National Institute of Standards and Technology (NIST), Dr. Michael F. Toney at Stanford Synchrotron Radiation Lightsource (SSRL), and Prof. Michael D. McGehee at Stanford University. This methodology allows us to confirm how the polymer components (i.e., backbone and side chains) contribute to the total diffraction pattern, and how changes in molecular orientation influence the diffraction pattern. Moreover, we examine how the length of the alkyl side chains, going from $C_{12}H_{25}$ to $C_{14}H_{29}$ and $C_{16}H_{33}$, affects the molecular packing. Finally, we evaluate the influence of these parameters on the electronic band structure and intermolecular electronic couplings, which are directly associated with the charge-transport performance.

## 3.2 Computational methodology

The initial crystal geometry for each polymer in the PBTTT-$C_n$ series was taken as one monomer in a unit cell of varying lattice parameters and periodic boundary conditions; the *a*-axis of the unit cell was defined as the lamellar growth direction, the *b*-axis as the backbone-stacking direction, and the *c*-axis as the monomer repeat direction along the polymer chain. Each polymer consisted of a planar backbone with the thiophene moieties oriented in anti-configurations and interdigitated alkyl side-chains, as previously suggested.[15] All molecular mechanics calculations were performed with the Materials Studio software suite. Atomic charges were assigned via the COMPASS force field. The polymer crystal structures were optimized with the Universal Force Field (UFF).[16] Non-bonded interactions in the crystal structures were calculated by the Ewald method with an energy accuracy of $10^{-4}$ kcal/mol.[17]

The optimized polymer crystal packing motifs were used to simulate the 2D grazing incidence X-ray diffraction (GIXD) patterns using the simDiffraction code.[18,19] An incident X-ray wavelength of 0.975 Å (corresponding to an incident energy of 12.7 keV), a fixed incidence angle of 0.1°, and peak width of 0.02 $Å^{-1}$ were used for the simulations. The *a** direction of crystal unit cell, i.e. *(h00)* planes of the crystalline domains, is set to be oriented parallel to the substrate since previous experiment found edge-on orientation.[1,2] In the simulation, we took into account the Lorentz factor, in-plane polarization factor, correction for preferred orientation, and Debye-Waller factor (u=0.2 Å), as described in the literature.[18] The parameters for the in-plane ($W_{\parallel}$) and out-of-plane ($W_{\perp}$) orientations were set to infinity and 2°, respectively, for uniaxially-aligned films,

and 30° and 5° for biaxially-aligned films, respectively, to reflect the thin-film orientational distribution.

Three force fields, UFF,[16] COMPASS,[20] and Dreiding,[21] were evaluated to find the most appropriate force field able to predict the packing structure of PBTTT-$C_n$. Specifically, the crystal structure of PBTTT-$C_{12}$ was fully optimized using each force field; the GIXD patterns simulated from each optimized structure are compared to the experimental ones (Figure 3.2 and Table 3.1). As shown in Figure 3.2, the GIXD patterns of the structures obtained using UFF and COMPASS showed trends similar to the experimental data, while the GIXD pattern of that optimized by Dreiding produced quite different spots in the range of $Q_{xy} < 1.5$ Å$^{-1}$. In terms of detailed structural information for each structure, UFF underestimated the lamellar d-spacing compared to COMPASS, see Table 3.1. In contrast, COMPASS provided a shorter polymer length repeat unit compared to experiment, which is an unphysical result regarding the features of repeated polymer. From these analyses, UFF was determined to be the most suitable force field to determine the PBTTT-$C_{12}$ structures. Therefore, UFF was used to further study the molecular structures of PBTTT-$C_n$.

Although UFF provided reasonable agreement with experimental data compared to the other force fields, there were still discrepancies between the simulated and experimental GIXD patterns in terms of lamellar spacing and exact peak positions. Therefore, we varied the lattice parameters and fully optimized the polymer structure. The GIXD patterns of the new structures were then simulated and compared to experiment, which

allowed us to eventually refine the unit-cell parameters and packing structure of the polymer.

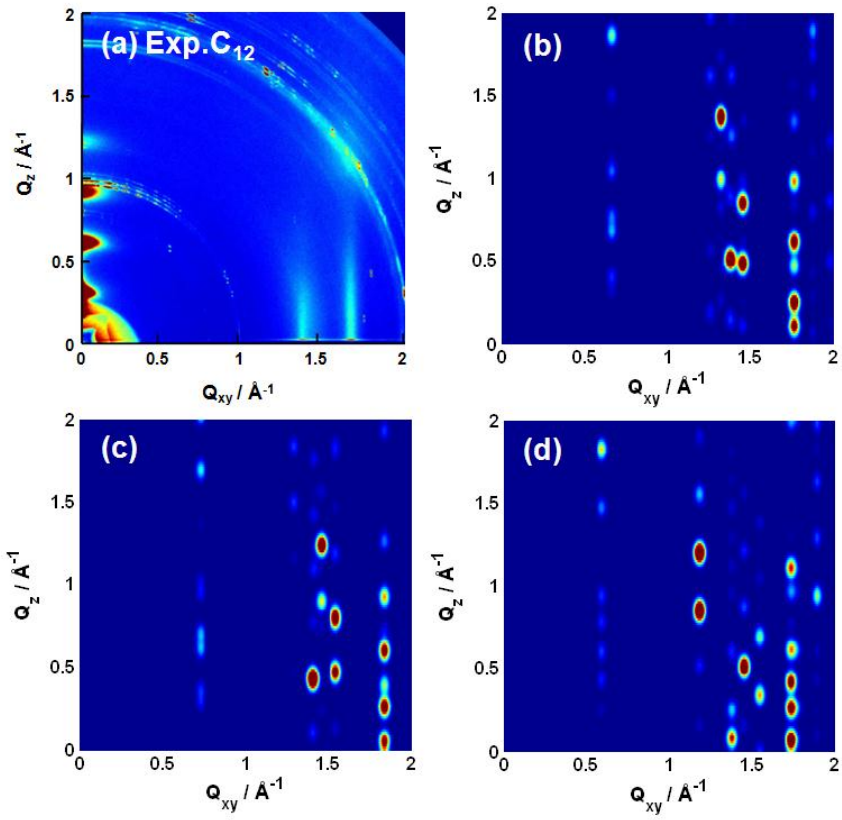


Figure 3.2 2D GIXD patterns of structures of PBTTT-$C_{12}$: experimentally measured[14] (a) and simulated from fully relaxed structures using UFF (b), COMPASS (c), and Dreiding (d) force fields. Dotted ellipses on the experimental spectra are transposed to the simulated spectra to serve as a guide to the eye.

Table 3.1 Structural characteristics of the PBTTT-$C_{12}$ crystal optimized using various force fields.

| PBTTT-$C_{12}$ | Lattice parameters | | | | | | Lamellar-spacing (Å) | π-stacking (Å) |
|---|---|---|---|---|---|---|---|---|
| | *a* (Å) | *b* (Å) | *c* (Å) | α (°) | β (°) | γ (°) | | |
| Experiment | 19.1 | 3.7 | 13.6 | 90 | 90 | 90 | 19.1 | 3.6 |
| UFF | 17.4 | 5.0 | 13.5 | 135 | 93 | 82 | 17.2 | 3.5 |
| COMPASS | 19.2 | 4.9 | 12.4 | 136 | 94 | 81 | 18.9 | 3.4 |
| Dreiding | 19.3 | 4.6 | 13.5 | 128 | 94 | 72 | 18.1 | 3.6 |

We performed DFT calculations to evaluate the electronic properties of the optimized polymers where the molecular geometries were taken from the refined model without further geometry optimization. Intermolecular transfer integrals (electronic couplings) between adjacent polymer chains were determined using the B3LYP functional and the 6-31G(d,p) basis set with the Gaussian 09 program suite;[22] detailed computational methods are described elsewhere in the literature.[23] Electronic band structures were determined using DFT at the B3LYP/6-31G(d) level with the CRYSTAL06 program;[24] the Monkhorst−Pack scheme with a 2×8×4 k-point mesh in the Brillouin zone was applied.

## 3.3 Results and discussion

### 1.1.1 Uniaxially-aligned PBTTT-$C_{14}$ films

While empirical and theoretical models of PBTTT thin films provide important details concerning the polymer structure and packing,[2,14,15,25-27] there remain a number of dissimilarities among the models, and the overall agreement with GIXD data is incomplete. For example, the unit cell for PBTTT-$C_{14}$ has been reported as an

orthorhombic unit cell with $a$ = 22.15 Å, $b$ = 3.67 Å, $c$ = 13.37 Å, $\alpha = \beta = \gamma = 90°$,[2] while simulations have shown that PBTTT-$C_{12}$ is triclinic lattice with $a$ = 19.6 Å, $b$ = 5.4 Å, $c$ = 13.6 Å, $\alpha$ = 136°, $\beta$ = 84°, $\gamma$ = 86°.[15] In order to develop a robust structural model for PBTTT, we considered first experimental uniaxially-aligned polymer films where there are strong orientations with respect to the substrate normal and random in-plane orientations. Using a theoretical methodology based on the experimental data, the packing structure of PBTTT-$C_{14}$ was determined (at 0 K) as shown in Figure 3.3.[28]

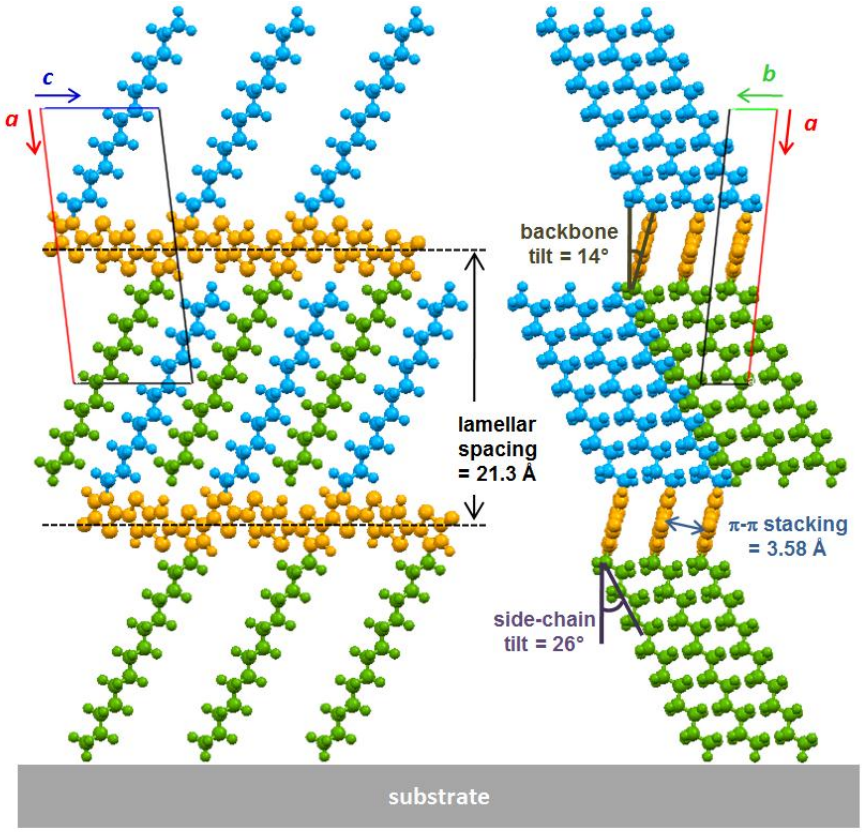


Figure 3.3 Out-of-plane packing motifs for the simulated model of PBTTT-$C_{14}$ viewed along the *b*-axis (left) and *c*-axis (right); the color coding is such that orange represents the polymer backbones and blue and green represent the side chains attached above and below the backbones, respectively. The substrate is shown to indicate the polymer film orientation, as it is not completely known how the PBTTT layer next to the substrate is aligned.

The unit-cell is triclinic, with unit-cell parameters a = 21.5 Å, *b* = 5.4 Å, *c* = 13.5 Å, α = 137°, β = 86°, γ = 89°. These unit-cell parameters are similar to those previously proposed for PBTTT-$C_{12}$.[15] It is clear that the conjugated backbones are planar and inter-backbone stacking distance (π-stacking distance) is relatively short, 3.58 Å, which can lead to strong π-π interactions; these two features are susceptible to be result in efficient intra-and inter-chain charge transfer along the *c*- and *b*-axis, respectively. The planar backbones have a slight tilt (14°) of the short backbone axis with respect to the substrate normal; this tilt is in reasonable agreement with, though somewhat smaller than, the backbone tilt (21° ± 3°) obtained from NEXAFS.[13] We note that the NEXAFS measurement is an azimuthal average of unknown orientation distribution and requires the assumption of a single, narrow tilt distribution to calculate the tilt angle; if disorder is present in the film, the estimated tilt will shift towards the magic angle (54.7°) and result in an estimated tilt larger than that in the ordered regions. The interdigitated alkyl side chains are straight, leading to the formation of lamellar structures with a d-spacing of 21.3 Å. The tilt of the side chains from the substrate normal is 26°. This result is substantially smaller than the 45° tilt determined from polarized infrared (IR) spectroscopy[13] but closer to the value of 37° tilt estimated with GIXD from the change of lamellar spacing with side chain length.[14] As was previously described for NEXAFS, IR spectroscopy also measures an azimuthal average of an unknown distribution and this skews the estimated tilt angle towards the magic angle of 54.7° when disorder is present, as for semicrystalline polymers. Therefore the IR-derived tilt is likely overestimated for the PBTTT. The sensitivity of the simulated GIXD pattern to side-chain tilt will be discussed in more detail below. In general, there is good agreement among the

experimentally-determined and modeled orientation and distance parameters. Overall, PBTTT-$C_{14}$ shows very well-ordered orientations of backbones and side-chains. The simulated GIXD pattern is compared to experiment in Figure 3.4 and Table 3.2. The simulated 2D GIXD patterns are represented in a space spanned by $Q_{xy}$ (the component of scattering vector parallel to the substrate) and $Q_z$ (the component of scattering vector perpendicular to the substrate). There is no observable *(h00)* Bragg peaks, since the crystal unit cell was set to be well aligned with respect to the substrate plane.[29] We find good agreement between the experimental and simulated data, with strong peaks at $Q_{xy}$=1.41 and 1.71 $Å^{-1}$ reflecting the lateral ordering of the polymer films.

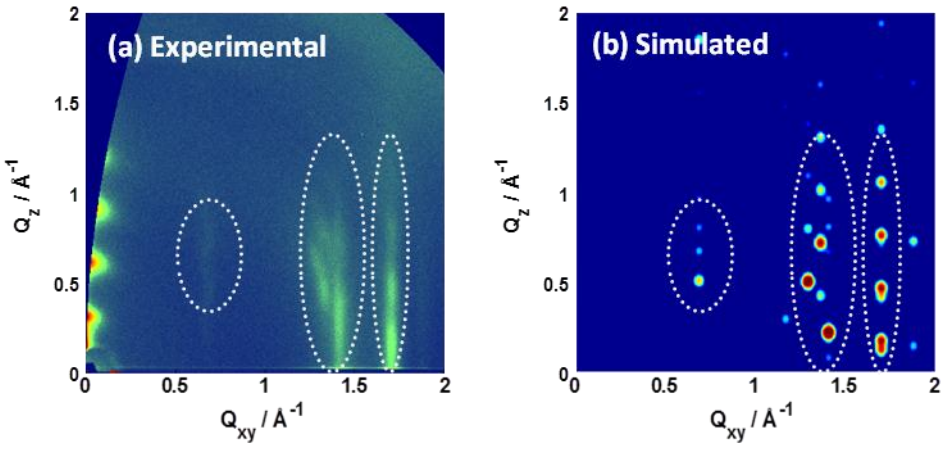


Figure 3.4 Experimental (a) and simulated (b) GIXD patterns of PBTTT-$C_{14}$ with random in-plane orientation. Dotted ellipses on the experimental diffraction pattern are transposed to the simulated spectra to serve as a guide to the eye. All intensities are shown on a logarithmic scale.

Table 3.2 Indexing of the intense peaks in uniaxial PBTTT-$C_{14}$. The experimental error bars for $Q_{xy}$ are ±0.01 $Å^{-1}$.

| Experiment | | Simulated model | |
|---|---|---|---|
| $Q_{xy}$ ($Å^{-1}$) | *(hkl)* | $Q_{xy}$ ($Å^{-1}$) | $Q_z$ ($Å^{-1}$) |
| 1.29 | *(21-1)* | 1.29 | 0.50 |
| 1.35 | *(302)* | 1.37 | 0.72 |
| 1.41 | *(1-13)* | 1.41 | 0.22 |
| 1.71 | *(0-10)* | 1.71 | 0.17 |
| | *(110)* | 1.71 | 0.12 |
| 1.71 | *(1-10)* | 1.71 | 0.47 |
| | *(210)* | 1.71 | 0.42 |
| 1.71 | *(2-10)* | 1.71 | 0.76 |

### 3.3.1 Biaxially-aligned PBTTT-$C_{14}$ films

Biaxial films of PBTTT-$C_{14}$ were obtained from a flow coating process with thermal treatment that can control the backbone orientation in plane, leading to a situation where the polymer backbones are preferentially aligned along one direction and lamellae domains are strongly oriented along *a**.[27] Figure 3.5 depicts the in-plane orientation via a top-view derived from the UFF-modeled unit cell. The polymer backbones (orange) are well-aligned within the *b*-*c* plane (parallel to the substrate plane). Interestingly, the conjugated backbones are displaced by 3.68 Å (from a perfect cofacial orientation) with respect to their neighbors along the long axis, while maintaining a short inter-backbone packing distance (3.58 Å). We note that this displacement along the long axis differs from previous results obtained with DFT,[25] which has a direct impact on the description of the electronic properties of the polymer (see below). The alkyl side chains have a preferential in-plane rotation with respect to the backbone of about 58°.

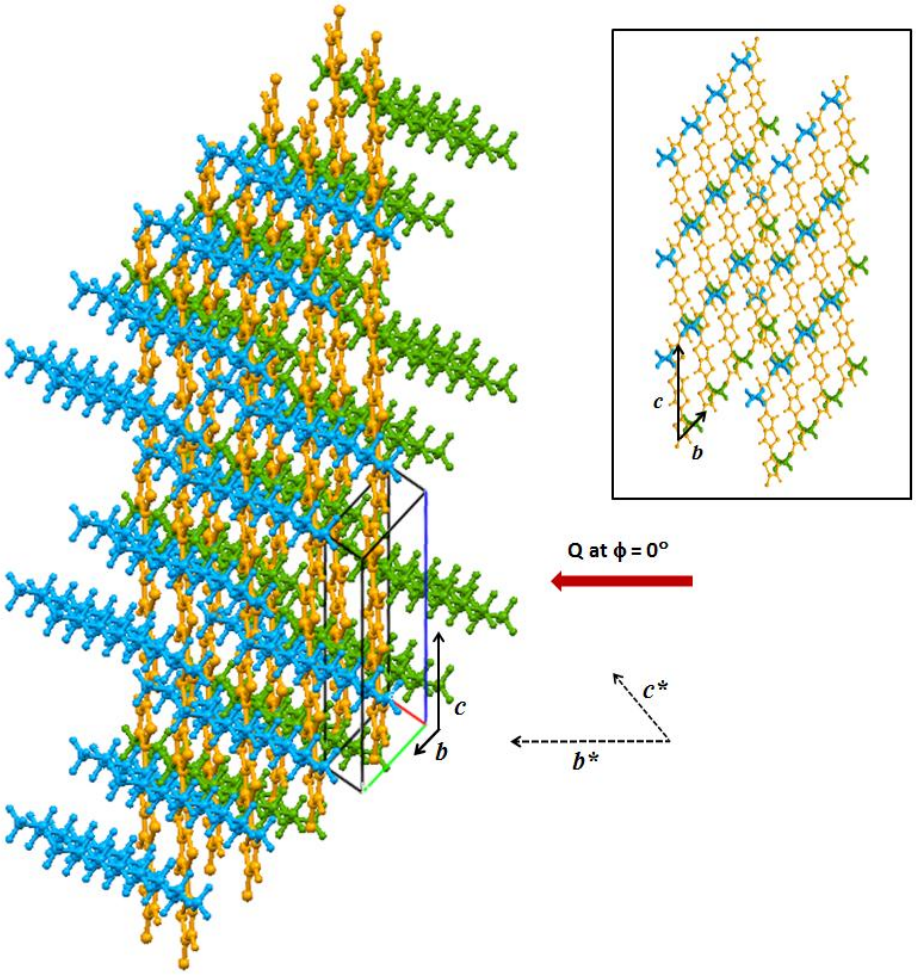


Figure 3.5 In-plane orientation of the PBTTT-$C_{14}$ model viewed along the *a**-axis. Orange represents the polymer backbones; blue and green represent the side chains attached above and below the backbones, respectively; solid and dotted arrows indicate axes of direct and reciprocal lattice, respectively; a thick red arrow represents the scattering vector Q at the azimuthal angle $\phi = 0°$ for the GIXD data. The inset highlights the molecular structure viewed along the side chains to clearly show the backbone orientations relative to the side chains.

The in-plane orientation of the biaxial films can be detected by GIXD measurements. As stated earlier, the azimuthal angle ($\phi$) is the angle between the in-plane component of scattering vector ($Q_{xy}$) and the in-plane component of ***b****. At 0°, the *(h10)* peaks corresponding to the inter-chain backbone stacking are strongly observed. However, the

specific reflections that occur at various ϕ angles (*e.g.*, 45° and 90°) depend on the unit-cell parameters for the triclinic cell. For example, the *(h01)* peaks appear near angle ϕ=α*, the angle between *b** and *c**. Thus, GIXD simulations were performed at different in-plane orientations (azimuthal angles ϕ) to confirm the validity of the detailed in-plane packing of the PBTTT-$C_{14}$ model.

Figure 3.6 and Table 3.3 display the empirical and simulated GIXD patterns and peak positions for the biaxial films at various azimuthal angles. The simulated patterns show good agreement with the experimental data in terms of dominant peak positions. At the azimuthal angle ϕ=0° (backbones parallel to the beam direction), the *(h10)* peaks appear strong at $Q_{xy}$=1.71 $Å^{-1}$ with intensity along $Q_z$. As Figure 3.7 shows, the $Q_z$ values for *(h10)* peaks obtained from the simulation are consistent with the (broader) experimental peaks. In this region, each spot comes from a contribution of two reflection planes; the peaks at $Q_z$=0.15 $Å^{-1}$ are from the (0-10) and (110) planes, those at $Q_z$=0.47 $Å^{-1}$ from the (1-10) and (210) planes, and those at $Q_z$=0.79 $Å^{-1}$ from the (2-10) and (310) planes. The difference between any two pairs of reflection planes along $Q_z$ is only 0.05 $Å^{-1}$, so the two peaks appear as a single broader peak. As the simulated GIXD pattern shows distinct spots for the aligned crystalline domains, it is anticipated that stacking faults and disorder in the films are the cause for the smeared and broad peaks present in the experimental data; indeed, X-ray line-shape analysis of PBTTT reveals considerable paracrystalline disorder along the π-π stacking direction, which can influence the charge-transport properties.[30] Because of the broad in-plane orientation distribution, the (21-1) reflection is also observed even though it is centered at ϕ=14° in the simulations. Additionally,

analyses of the simulated GIXD patterns provide a clear interpretation of the intense peaks at $\phi$ = 45° and 90°. At 45°, the (201) and (302) peaks are intense as $\alpha^*$=48°, thus the scattering vector lies nearly parallel to the **c*** direction at this azimuthal angle; at 90°, the mixed reflection planes (1-13) and (3-14) appear.

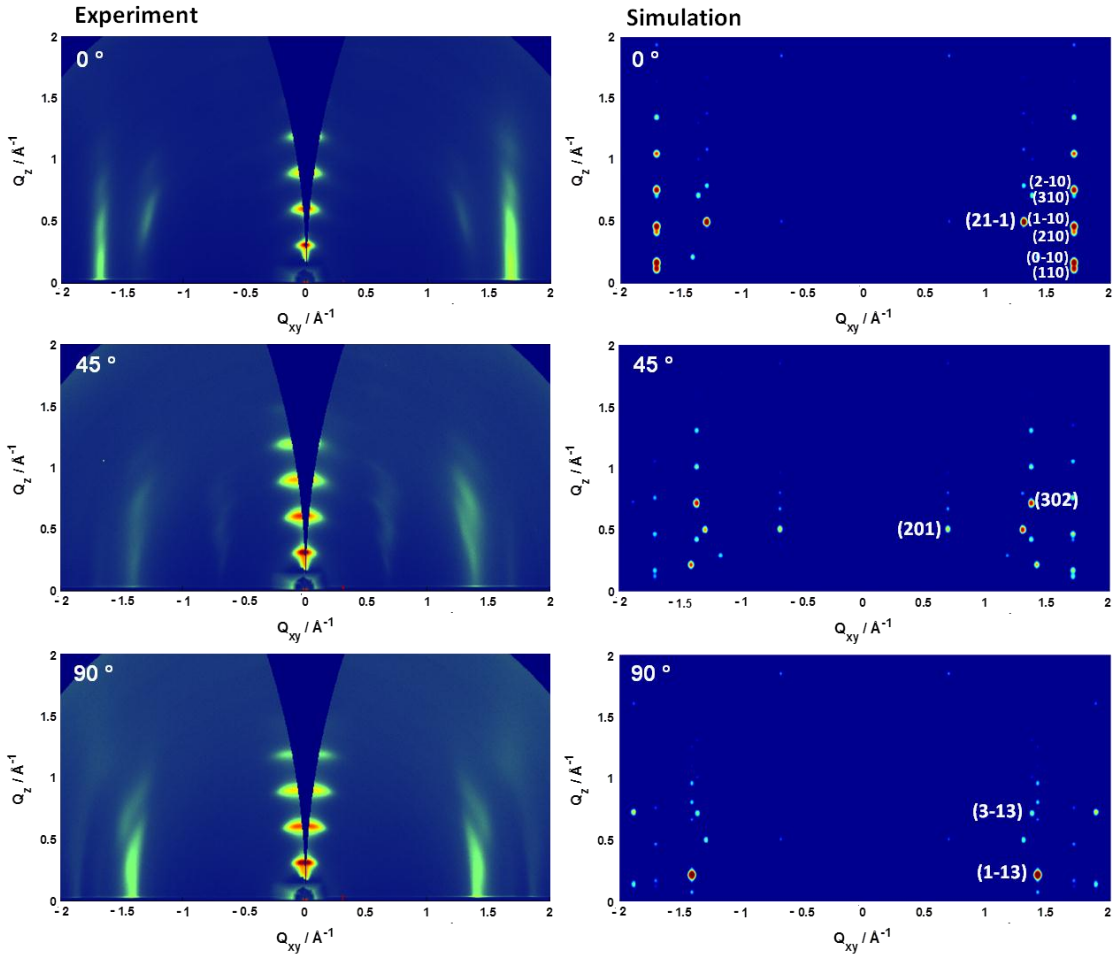


Figure 3.6 Comparison of experimental (left) and simulated (right) GIXD patterns of biaxial PBTTT-$C_{14}$ films at various azimuthal angles ($\phi$=0°, 45°, 90°) with respect to the incident beam direction. The experimental diffraction images at 0° and 90° are not symmetric since the samples are aligned with ±2° deviation. When the samples are misoriented, you can see asymmetry in the films. The peaks near 45° are much broader than the peaks near 0° or 90°. Intensities are shown on a logarithmic scale.

Table 3.3 GIXD peak indexation for the experimental and simulated biaxial PBTTT-$C_{14}$ films at various azimuthal angles ($\phi$=0°, 45°, 90°) with respect to the incident beam direction. The experimental error bars for $Q_{xy}$ are ±0.01 $Å^{-1}$.

| $\phi$ | Experiment | | Simulated model | | |
|---|---|---|---|---|---|
| | $Q_{xy}$ ($Å^{-1}$) | $Q_z$ ($Å^{-1}$) | *(hkl)* | $Q_{xy}$ ($Å^{-1}$) | $Q_z$ ($Å^{-1}$) |
| 0° | 1.29 | 0.50 | *(21-1)* | 1.29 | 0.50 |
| | 1.71 | 0.15 | *(0-10)* | 1.71 | 0.17 |
| | | | *(110)* | 1.71 | 0.12 |
| | 1.71 | 0.47 | *(1-10)* | 1.71 | 0.47 |
| | | | *(210)* | 1.71 | 0.42 |
| | 1.71 | 0.79 | *(2-10)* | 1.71 | 0.76 |
| | | | *(310)* | 1.71 | 0.71 |
| 45° | 0.68 | 0.51 | *(201)* | 0.68 | 0.51 |
| | 1.35 | 0.73 | *(302)* | 1.37 | 0.72 |
| 90° | 1.41 | 0.30 | *(1-13)* | 1.41 | 0.22 |
| | 1.41 | 0.74 | *(3-13)* | 1.41 | 0.81 |

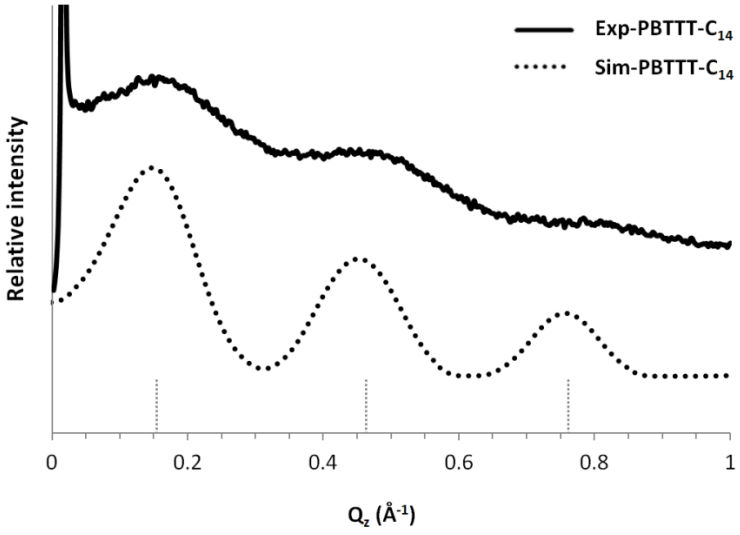


Figure 3.7 Experimental (solid line) and simulated (dotted line) plots of *(h10)* peak intensities at $Q_{xy}$=1.71 $Å^{-1}$ for PBTTT-$C_{14}$ vs $Q_z$; the short dotted vertical lines represent the expected $Q_z$ positions. The simulated data were broadened with a Gaussian function (FWHM=2*original FWHM).

### 3.3.2 Influence of molecular packing on diffraction patterns

Figure 3.8 displays the simulated GIXD patterns for the individual polymer components for three in-plane azimuthal angles. The contributions from each component of the polymer structure were evaluated by setting all atoms on the polymer component not of interest to be non-diffracting (*i.e.*, hydrogen-like). Contributions from the polymer backbones and from the side chains are readily identifiable**.** The backbones mainly contribute to the diffraction peaks at $Q_{xy}$=1.71 $Å^{-1}$ (π-stacking peaks), while the side chains make significant contributions to the peaks around $Q_{xy}$= 1.29 - 1.41 $Å^{-1}$. These results suggest that the degree of disorder for the different components plays a significant role in the intensity of the GIXD pattern. Indeed, one would expect *a priori* that diffraction peaks arising from the more flexible and disordered alkyl side chains would be weaker and more diffuse than those mainly arising from the conjugated backbone, a result borne out by the analysis of the partitioned structure. In terms of azimuthal angle dependence of the components, as we confirmed above, the diffraction images at 45° and 90° are principally influenced by the packing orientation of the side chains while the 0° image is mainly influenced by the backbone orientation with some contributions of side-chain packing. Interestingly, the intensity of the *(201)* reflection in the 45° image appears to be enhanced by the interference between the backbone and side-chain components as the simulation of the full polymer shows relatively intense peaks while the simulations of the individual components show weaker diffraction spots.

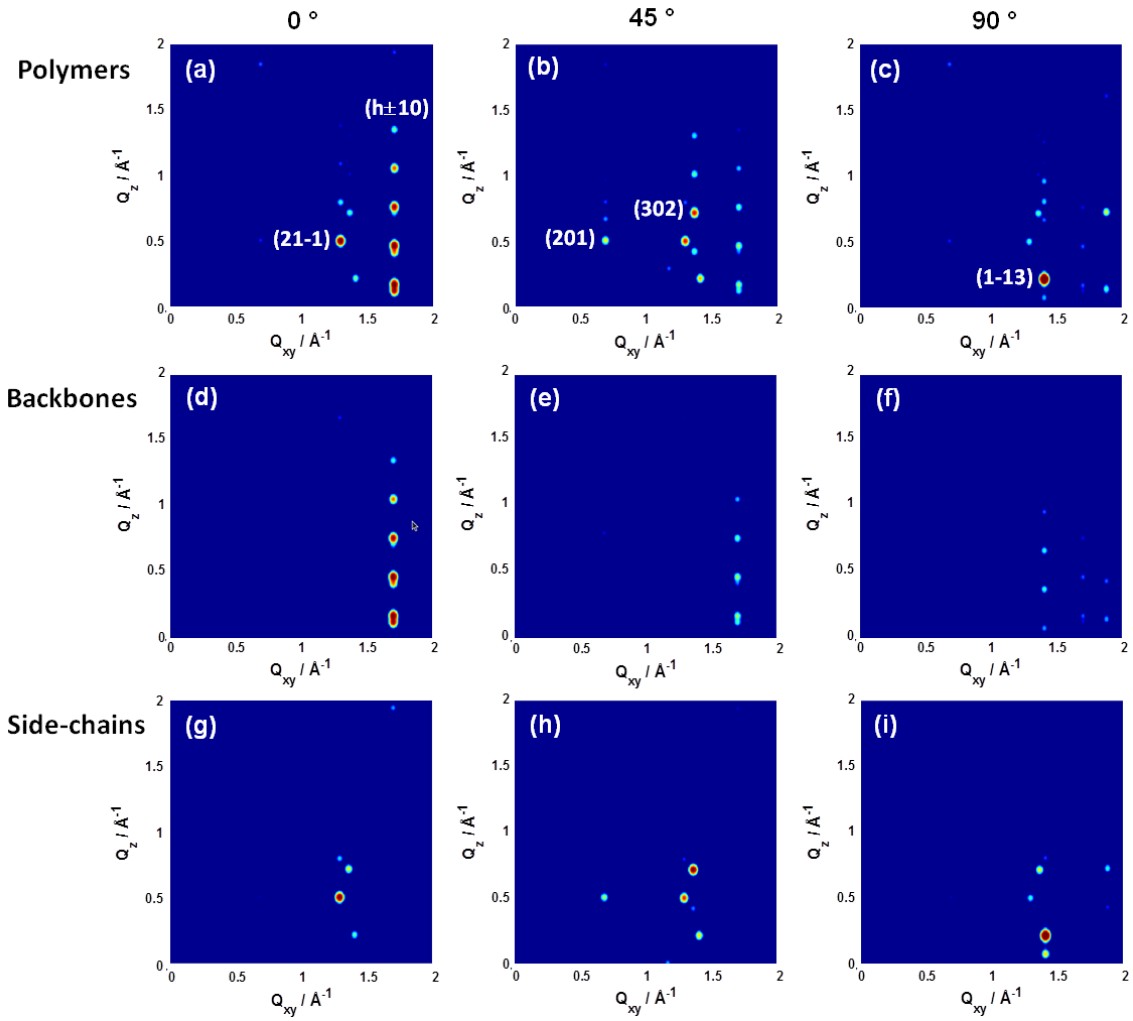


Figure 3.8 Simulated GIXD patterns at azimuthal angles (ϕ=0°, 45°, 90°) with respect to the incident beam direction for the biaxial PBTTT-$C_{14}$ polymer (a-c), backbone segments (d-f), and alkyl side-chain segments (g-i). Note that the intensity scales are the same for each plot. Intensities are shown on a logarithmic scale.

We then investigated further how these molecular packing parameters affect the GIXD patterns of the uniaxial films. First, we examined how the tilt of the backbones with respect to the substrate normal (14° simulation vs. 20° NEXAFS) affects the simulated diffraction patterns. A unit cell containing only the backbone was considered, as it was

noted above that the side chains do not contribute significantly to diffraction peaks related to the polymer backbones. The backbone tilt was changed from 10° to 30° via 5° increments within a fixed unit cell. As shown in Figure 3.9, the *(h10)* intensity profile for the uniaxial polymer films are similar when the backbone tilt is less than 20°; the peak at lower $Q_z$ appears more intense than the higher $Q_z$ peaks. When the backbone tilt is greater than 25°, however, the intensity of the higher $Q_z$ peaks becomes much stronger, a result not consistent with experiment. We note that the energetic differences among these structural variations are minor. These results show that the *(h10)* peaks are relatively insensitive to the change in the backbone tilt when the tilt is smaller than 25°. Thus, the 6° difference in tilt between simulation and NEXAFS data is within the error bars as there is no significant change both in the diffraction patterns and peak intensities with variation of the tilt in this range. These results reveal that there is likely considerable disorder in the backbone tilt angles (*ca*. 0° - 20°).

Second, in order to evaluate the effect of the side-chain orientation on the diffraction patterns, the tilt of the side chains in the unit cell was varied, though interdigitation between the side chains was maintained. These structures were not optimized, since after geometry optimization the tilt angle goes back to the original, energetically-stable state. As the side-chain tilt changes from 26° to 31° and 36°, the in-plane rotation of the side chains from the backbones also change from 58° to 85° and 86°. Figure 3.10 shows the GIXD pattern of the full polymer with varying side-chain tilt and that of only the side-chain part with peak indexes to clearly identify the diffraction peaks with respect to the tilt.

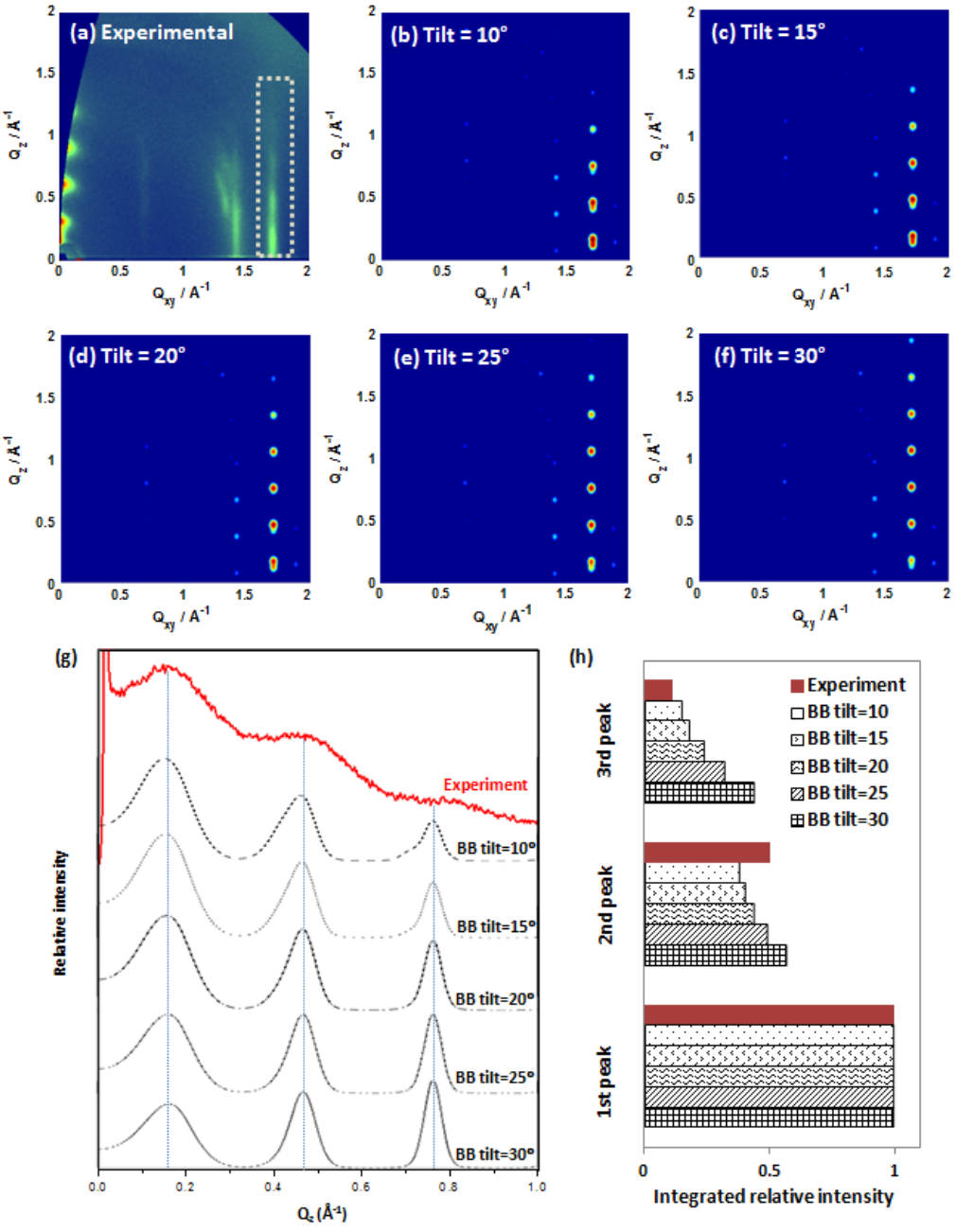


| BB tilt (°) | 10 | 15 | 20 | 25 | 30 |
|---|---|---|---|---|---|
| Unit cell energy (kcal/mol) | 49.18 | 49.23 | 49.75 | 51.46 | 56.15 |

Figure 3.9 Experimental (a) and simulated GIXD patterns of uniaxial backbone with tilt (b) 10°, (c) 15°, (d) 20°, (e) 25°, and (f) 30°, (g) plot of *(h10)* intensity of the peaks at $Q_{xy}$=1.71 Å$^{-}$1 vs. $Q_z$, (h) the integrated relative intensity of 1$^{st}$, 2$^{nd}$, and 3$^{rd}$ peaks of experiment and simulated model with various backbone tilt angles, and (i) energy of unit cell as a function of backbone tilt; a white box in the experimental data indicates the diffraction pattern coming from the backbone contribution. For 2D GIXD, intensities are shown on a logarithmic scale.

As shown in Figure 3.10, the change in side-chain tilt has a significant impact on the diffraction pattern. The simulated GIXD patterns lose their agreement with the experimental pattern ($Q_{xy} \approx 0.5$ - 1.5 $Å^{-1}$ and $Q_z \approx 0.0$ - 1.5 $Å^{-1}$) as the side-chain tilt changes from 26° (tilt of the optimized model) to 31° or 36°. Since the side-chain orientation is related to the backbone orientation and lamellar thickness, artificial modification of the side-chain tilt angle with respect to the substrate normal may not be relevant to prove the exact tilt angle of the side chains. Nevertheless, these results suggest that the side-chain arrangements significantly influence the polymer packing and diffraction peak intensities and positions. The disagreement in side-chain orientation between the IR experiment, and our GIXD data/simulation likely arises from the exclusion from the simulation of both side-chain disorder and the possibility of gauche defects along the alkyl chains. Additionally, as mentioned earlier, the side-chain tilts extracted from polarized IR spectroscopy would overestimate the tilt angle for this system when disorder is present. The tilt angle extracted from the GIXD measurements relates to the side chains in the interdigitated portion of the unit cell and is based on the assumption that the side-chain conformation is independent of side-chain length. The GIXD measurement also points to having a non-interdigitated region about 3 to 5 methylenes long.[14] Such non-interdigitated regions do not appear in the simulations since the molecular mechanics modeling does not include temperature-dependent contributions, which can result in an increase in the tilt angle when the lamellar d-spacing is held constant.

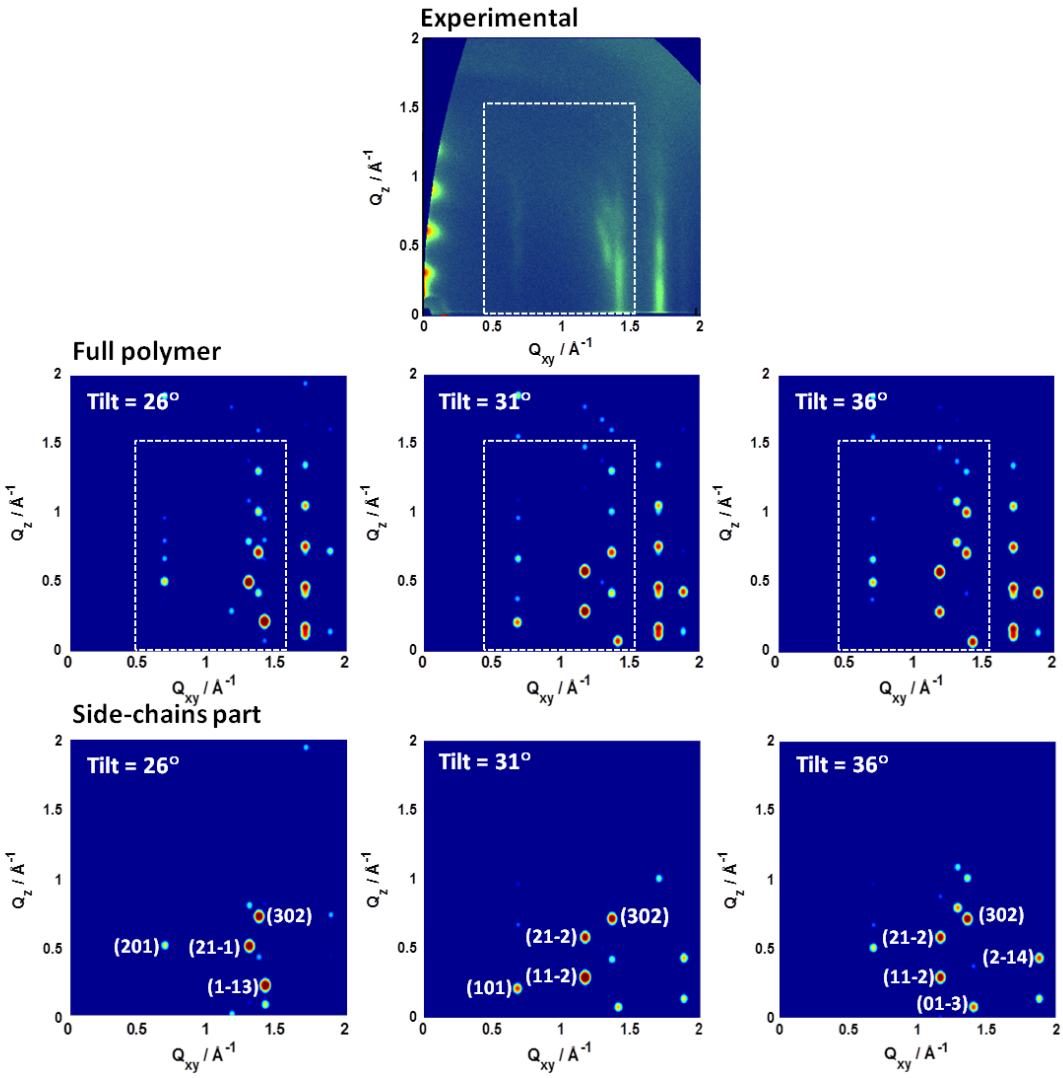


Figure 3.10 Experimental (top) and simulated 2D GIXD patterns of the full polymer (middle) and of only the side chain part (bottom) with various side-chain tilts of: (b) 26°, (c) 31°, and (d) 36° in uniaxial PBTTT-$C_{14}$ films; the white box in the data points to the diffraction pattern coming from the side-chains contributions. Intensities are shown on a logarithmic scale.

### 3.3.3 Influence of alkyl side-chain length on polymer packing

We determined the molecular structures of PBTTT with dodecyl ($C_{12}$) and hexadecyl ($C_{16}$) side chains to evaluate the influence of the side-chain length on the polymer packing properties. The packing motifs of PBTTT determined with various side-chain lengths are

shown in Table 3.4. Regardless of side-chain length, the polymer backbones are planar and tilt slightly with respect to the substrate normal to maintain strong inter-backbone interactions. The interdigitated alkyl side chains are predicted to be straight and present a fully *trans*-conformation (though, as noted above, disorder and gauche defects likely appear in the actual thin films). On increasing the alkyl chain length, the size and shape of the polymer unit cells are modified slightly. With the addition of two methylenes, from $C_{12}$ to $C_{14}$ or $C_{14}$ to $C_{16}$, *a* increases by approximately 2 Å, resulting in increased lamellar d-spacing. The values of β and γ increase slightly by 1° and 3°, respectively. The inter-backbone distance overall remains constant and falls between 3.5-3.6 Å. The backbone tilt angle slightly decreases as the side chain lengthens, which can be regarded as minimal-to-no change as it was shown that differences in backbone tilt produce negligible changes to the GIXD patterns. The tilt of the side chains is also nearly the same with increasing side-chain length.

Table 3.4 Structural parameters of the simulated unit cells for PBTTT-$C_n$, n=12, 14, and 16.

| | | PBTTT-$C_{12}$ | PBTTT-$C_{14}$ | PBTTT-$C_{16}$ |
|---|---|---|---|---|
| Lattice Parameters | *a* (Å) | 19.6 | 21.5 | 23.5 |
| | *b* (Å) | 5.4 | 5.4 | 5.4 |
| | *c* (Å) | 13.5 | 13.5 | 13.5 |
| | α (°) | 137 | 137 | 137 |
| | β (°) | 85 | 86 | 87 |
| | γ (°) | 86 | 89 | 92 |
| Lamellar spacing (Å) | | 19.1 | 21.3 | 23.5 |
| π-stacking distance (Å) | | 3.54 | 3.58 | 3.62 |
| Backbone tilt angle (°) | | 16 | 14 | 10 |
| Side-chain tilt angle (°) | | 25 | 26 | 27 |

We note, however, that there is still a need to improve the models, in particular with regard to disorder. At the molecular level, disorder results from variation of both atomic displacements about their equilibrium positions and molecular/component orientations. These effects have been only marginally taken into account during the simulations presented here. First, the influence of thermal fluctuations is not included in the molecular mechanics simulations as they are performed at 0 K. Additionally, in the process of energy minimization with 3D periodic boundary conditions, it is assumed that all surrounding cells are exact copies of the central unit cell. Recent works[30,31] by Rivnay *et al.* have shown that Warren-Averbach analysis of diffraction line shapes for PBTTT can provide insight into the nature of paracrystalline displacements and variations in the average lattice spacing – variations that are not taken into account in our model. Therefore, any larger-scale disorder is not properly represented. Molecular dynamics simulations of super cells are currently ongoing to investigate further the influence of disorder.

### 3.3.4 Electronic properties as a function of alkyl side-chain length

Efficient charge-carrier transport greatly depends on the polymer packing in the thin film.[32] Our simulations confirm the experimental results that PBTTT-$C_n$ maintains relatively well-ordered crystalline domains with respect to the preferential orientation as the number of carbon atoms in the alkyl side-chains increases from 12 to 16. It is expected that such well-ordered polymer structures can lead to efficient charge-carrier transport. By evaluating the band structure and intermolecular electronic couplings, the

relationship between the three-dimensional structure (taking into account the full alkyl side-chain lengths) and the electronic properties of the polymers can be investigated.

The electronic band structures along the main reciprocal-space directions are displayed in Figure 3.11, with detailed information provided in Table 3.5. Here, the unit cell has one polymer unit, and five valence and conduction bands are displayed. The direct band gap, obtained at the Z point, is ~2.2 eV for each of the polymers in the series, a result consistent with experiment, 2.0 eV.[1] Along the *a*-axis (in the ΓX direction of the Brillouin zone), nearly flat bands are calculated, which means that there is no hole or electron interaction among the polymer chains along the *a*-axis. On the other hand, large dispersions are found along the other directions for both the valence and conduction bands. The strongest dispersions appear along the *c**-axis (in the ΓZ direction of the Brillouin zone), with widths of 0.9 eV for the valence band and 0.6 eV for the conduction band. Along the *b**-axis (in the ΓY direction of the Brillouin zone), large dispersions are also observed, 0.7 eV for the valence band and 0.5 eV for the conduction band. When compared to the earlier work of Northrup,[25] the band dispersions determined here are smaller, a direct result of the backbone slip along the long molecular axis vs. the cofacial backbone orientation considered in the previous study. Our results confirm that the band dispersion is larger along the polymer backbone than along the π-stacking direction, as one might expect *a priori*, and are consistent with previous findings.[25]

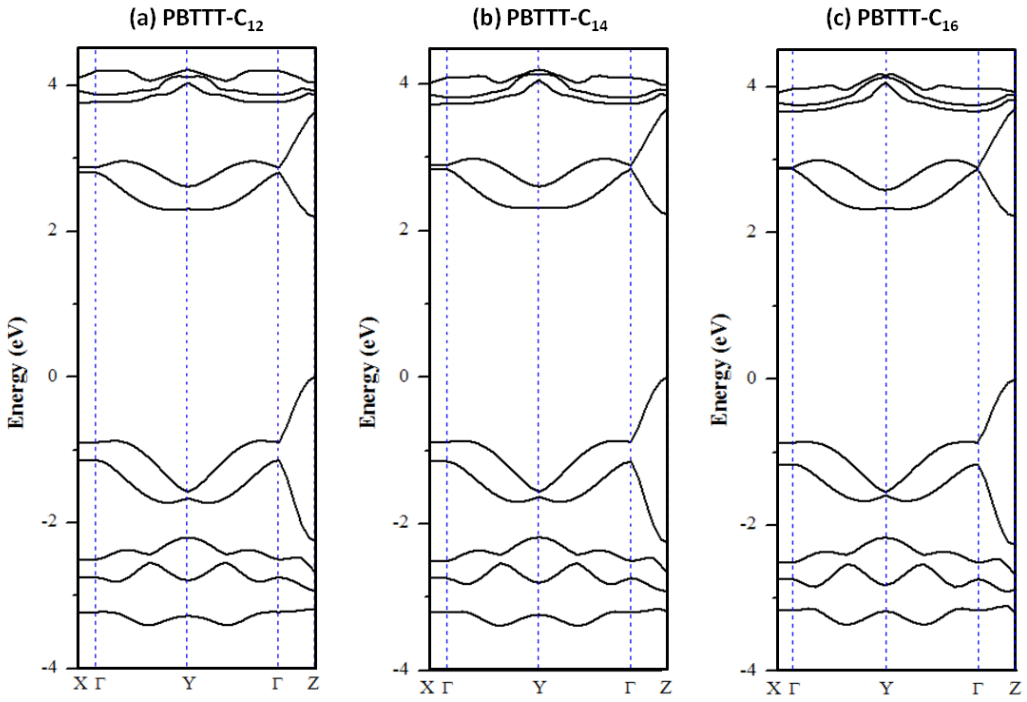


Figure 3.11 Electronic band structures of the PBTTT polymers with $C_{12}$ (a), $C_{14}$ (b), and $C_{16}$ (c) side chains. Points of high symmetry in the first Brillouin zone are labeled as follows: Γ = (0, 0, 0), X = (0.5, 0, 0), Y = (0, 0.5, 0), Z = (0, 0, 0.5), all in crystallographic coordinates. The energy levels are shifted so that the top of the valence band represents the origin of the energy axis.

Table 3.5 Calculated band gaps ($E_g$) at the Z point and dispersions (eV) of the upper valence band (VB) and lower conduction band (CB) along various directions in the Brillouin zone of PBTTT-$C_n$ with n = 12, 14, and 16.

| Dispersion (eV) | X → Γ | | Γ → Y | | Γ → Z | | $E_g$ [eV] |
|---|---|---|---|---|---|---|---|
| | VB | CB | VB | CB | VB | CB | |
| PBTTT-$C_{12}$ | 0 | 0 | 0.68 | 0.50 | 0.89 | 0.61 | 2.20 |
| PBTTT-$C_{14}$ | 0 | 0 | 0.68 | 0.52 | 0.88 | 0.62 | 2.22 |
| PBTTT-$C_{16}$ | 0 | 0 | 0.68 | 0.53 | 0.87 | 0.65 | 2.22 |

Charge transport in spin-coated (disordered) thin films is usually described via a polaron hopping model in which localized charge carriers jump between adjacent chains.[33] In that context, Marcus theory[34,35] has been widely used to assess the charge hopping rate between molecules or polymer chains.[36] According to semiclassical Marcus theory, the electron transfer rate is given by:

$$k_{ij} = \frac{2\pi}{\hbar}\left|t_{ij}\right|^2 \sqrt{\frac{1}{4\pi k_B T \lambda}} \exp\left[-\frac{(\lambda + \Delta G)^2}{4\lambda k_B T}\right] \qquad (3.1)$$

where $t_{ij}$ denotes the transfer integral (electronic coupling) between state *i* and state *j*; λ, the reorganization energy; $\Delta G^0$, the free energy difference between state *i* and state *j*; $k_B$ and *h* are Boltzmann's and Planck's constants, respectively; and T, the temperature. The magnitude of $t_{ij}$ depends on the amount of overlap of the wave functions of the two states. Quantum-chemical calculations can provide direct insight into the extent of the transfer integrals for holes and electrons, $t_h$ and $t_e$.

To further evaluate the electronic interactions in the polymer films, we evaluated the inter-chain electronic couplings between adjacent polymer chains at the B3LYP/6-31G(d,p) level of theory; the main results are collected in Table 3.6. The electronic couplings along the lamellar growth direction (*a*) are expectedly negligible, which is consistent with the lack of dispersion shown by the electronic band-structure calculations. Along the backbone stacking direction (*b*), there is substantial electronic coupling for both holes and electrons, 110-120 meV and 130-145 meV, respectively. These values are significant when compared to the electronic couplings found, for instance, in the pentacene crystal (~ 85 meV) for holes between adjacent molecules along the

herringbone direction.[37,38] The coplanar character of the polymer backbones and the short intermolecular distances should result in large overlap between molecular orbitals on adjacent chains. In the context of a tight-binding model, these electronic-coupling values imply valence and conduction band widths along the *b*-axis on the order of 0.5 eV, which is consistent with the results of the band-structure calculations. The transfer integrals for PBTTT-$C_{12}$ are similar to those determined by Brocorens *et al.*,[15] and smaller than those obtained by Milian-Medina *et al*. for polymers in a cofacial geometry.[39] The variations in band dispersions and transfer integrals when considering cofacial *vs*. slipped polymer-chain packing underline the importance of having precise geometric models for the evaluation of the electronic properties. In any event, the results of the band structure and electronic coupling calculations provide a consistent picture and highlight pronounced electronic couplings for holes and electrons along both the intra-chain and inter-chain directions, which could provide for efficient intra- and inter-chain charge-carrier transport.

Table 3.6 Transfer integrals for holes ($t_h$) and electrons ($t_e$) along the *b*-axis for PBTTT as a function of the side-chain length.

| dimers | *b*-axis | |
|---|---|---|
| | $\lvert t_h \rvert$ (meV) | $\lvert t_e \rvert$ (meV) |
| PBTTT-$C_{12}$ | 113 | 130 |
| PBTTT-$C_{14}$ | 115 | 139 |
| PBTTT-$C_{16}$ | 119 | 145 |

No marked differences in the electronic couplings and band structures are obtained with respect to side-chain length (the electronic couplings and band dispersions increase slightly with longer side chains). This result points to the fact that the side chains are long enough to interdigitate, they facilitate the formation of highly-ordered lamellae and pave the way towards significant intermolecular/intramolecular electronic couplings.

## 3.4 Conclusions

We have used computational modeling to evaluate the three-dimensional orientation of PBTTT-$C_{14}$ films by determining the optimal packing structure and unit-cell parameters based on experimental GIXD patterns for uniaxial and biaxial polymer films. In terms of the polymer packing, planar backbones and relatively short inter-backbone distances are observed, leading to strong inter-chain interactions, as noted previously.[13,15] The straight and interdigitated alkyl side chains contribute to the formation of lamellar structures. Simulations of the diffraction patterns at in-plane angles (0°, 45°, 90°) with respect to the incident beam direction has allowed us to reveal the in-plane (*bc*) ordering of polymers, including substantial lateral slip among the conjugated backbones and considerable side-chain rotation relative to the backbones. This is noteworthy as it is the first time in-plane GIXD simulations for biaxially-oriented polymer structures have been demonstrated, and very reasonable agreement is found between experiment and theory.

We also examined the contributions of the individual polymer components to particular diffraction peaks in the GIXD patterns. The ability to consider these components separately within the unit cell is a powerful technique to understand the diffraction

patterns of uniaxial and biaxial films. From the analysis of the influence of the detailed molecular packing on the GIXD patterns, it is clear that the observable diffraction patterns are more sensitive to the orientation of the alkyl side chains than the relative backbone orientation.

Finally, we thoroughly compared the geometric, packing, and electronic structures for PBTTT polymers with varying side chains, from $C_{12}$ to $C_{16}$. Although slight changes in the lattice parameters are observed with increased side-chain length, the planarity and short inter-chain distance of the backbones remain nearly constant. Quantum-chemical calculations confirm that there is no substantial difference with regard to the electronic properties of polymers as a function of side-chain length. Regardless of the chain length, large electronic couplings are found along the backbone-stacking direction. Strong band dispersions along both the polymer repeat direction and the backbone-stacking direction are calculated, reflecting the potential for efficient inter- and intra-chain charge transport via a two-dimensional channel. This suggests that as long as polymers have long-enough alkyl side chains to contribute to high-structural ordering, efficient intra- and inter-chain charge-carrier transport is possible.

In summary, the combination of computational and experimental techniques exploited in this work has demonstrated an ability to understand the intimate relationship between the structural and electronic properties of polymer films. These tools can foster rational design concepts for new molecular and polymeric materials for organic electronics applications.

## 3.5 References


(1) McCulloch, I.; Heeney, M.; Bailey, C.; Genevicius, K.; Macdonald, I.; Shkunov, M.; Sparrowe, D.; Tierney, S.; Wagner, R.; Zhang, W. M.; Chabinyc, M. L.; Kline, R. J.; McGehee, M. D.; Toney, M. F. *Nat. Mater.* **2006**, *5*, 328.

(2) Chabinyc, M. L.; Toney, M. F.; Kline, R. J.; McCulloch, I.; Heeney, M. *J. Am. Chem. Soc.* **2007**, *129*, 3226.

(3) Wang, S.; Tang, J. C.; Zhao, L. H.; Png, R. Q.; Wong, L. Y.; Chia, P. J.; Chan, H. S. O.; Ho, P. K. H.; Chua, L. L. *Appl. Phys. Lett.* **2008**, *93*, 162103.

(4) Rawcliffe, R.; Shkunov, M.; Heeney, M.; Tierney, S.; McCulloch, I.; Campbell, A. *Chem. Commun.* **2008**, 871.

(5) Jung, Y.; Kline, R. J.; Fischer, D. A.; Lin, E. K.; Heeney, M.; McCulloch, I.; DeLongchamp, D. M. *Adv. Funct. Mater.* **2008**, *18*, 742.

(6) Baklar, M.; Barard, S.; Sparrowe, D.; Wilson, R. M.; McCulloch, I.; Heeney, M.; Kreouzis, T.; Stingelin, N. *Polym. Chem.* **2010**, *1*, 1448.

(7) Lee, M. J.; Gupta, D.; Zhao, N.; Heeney, M.; McCulloch, I.; Sirringhaus, H. *Adv. Funct. Mater.* **2011**, *21*, 932.

(8) Wang, C. C.; Jimison, L. H.; Goris, L.; McCulloch, I.; Heeney, M.; Ziegler, A.; Salleo, A. *Adv. Mater.* **2010**, *22*, 697.

(9) Schuettfort, T.; Watts, B.; Thomsen, L.; Lee, M.; Sirringhaus, H.; McNeill, C. R. *ACS Nano* **2012**, *6*, 1849.

(10) Hamadani, B. H.; Gundlach, D. J.; McCulloch, I.; Heeney, M. *Appl. Phys. Lett.* **2007**, *91*, 243512.

(11) Umeda, T.; Kumaki, D.; Tokito, S. *J. Appl. Phys.* **2009**, *105*, 024516.

(12) Wang, S.; Kiersnowski, A.; Pisula, W.; Mullen, K. *J. Am. Chem. Soc.* **2012**, *134*, 4015.

(13) DeLongchamp, D. M.; Kline, R. J.; Lin, E. K.; Fischer, D. A.; Richter, L. J.; Lucas, L. A.; Heeney, M.; McCulloch, I.; Northrup, J. E. *Adv. Mater.* **2007**, *19*, 833.

(14) Kline, R. J.; DeLongchamp, D. M.; Fischer, D. A.; Lin, E. K.; Richter, L. J.; Chabinyc, M. L.; Toney, M. F.; Heeney, M.; McCulloch, I. *Macromolecules* **2007**, *40*, 7960.

(15) Brocorens, P.; Van Vooren, A.; Chabinyc, M. L.; Toney, M. F.; Shkunov, M.; Heeney, M.; McCulloch, I.; Cornil, J.; Lazzaroni, R. *Adv. Mater.* **2009**, *21*, 1193.

(16) Rappe, A. K.; Casewit, C. J.; Colwell, K. S.; Goddard, W. A.; Skiff, W. M. *J. Am. Chem. Soc.* **1992**, *114*, 10024.

(17) Ewald, P. P. *Ann. Phys.* **1921**, *64*, 253.

(18) Breiby, D. W.; Bunk, O.; Andreasen, J. W.; Lemke, H. T.; Nielsen, M. M. *J. Appl. Crystallogr.* **2008**, *41*, 262.

(19) Breiby, D. W.; Chin, P. T. K.; Andreasen, J. W.; Grimsrud, K. A.; Di, Z. Y.; Janssen, R. A. J. *Langmuir* **2009**, *25*, 10970.

(20) Sun, H.; Ren, P.; Fried, J. R. *Comput. Theor. Polym. Sci.* **1998**, *8*, 229.

(21) Mayo, S. L.; Olafson, B. D.; Goddard, W. A. *J. Phys. Chem.* **1990**, *94*, 8897.

(22) Frisch, M. J.; Trucks, G. W.; Schlegel, H. B.; Scuseria, G. E.; Robb, M. A.; Cheeseman, J. R.; Scalmani, G.; Barone, V.; Mennucci, B.; Petersson, G. A.; Nakatsuji, H.; Caricato, M.; Li, X.; Hratchian, H. P.; Izmaylov, A. F.; Bloino, J.; Zheng, G.; Sonnenberg, J. L.; Hada, M.; Ehara, M.; Toyota, K.; Fukuda, R.; Hasegawa, J.; Ishida, M.; Nakajima, T.; Honda, Y.; Kitao, O.; Nakai, H.; Vreven, T.; Montgomery, J., J. A.; Peralta, J. E.; Ogliaro, F.; Bearpark, M.; Heyd, J. J.; Brothers, E.; Kudin, K. N.; Staroverov, V. N.; Kobayashi, R.; Normand, J.; Raghavachari, K.; Rendell, A.; Burant, J. C.; Iyengar, S. S.; Tomasi, J.; Cossi, M.; Rega, N.; Millam, J. M.; Klene, M.; Knox, J. E.; Cross, J. B.; Bakken, V.; Adamo, C.; Jaramillo, J.; Gomperts, R.; Stratmann, R. E.; Yazyev, O.; Austin, A. J.; Cammi, R.; Pomelli, C.; Ochterski, J. W.; Martin, R. L.; Morokuma, K.; Zakrzewski, V. G.; Voth, G. A.; Salvador, P.; Dannenberg, J. J.; Dapprich, S.; Daniels, A. D.; Farkas, Ö.; Foresman, J. B.; Ortiz, J. V.; Cioslowski, J.; Fox, D. J. In *Gaussian 09, Revision A.02*; Gaussian, Inc.: Wallingford, CT, 2009.

(23) Valeev, E. F.; Coropceanu, V.; da Silva, D. A.; Salman, S.; Bredas, J. L. *J. Am. Chem. Soc.* **2006**, *128*, 9882.

(24) Dovesi, R. S., V. R.; Roetti, C.; Orlando, R.; Zicovich-Wilson, C. M.; Pascale, F.; Civalleri, B.; Doll, K.; Harrison, N. M.; Bush, I. J.; D'Arco, P.; Llunell, M.; University of Torino: Torino: Italy, 2006.

(25) Northrup, J. E. *Phys. Rev. B* **2007**, *76*, 245202.

(26) DeLongchamp, D. M.; Kline, R. J.; Jung, Y.; Lin, E. K.; Fischer, D. A.; Gundlach, D. J.; Cotts, S. K.; Moad, A. J.; Richter, L. J.; Toney, M. F.; Heeney, M.; McCulloch, I. *Macromolecules* **2008**, *41*, 5709.

(27) DeLongchamp, D. M.; Kline, R. J.; Jung, Y.; Germack, D. S.; Lin, E. K.; Moad, A. J.; Richter, L. J.; Toney, M. F.; Heeney, M.; McCulloch, I. *ACS Nano* **2009**, *3*, 780.

(28) Cho, E.; Risko, C.; Kim, D.; Gysel, R.; Miller, N. C.; Breiby, D. W.; McGehee, M. D.; Toney, M. F.; Kline, R. J.; Bredas, J. L. *J. Am. Chem. Soc.* **2012**, *134*, 6177.

(29) Baker, J. L.; Jimison, L. H.; Mannsfeld, S.; Volkman, S.; Yin, S.; Subramanian, V.; Salleo, A.; Alivisatos, A. P.; Toney, M. F. *Langmuir* **2010**, *26*, 9146.

(30) Rivnay, J.; Noriega, R.; Northrup, J. E.; Kline, R. J.; Toney, M. F.; Salleo, A. *Phys. Rev. B* **2011**, *83*, 121306.

(31) Rivnay, J.; Noriega, R.; Kline, R. J.; Salleo, A.; Toney, M. F. *Phys. Rev. B* **2011**, *84*, 045203.

(32) Bredas, J. L.; Calbert, J. P.; da Silva, D. A.; Cornil, J. *Proc. Natl. Acad. Sci. U. S. A.* **2002**, *99*, 5804.

(33) Bredas, J. L.; Beljonne, D.; Coropceanu, V.; Cornil, J. *Chem. Rev.* **2004**, *104*, 4971.

(34) Marcus, R. A. *Rev. Mod. Phys.* **1993**, *65*, 599.

(35) Marcus, R. A.; Sutin, N. *Biochimica Et Biophysica Acta* **1985**, *811*, 265.

(36) Coropceanu, V.; Cornil, J.; da Silva, D. A.; Olivier, Y.; Silbey, R.; Bredas, J. L. *Chem. Rev.* **2007**, *107*, 926.

(37) Endres, R. G.; Fong, C. Y.; Yang, L. H.; Witte, G.; Woll, C. *Comput. Mater. Sci.* **2004**, *29*, 362.

(38) Gruhn, N. E.; da Silva, D. A.; Bill, T. G.; Malagoli, M.; Coropceanu, V.; Kahn, A.; Bredas, J. L. *J. Am. Chem. Soc.* **2002**, *124*, 7918.

(39) Milian Medina, B.; Van Vooren, A.; Brocorens, P.; Gierschner, J.; Shkunov, M.; Heeney, M.; McCulloch, I.; Lazzaroni, R.; Cornil, J. *Chem. Mat.* **2007**, *19*, 4949.

# CHAPTER 4

# MOLECULAR SIMULATION OF POLYMER:FULLERENE INTERCALATION PROCESSES IN BHJ SOLAR CELLS

## 4.1 Introduction

In bulk-heterojunction solar cells, device performance is not only influenced by the intrinsic properties of the individual components, but also by how the individual components assemble and interact at interfaces and in the bulk, as exciton dissociation and charge-carrier transport are highly correlated to the nano-structured morphology of the polymer:fullerene blend.[1-5] Therefore, it is important to understand the complex and detailed molecular organization of the polymer:fullerene blend to better understand the electronic processes. Recently, a blend of poly(2,5-bis (3-tetradecyl thiophene-2-yl) thieno [3,2-b] thiophene) (PBTTT-$C_{14}$) and phenyl-$C_{71}$-butyric acid methyl ester ($PC_{71}BM$) has shown promising performance for bulk-heterojunction solar cells, with a power conversion efficiency of 2.3%.[6] The more intriguing feature of the blend, however, is the proposed intercalation of fullerenes among the side-chains of the conjugated polymers, leading to the formation of a bimolecular crystal (or co-crystal).[7] Such a structure allows us to investigate the molecular packing in the blend films, and further understand the relationship between packing structures and electronic properties in the blend using a combination of experiments and simulations.

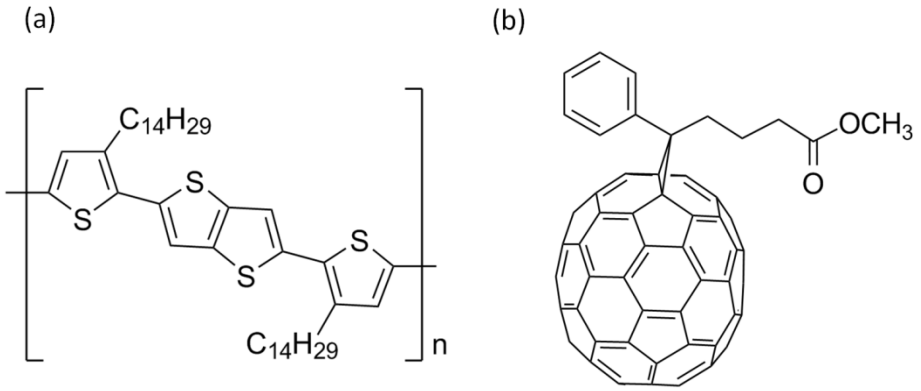


Figure 4.1 Chemical structure of (a) poly (2,5-bis (3–tetradecyl thiophene–2–yl) thieno [3,2-b] thiophene) (PBTTT-$C_{14}$) and (b) phenyl-$C_{71}$-butyric acid methyl ester ($PC_{71}BM$).

Here, we use molecular mechanics (MM) and 2D grazing incidence X-ray diffraction (GIXD) pattern simulations to determine the potential packing configuration for a blend of PBTTT-$C_{14}$:$PC_{71}BM$. We confirm the bimolecular structure, in which $PC_{71}BM$ is intercalated into the polymer side-chains, by comparing the simulated data with experimental 2D GIXD and 2D solid-state nuclear magnetic resonance (NMR) data. The experimental GIXD data were provided by Prof. Michael D. McGehee at Stanford University and Dr. Michael F. Toney at Stanford Synchrotron Radiation Lightsource (SSRL), and the 2D NMR data by the group of Prof. Bradley F. Chmelka at University of California at Santa Barbara. Based on the determined structure, we then performed molecular dynamics (MD) simulations to investigate structural stability and thermal disorder in the co-crystal. In addition, we evaluated the electronic band structure and intermolecular electronic couplings (transfer integrals) using quantum-chemical calculations in order to understand how the packing motifs affect the electronic properties of the blend. Finally, we evaluated the intermolecular interaction energies to reveal the driving force for molecular mixing of the polymer and fullerene.

## 4.2 Computational methodology

Molecular mechanics (MM) and molecular dynamics (MD) simulations were carried out for the unit-cell of PBTTT-$C_{14}$ and $PC_{71}BM$ using the Universal Force Field (UFF)[8] with the Materials Studio software. Initial blends within the crystal unit cell used different ratio of monomer units (e.g., two, three, or four) and two PCBM molecules (Figure 4.2). In addition, the unit-cell parameters were also varied. A number of conformations of the polymer backbones, alkyl side chains, and $PC_{71}BM$ within the unit cell were also considered. Blend crystal packing motifs optimized by UFF were used to simulate the 2D grazing incidence X-ray diffraction (GIXD) patterns using the simDiffraction code.[9,10] An incident X-ray wavelength of 0.975 Å (corresponding to an incident energy of 12.7 keV), a fixed incidence angle of 0.1°, and peak width of 0.01 $Å^{-1}$ were used for the simulations. The $a^*$ direction of the crystal unit cell was set to be oriented parallel to the substrate normal. The degrees of in-plane orientation were set to infinity and 30° for the uniaxially and biaxially textured blend films, respectively, while the degree of out-of-plane orientation was set to 10° for both. The intensity of diffracted peaks was calculated by accounting for the Lorentz factor, in-plane polarization factor, and Debye-Waller factor (u=0.4 Å) as described in the literature.[9]

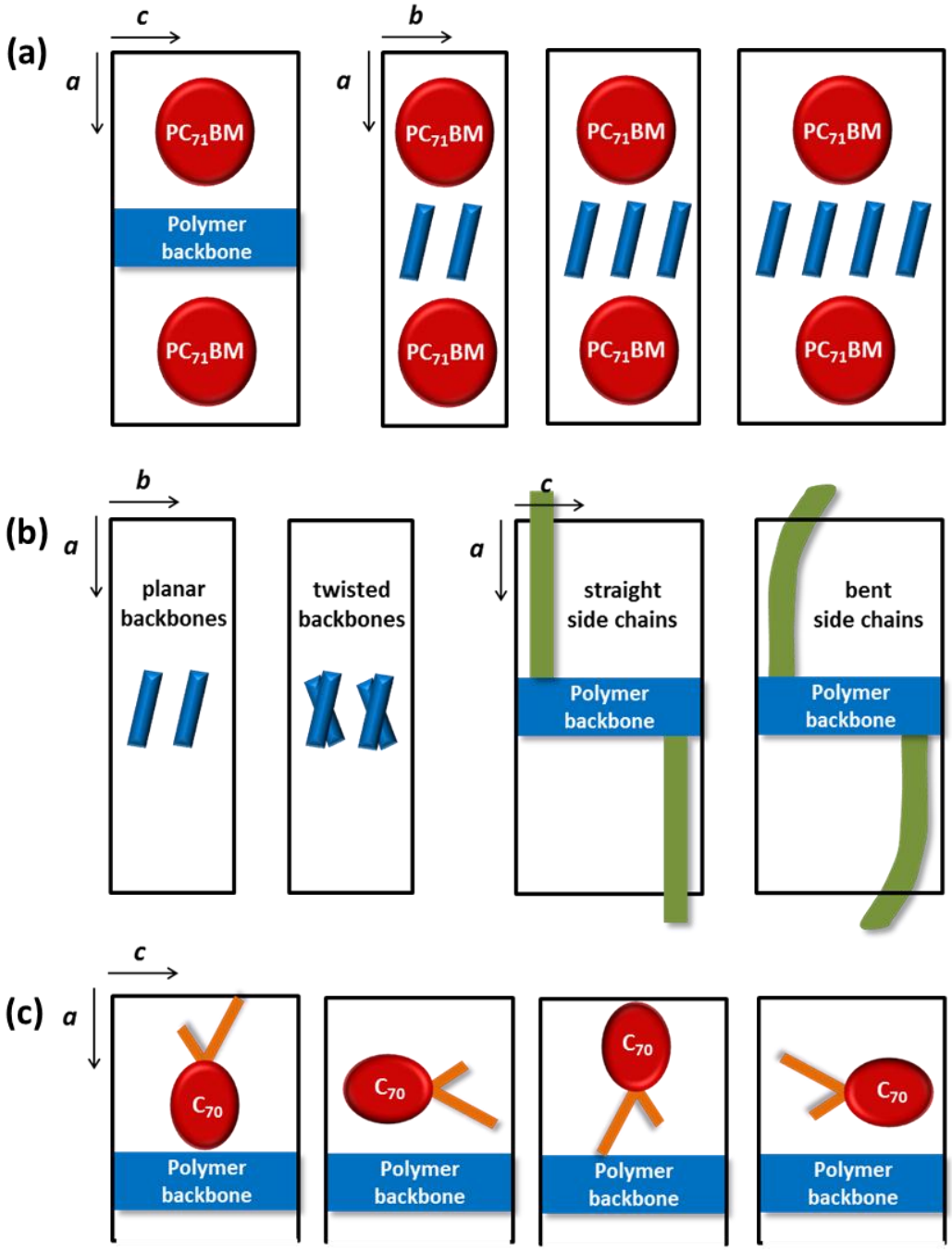


Figure 4.2 Schematic representation of initial structure for PBTTT-$C_{14}$:$PC_{71}BM$ blend we considered: (a) unit cell with various molar ratios of polymer and PCBM viewed along the *b*-axis and *c*-axis (1:1, 1.5:1, 2:1), (b) conformation of polymer backbones in *ab* plane (left) and polymer side chains in ac plane (right), and (c) $PC_{71}BM$ orientation with respect to the polymer backbone in ac plane. Here, the *a*-axis of the unit cell was defined as the lamellar growth direction, the *b*-axis as the backbone-stacking direction, and the *c*-axis as the monomer repeat direction along the polymer chain.

We performed density functional theory (DFT) calculations to evaluate the electronic properties of the blend based on the crystal structure optimized using UFF without further geometry optimization. The transfer integrals between adjacent polymer chains, adjacent $PC_{71}BM$ molecules, and polymer and $PC_{71}BM$ pairs were obtained using B3LYP/6-31G(d,p) in the Gaussian 09 program[11], with a basis set orthogonalization procedure.[12,13] The electronic band structures were determined using the generalized-gradient approximation (GGA) exchange-correlation functional of Perdew, Burke, and Ernzerhof (PBE) and the projector-augmented wave (PAW) method in the VASP program.[14,15] The energy cut-off and total energy convergence for the self-consistent iterations were set to 400 eV and $10^{-6}$ eV, respectively, and the Monkhorst-Pack scheme with a 2×6×4 k-point mesh in the Brillouin zone was applied.

## 4.3 Results and discussion

### 4.3.1 Determination of the molar ratio of the bimolecular crystal

Two possible crystal structures for the blend were assigned based on the experimental GIXD patterns: (i) an orthorhombic lattice with parameters $a$ = 30.0Å, $b$ = 12.8 Å, $c$ = 13.5 Å, $\alpha = \beta = \gamma = 90°$ and (ii) a monoclinic lattice with $a$ = 30.0 Å, $b$ = 9.9 Å, $c$ = 13.5 Å, $\alpha = 72°$, $\beta = \gamma = 90°$.[7] Here, we considered two sets of lattice parameters with different blend ratios to construct the crystal structure of the 1:1 blend. Each unit-cell parameter was slightly refined to better match the experimental diffraction pattern. Two sets of unit-cell parameters for the blend were determined: (i) a cell close to orthorhombic with $a$ = 31.2 Å, $b$ = 13.5 Å, $c$ = 13.5 Å, $\alpha = 89°$, $\beta = 92°$, $\gamma = 85°$, and (ii) a cell close to

monoclinic with $a$ = 31.2 Å, $b$ = 9.8 Å, $c$ = 13.5 Å, $\alpha$ = 72°, $\beta$ = 89°, $\gamma$ = 89°. The structure optimized with each set of parameters is defined as PT35 and PT24, respectively, as shown in Figure 4.3. The lamellar d-spacings of PT35 and PT24 were 31.1 Å and 31.2 Å, respectively, both of which are consistent with the experimental d-spacing, 31.1 Å. PT35 contains three monomer units and two $PC_{71}BM$ molecules in one unit cell to form the bimolecular crystal, which corresponds to the 1:1 weight ratio of the blend. PT24 contains two monomer units and two $PC_{71}BM$ in one unit cell, which corresponds to a 1:1 molar ratio of the blend.

In terms of the molecular packing structures in Figure 4.3, the alkyl side-chains of both structures are slightly bent, and the conjugated backbones are twisted and bent. The twisted backbone orientations result from interactions between the fullerenes and the conjugated backbones; such a twist could affect the hole mobility along the polymer chains versus the pure polymer structure. The $PC_{71}BM$ molecules are oriented along the *b*-axis and the functional group of $PC_{71}BM$ is close to the polymer backbones for PT35, and oriented away from the polymer backbones in PT24; these differing orientations could potentially affect the electron mobility through $PC_{71}BM$. PT35 has a larger *b*-length (by about 3 Å) than PT25 to allow for three monomer units in one unit cell; such a difference increases the distance between the $PC_{71}BM$ molecules.

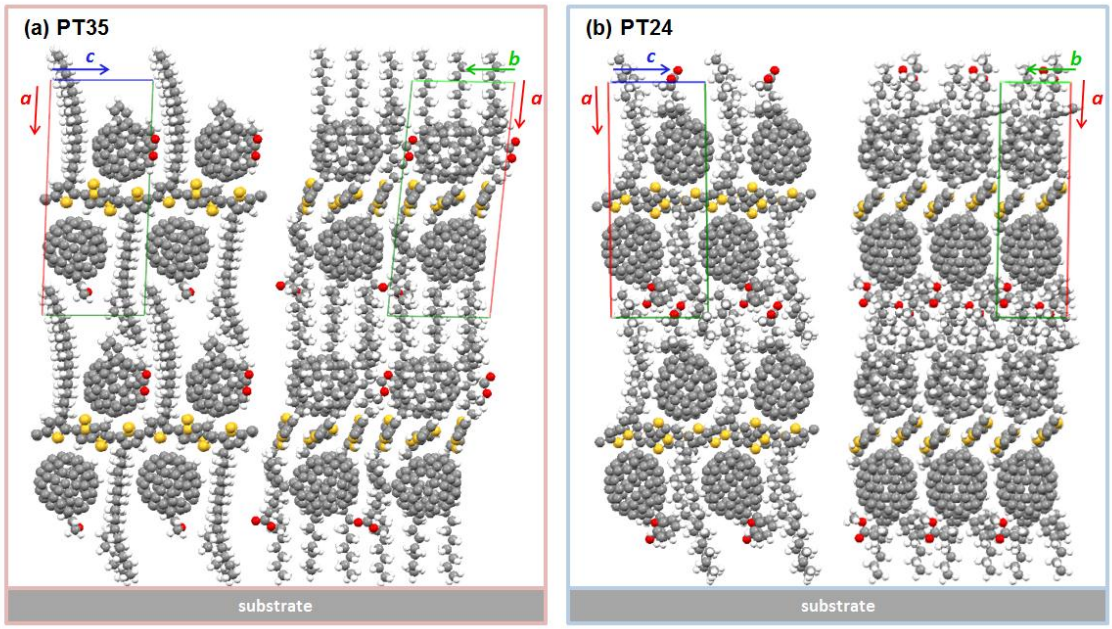


Figure 4.3 Crystal packing of simulated PBTTT-$C_{14}$:$PC_{71}BM$ blend model (a) PT35 and (b) PT24 viewed along the *b*-axis (left) and *c*-axis (right).

To determine the blend ratio and packing motif of the bimolecular structure, 2D GIXD patterns were simulated for both models and compared to experiment. Here, it is assumed that the blend has a preferential out-of-plane orientation and random in-plane orientation. As shown in Figure 4.4, the experimental and simulated GIXD patterns are very similar and show two strong peaks at $Q_{xy}$=0.5 and 1.4 $Å^{-1}$; however, PT35 presents much more intense diffraction peaks than PT24. In the region around $Q_{xy}$=1.0 $Å^{-1}$ where there is no reflection in the experiment, PT35 has several intense peaks along $Q_z$, while PT24 only has weaker peaks at higher $Q_z$. PT35 has much stronger peaks at $Q_{xy}$=0.5 $Å^{-1}$ compared to the experimental data. In terms of intensity comparison, therefore, PT24 seems to match better the experimental data than PT35.

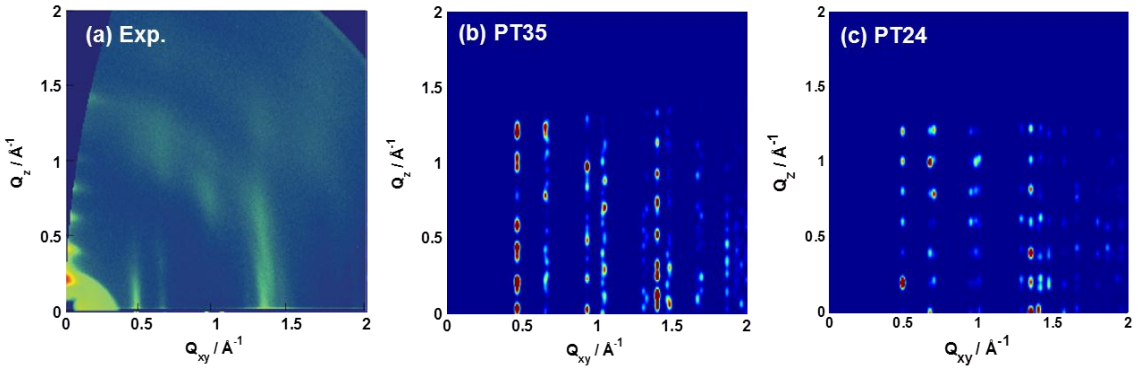


Figure 4.4 Experimental (a) and simulated 2D GIXD patterns of PT35 (b) and PT24 (c), in which blend films have a random in-plane orientation.

The index of the strong peaks at $Q_{xy}$=0.5 and 1.4 $Å^{-1}$ is different for the two simulated models. In the case of PT35, the intense peaks come from *(h10)* and *(h30)*, which correspond to the inter-polymer π-stacking distance along the *b*-axis. For PT24, however, it results from *(h01)* corresponding to the intra-chain distance along the *c*-axis and *(h20)* corresponding to the π-stacking distance, respectively. This allows us to further confirm the best structure based on the experimental 2D GIXD patterns of biaxial blend films at various ϕ angles.[16] The 0° direction means that the chain backbones are oriented along the incoming beam direction, hence *(h10)* peaks associated with backbone stacking are expected to appear in the 0° position. In the experimental data, the peaks at $Q_{xy}$=0.67 and 1.35 $Å^{-1}$ are very intense in the 0° position and become weaker upon increasing angle and disappear at 90°, which indicates that these peaks correspond to the backbone stacking, which is consistent with PT24. Thus, PT24 shows better agreement with the experimental data, although both provide a good match with experiment for textured films with random in-plane orientation. As a result, it is clear that PT24 with a 1:1 molar ratio of PBTTT and $PC_{71}BM$ is the more likely bimolecular structure.

### 4.3.2 Determination of the structure of the bimolecular crystal

We confirmed that the PBTTT:$PC_{71}BM$ bimolecular crystal can form at 1:1 molar ratio of polymer and fullerene. In order to verify the correct lattice parameters for the bimolecular crystal, we compared the PT24 model to PT24 with $\alpha$ = 108°, a result suggested by 2D NMR experiments. Both structures are found to be stable from MM calculations. Figure 4.5 shows the simulated GIXD patterns for both models compared to experiment. These are very similar in terms of intensities and positions of the strongest diffraction peaks.

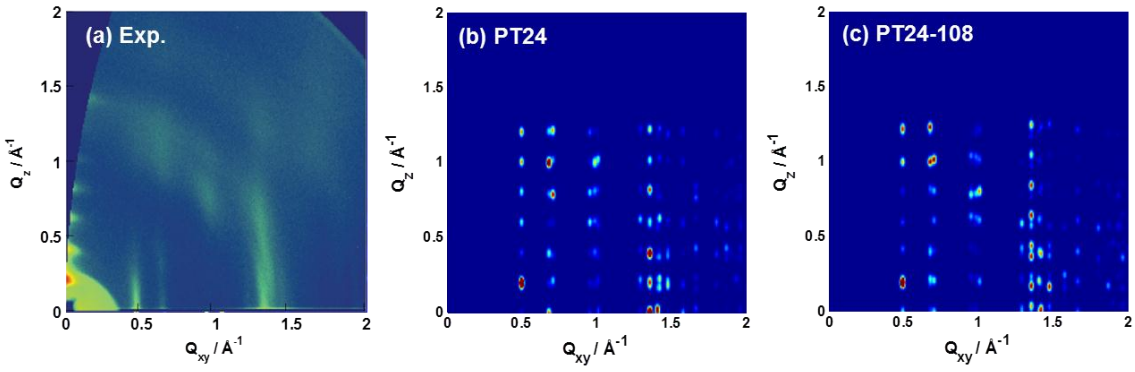


Figure 4.5 Experimental (a) and simulated 2D GIXD patterns of PT24 (b), and PT24-108 (c), in which blend films have a random in-plane orientation.

To further confirm the best unit-cell parameters for the bimolecular crystal, the molecular orientations were compared in detail with the results from 2D solid-state nuclear magnetic resonance (NMR) spectroscopy since NMR spectroscopy is sensitive to local compositional, structural, and dynamical environments in both ordered and disordered regions of the materials.[17] The NMR revealed close molecular proximities between $PC_{71}BM$ and the side-chains and backbones of the polymer, consistent with our model

structures for both.[16] Furthermore, separate solid-state $^{1}H\{^{1}H\}$ double-quantum NMR analyses enabled the local distances between different aromatic proton moieties to be determined (Table 4.1). Specifically, the $^{1}H$ signals at 7.2 and 8.7 ppm correspond to distinct thienothiophene moieties and provide important quantitative constraints that allow the structure of the bimolecular crystal to be confidently established. In terms of the distances between selected aromatic backbone protons, PT24-108 is in good agreement with NMR data while PT24 does not agree as well. Therefore, PT24-108 appears to be the best structure describing the bimolecular crystal and could represent the correct lattice parameters and detailed structural properties in this blend.

Table 4.1 Distance between selected aromatic backbone protons from NMR and two simulated models, PT24 and PT24-108.

| | NMR | PT24 | PT24-108 |
|---|---|---|---|
| $H_{8.7ppm}$ - $H_{8.7ppm}$ distance | 3.6 Å | 5.0 Å | 3.5 Å |
| $H_{7.2ppm}$ - $H_{8.7ppm}$ distance | 3.8 Å | 4.8 Å | 4.3 Å |
| $H_{7.2ppm}$ – $H_{7.2ppm}$ distance | 3.8 Å | 7.1 Å | 4.4 Å |

### 4.3.3 Structural properties

We found that the bimolecular crystal can form at a 1:1 molar blend of PBTTT-$C_{14}$:$PC_{71}BM$ and contains two monomer units and two $PC_{71}BM$ molecules in one unit cell with $\alpha = 108°$ (see Figure 4.6). The conjugated backbones twist and bend while the $PC_{71}BM$ molecules are intercalated within the side-chains of the polymers. This suggests that $PC_{71}BM$ contributes to the disruption of the planar backbone structure, which affects

hole mobility in the polymer along the intra-chain and π-stacking directions. The side-chains are mostly straight, with some bending at their ends. The center-to-center distance for $PC_{71}BM$ along the *b*-axis is around 9.8 Å, with the closest surface distance at 3.0 Å; such a short intermolecular distance could lead to efficient electron transfer in fullerene channels along the *b*-axis.

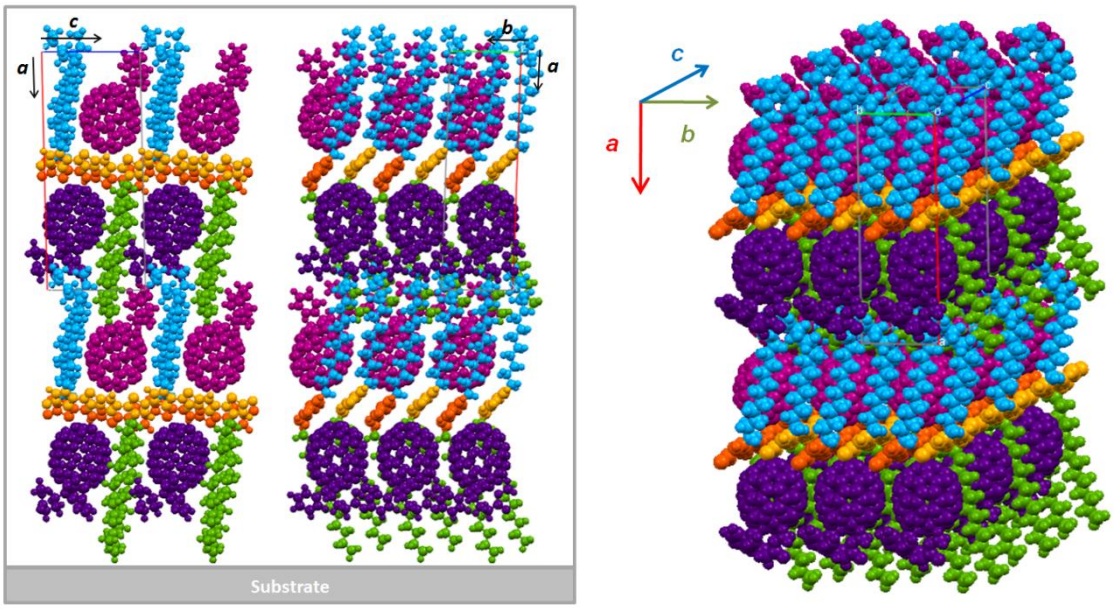


Figure 4.6 Simulated best structure of the PBTTT-$C_{14}$:$PC_{71}BM$ bimolecular crystal, PT-108, viewed along the *b*-axis and *c*-axis, respectively (left), and its three-dimensional packing structure (right).

To study the component contributions of the blend to the GIXD patterns, the blend structure was partitioned into unit cells containing only the: (i) polymer conjugated backbones, (ii) alkyl side chains, and (iii) $PC_{71}BM$ molecules. Then, to further demonstrate the added contributions of two components on the GIXD patterns, the structures were also partitioned into unit cells containing: (iv) polymer backbones and side-chains, (v) polymer backbones and $PC_{71}BM$, and (vi) side chains and $PC_{71}BM$, see

Figure 4.7. Analysis of the single components suggest that the peaks at $Q_{xy}$=0.49 $Å^{-1}$ principally arise from $PC_{71}BM$ and the side chains and those at $Q_{xy}$=0.67 $Å^{-1}$ mainly come from the backbones and $PC_{71}BM$. The peaks with higher $Q_z$ values correspond to the orientation of the $PC_{71}BM$ molecules, except for the $Q_{xy}$=1.35 $Å^{-1}$ region that is associated with the oriented backbone contributions. Analysis of the merged components supports that the peaks around $Q_{xy}$=1.0 $Å^{-1}$ come mainly from $PC_{71}BM$, with some additional intensity from the side chains. These peaks appear stronger than those experimentally measured; however, because the $PC_{71}BM$ and side chains have flexibility at room temperature, these peaks could be expected to be less intense. The diffractions arising in the unit cell containing only the backbones and $PC_{71}BM$ produced an GIXD pattern very similar to the whole system. Thus, we can expect that the peaks at $Q_{xy}$=1.35~1.41 $Å^{-1}$ result from not simply the $PC_{71}BM$ molecules, but interactions between $PC_{71}BM$ and the polymer chains.

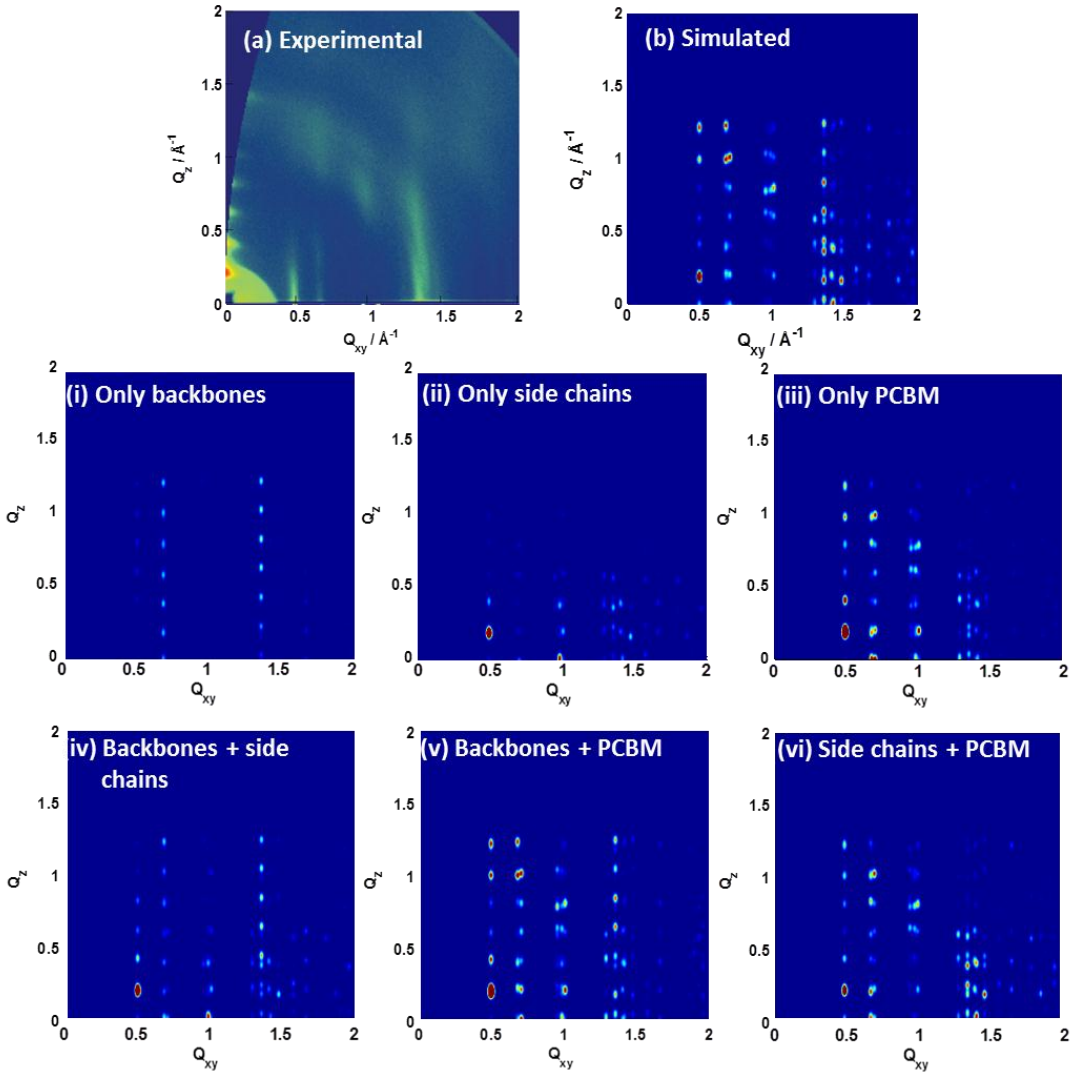


Figure 4.7 Experimental (a) and simulated (b) 2D GIXD patterns of the blend. Simulated 2D GIXD patterns of partitioned structures into unit cells containing (i) polymer backbones, (ii) side chains, (iii) $PC_{71}BM$, (iv) polymer backbones and side chains, (v) polymer backbones and $PC_{71}BM$, and (vi) side chains and $PC_{71}BM$.

### 4.3.4 Thermal stability and disorder

During the determination of the bimolecular crystal structure, only one unit cell was considered in the simulation to focus on the unit-cell parameters and detailed packing motif. In the process of energy minimization with 3D periodic boundary conditions, it is assumed that all surrounding cells are exact copies of the central unit cell, leading to the same orientations for all neighboring molecules. In the real system, however, there could be significant disorder within the structures induced for instance by thermal vibrations. In the MD simulations, the effect of temperature is accounted for by atomistic thermal vibrations.

Hence, we examined the structural stability against thermal fluctuations and morphological disorder in the blend by performing molecular dynamics on a 2×3×2 super cell expanded from the bimolecular crystal unit cell using NPT simulations at room temperature and 1 atm. We found that the energy and density stabilized after 200 ps while the simulations were run for 1 ns, suggesting that the bimolecular crystal structure is quite stable against thermal fluctuations at room temperature. As shown in Figure 4.8, both the MM energy-minimized structure and the one acquired from a snapshot of the super cell obtained towards the end of the MD simulation correlate well with each other in terms of their correspondence with the proton-proton distances determined by the 2D NMR measurements and in their use to simulate the 2D GIXD pattern. The large intensities of (200), (400), and (700) peak in the MM structure decrease in the MD model, which might result from the disorder of the alkyl side-chains and different arrangements of polymer backbones and $PC_{71}BM$ molecules within the super cell.

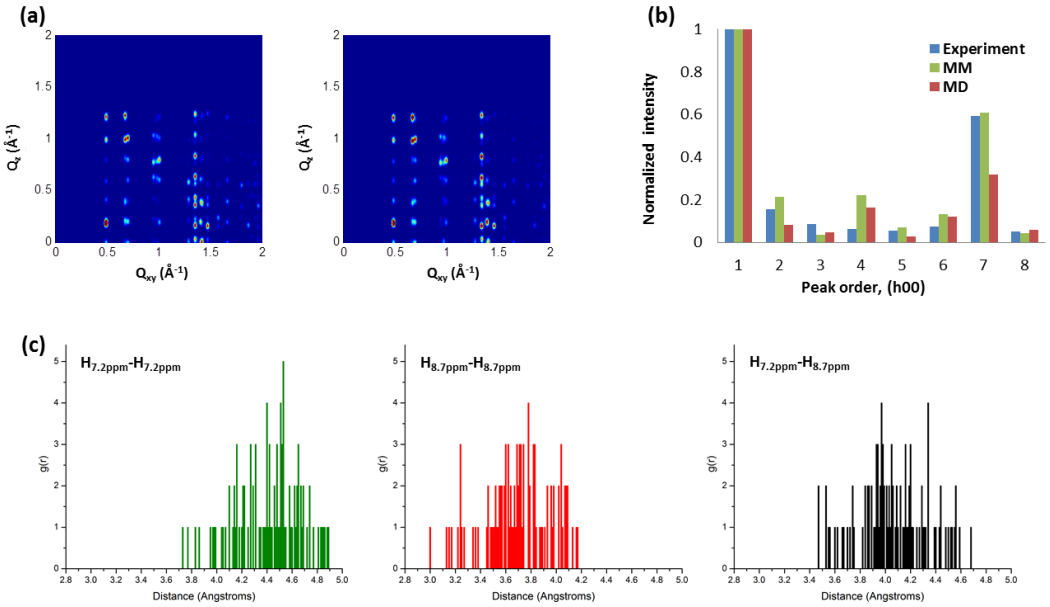


Figure 4.8 (a) Simulated 2D GIXD patterns of the final MM structure (left) and 2×3×2 super cell at 1ns in the MD simulation (right), (b) specular GIXD reflection intensities of MM and MD structures normalized by the (100) peak intensity, and (c) probability densities of H-H distances determined from MD. Note that the software cannot simulate peak broadening and diffuse scattering in the super cell.

### 4.3.5 Electronic properties

The packing structure and morphology of a blend of two different materials have a strong influence on device performance, since the charge-transport properties are dependent on the geometric structures and inter/intra molecular interactions.[18,19] To study the electronic properties of the bimolecular crystal, the electronic band structure along the main reciprocal space directions is investigated as shown in Figure 4.9. Since the unit cell contains two polymer units and two $PC_{71}BM$ molecules, the valence and conduction bands are split into four sub-bands. We find large dispersion for the valence band along *c*-axis (corresponding to the polymer backbone direction), a situation reminiscent of the pristine PBTTT polymer. On the other hand, nearly flat valence and conduction bands are

observed along the *b*-axis, which is a notable difference compared to the pristine polymer.[20] This results from the bent twisted backbones, and increased π-stacking distance upon $PC_{71}BM$ intercalation. Along the *a*-axis, we observed nearly flat bands as well. Thus, we find that there are limited electronic interactions between polymer chains or $PC_{71}BM$ molecules along the *a*- and *b*- axes, while strong interactions exist along the *c*-axis of the polymer.

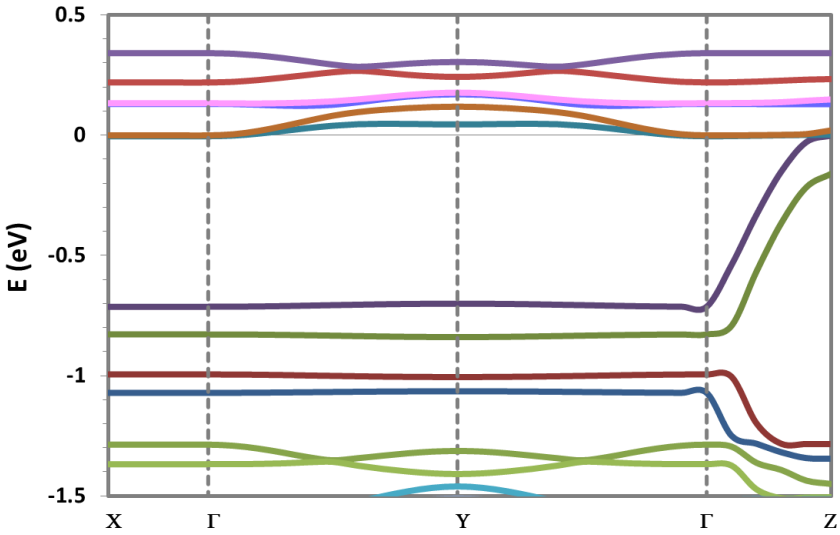


| $E_g$ [eV] | Dispersion (eV) | | | | | |
|---|---|---|---|---|---|---|
| | $X \rightarrow \Gamma$ | | $\Gamma \rightarrow Y$ | | $\Gamma \rightarrow Z$ | |
| | VB | CB | VB | CB | VB | CB |
| 0 | 0 | 0 | 0.01 | 0.05 | 0.71 | 0.01 |

Figure 4.9 Electronic band structures of the PBTTT-$C_{14}$:$PC_{71}BM$ bimolecular crystal, as calculated at the PBE/PAW level. Points of high symmetry in the first Brillouin zone are labeled as follows: Γ = (0, 0, 0), X = (0.5, 0, 0), Y = (0, 0.5, 0), Z = (0, 0, 0.5), all in crystallographic coordinates. The energy levels are shifted so that the top of the valence band represents the origin of the energy axis. Calculated band gaps ($E_g$) at the Z point and dispersions (eV) of the upper valence band (VB) and lower conduction band (CB) along various directions in the Brillouin zone.

The electronic couplings between adjacent polymer chains (P-P), adjacent $PC_{71}BM$ molecules (F-F), and polymer and $PC_{71}BM$ pairs (P-F) calculated at B3LYP/6-31G(d,p) level are listed in Table 4.2. In the case of transfer integrals for electrons among $PC_{71}BM$ molecules, we take into account the first three unoccupied levels, LUMO to LUMO+2,[21] as these molecular orbitals are nearly iso-energetic. Thus, the transfer integrals for the $PC_{71}BM$ molecules presented here represent an average value of these three contributions. Along the *b*-axis, the electronic couplings for holes and electrons dramatically drop (($|t_h|$ = 4 or 82 meV and $|t_e|$ = 42 or 124 meV) compared to the pristine polymers ($|t_h|$ = 115 meV and $|t_e|$ = 139 meV),[20] which is consistent with the results of the band-structure calculations. However, there are relevant electronic couplings (10 ~ 40 meV) between $PC_{71}BM$ molecules. Furthermore, we find non-negligible electronic couplings between the polymer and $PC_{71}BM$ along the *a*-axis at the interface where the polymer backbones 'contact' $PC_{71}BM$. This suggests that electrons and holes can travel from a polymer chain to a $PC_{71}BM$ as well as a neighboring polymer chain at the interface.

Table 4.2 Transfer integrals for holes ($t_h$) and electrons ($t_e$) between adjacent molecules in the bimolecular crystal along the main axes.

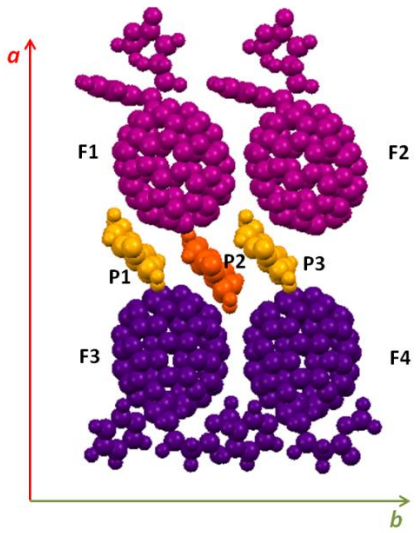


| axis | dimers | $\lvert t_h \rvert$ (meV) | $\lvert t_e \rvert$ (meV) |
|---|---|---|---|
| *a*-axis | P1-F1 | 1 | 15 |
| | P1-F3 | 20 | 29 |
| | P2-F1 | 1 | 20 |
| | P2-F3 | 7 | 11 |
| *b*-axis | P1-P2 | 4 | 42 |
| | P2-P3 | 82 | 124 |
| | F1-F2 | 43 | 6 |
| | F3-F4 | 20 | 37 |

### 4.3.6 Interaction energies

To understand why an intercalated structure can form, we evaluated the miscibility and strength of intermolecular interactions between the polymer chains and the fullerenes in the bimolecular crystal. For comparison, we also studied a hypothetical PBTTT-$C_{14}$:adamantane blend that does not form an intercalated structure for comparison. The

model crystal structures of PBTTT-$C_{14}$ and adamantane were taken from our previous work (Chapter 3)[20] and literature[22], respectively. In the case of $PC_{71}BM$, two possible structures were examined based on the most stable crystalline forms of $PC_{61}BM$[23], as there is no reported crystal structure: a simple cubic structure (sc) and a triclinic structure generated by optimizing the sc structure both without and with unit-cell optimization, respectively. Here, the results for the triclinic unit cell were used because it was found to be the most energetically stable. For the hypothetical blend of PBTTT-$C_{14}$:adamantane, we considered a bimolecular structure analogous to that of the PBTTT-$C_{14}$:$PC_{71}BM$.[16]

First, we performed molecular dynamics (MD) simulations using UFF to determine the cohesive energy densities of the pristine materials. We considered super-cells of the three systems including 4 chains of a PBTTT-$C_{14}$ pentamer and 20 $PC_{71}BM$ molecules, or 96 adamantane molecules. The systems were equilibrated using the NVT ensemble at 300K for 10-30 ps, then followed by an NPT simulation at 300K for 250 ps. The structures over the last 50 ps from the NPT run were collected and averaged to calculate the cohesive energy density of each system. The cohesive energy density represents the energy associated with interactions per unit volume (in atomic simulations, this is defined as the energy required to break all intermolecular physical links in a unit volume of the material).[24-26] The cohesive energy density is widely used to estimate the compatability or degree of molecular mixing of polymer blends since these are closely related to the interaction between two materials. A large cohesive energy density indicates strong intermolecular interactions in the material, and two materials with similar cohesive energy densities should be expected to be compatible on blending. The results show that

PBTTT-$C_{14}$ (636 J/cm$^3$) and $PC_{71}BM$ (644 J/cm$^3$) have very similar cohesive energy densities, while that of adamantane (828 J/cm$^3$) is considerably larger. These cohesive energy densities translate into Hildebrand solubility parameters ($\delta$)[24,27,28] of 12.3 (cal/cm$^3$)$^{1/2}$ for PBTTT-$C_{14}$, 12.4 (cal/cm$^3$)$^{1/2}$ for $PC_{71}BM$, and 14.1 (cal/cm$^3$)$^{1/2}$ for adamantane. The similarity of the calculated values for PBTTT-$C_{14}$ and $PC_{71}BM$ suggests that the two systems should readily mix, while the substantial differences between the polymer and adamantane point to phase separation.

We then evaluated pair-pair interaction energies in the pristine and blend structures to evaluate an important component of the free energy of mixing:

$$\Delta E = 2E_{AB} - E_{AA} - E_{BB} \quad (4.1)$$

where $E_{AB}$ is the total interaction energy between the polymer and small molecule, $E_{AA}$ is the total interaction energy for the neat polymer, and $E_{BB}$ is the total interaction energy for either $PC_{71}BM$ or adamantane. $\Delta E$ is negative for materials that favor mixing/blend formation, while positive $\Delta E$ will indicate that phase separation is favorable.[29,30] The results in Table 4.3 suggest that the bimolecular crystal of PBTTT-$C_{14}$ and $PC_{71}BM$ is energetically favorable while the bimolecular crystal of PBTTT-$C_{14}$ and adamantane is not favorable, which is consistent with the experimental observation.[31]

Table 4.3 Calculated pair-pair interaction energies (energies are in kcal/mol/fragment).

| | System | Pair-pair interaction energy (MM) |
|---|---|---|
| $E_{AA}/E_{BB}$ | PBTTT-$C_{14}$ | -98 |
| | $PC_{71}BM$ | -99 |
| | Adamantane | -26 |
| $E_{AB}$ | PBTTT-$C_{14}$ :$PC_{71}BM$ | -122 |
| | PBTTT-$C_{14}$ :Adamantane | -30 |
| $\Delta E$ | PBTTT-$C_{14}$ :$PC_{71}BM$ | -47 |
| | PBTTT-$C_{14}$ :Adamantane | 64 |

Finally, we assessed the total binding/intermolecular interaction energy within the blends using:

$$E_{binding} = E_{pm} - 2E_p - 2E_m \quad (4.2)$$

where $E_{pm}$ is the unit-cell energy of the intercalated structure (bimolecular crystal) containing the polymer *p* and the molecule *m*, and $E_p$ and $E_m$ represent the energy of the *isolated* components *p* and *m*, respectively. Note that $E_p$ and $E_m$ are multiplied by two as each molecule and polymer appears twice in the intercalated-blend unit cell. In this way, $-E_{binding}$ can be seen as corresponding to the enthalpy of sublimation of the bimolecular crystal. The energies entering Equation (4.2) were evaluated at the molecular mechanics level using the UFF force field and at the density functional-based tight binding (DFTB) level using the DFTB+ software. As shown in Table 4.4, both calculations indicate that the binding energy for the PBTTT-$C_{14}$:$PC_{71}BM$ crystal is much larger than for the (hypothetical) PBTTT-$C_{14}$:adamantane crystal, which means that the PBTTT-

$C_{14}$:$PC_{71}BM$ crystal presents stronger interactions vs. the adamantane blend. The driving force for the intercalation of $PC_{71}BM$ amongst the PBTTT-$C_{14}$ side chains appears to be mainly associated with van der Waals interactions (as opposed to electrostatic interactions).

Table 4.4 Calculated binding energies using molecular mechanics (MM) and the density functional-based tight binding method (energies are in kcal/mol/unit-cell).

| | System | Binding energy (MM) | Binding energy (DFTB) |
|---|---|---|---|
| $E_p/E_m$ | PBTTT-$C_{14}$ | 82 | -65846 |
| | $PC_{71}BM$ | 1332 | -95549 |
| | Adamantane | 14 | -14510 |
| $E_{pm}$ | PBTTT-$C_{14}$ :$PC_{71}BM$ | 2482 | -323207 |
| | PBTTT-$C_{14}$ :Adamantane | -51 | -160976 |
| $E_{binding}$ | PBTTT-$C_{14}$ :$PC_{71}BM$ | -346 | -416 |
| | PBTTT-$C_{14}$ :Adamantane | -244 | -265 |

## 4.4 Conclusions

We have determined the optimal packing motifs and unit-cell parameters for the bimolecular crystal of the PBTTT-$C_{14}$:$PC_{71}BM$ blend based on the experimental 2D GIXD and solid state NMR spectroscopy. Using the UFF-based molecular packing arrangement, the simulated GIXD patterns correspond well with experiment. We confirmed that the bimolecular crystal optimizes at 1:1 molar ratio that contains two monomer units and two $PC_{71}BM$ molecules with a well-ordered lamellar form. We found

that this bimolecular crystal is quite stable against thermal fluctuations at room temperature from MD simulations. In terms of blend packing, the conjugated backbones twisted and bent due to the presence of intercalated $PC_{71}BM$ molecules that are oriented along the backbone stacking direction. There are close contacts between polymer backbones and $PC_{71}BM$ molecules.

Quantum-chemical calculations confirm that structural changes in the blend compared to the pristine polymers leads to a dramatic reduction in the electronic coupling between polymer chains and in the band dispersion along the backbone stacking direction (*b*-axis); strong dispersion for the valence bands along the polymer backbone direction (*c*-axis) maintained, which is consistent with the slightly reduced high hole mobility in the bimolecular crystal. On the other hand, we find substantial electronic coupling between $PC_{71}BM$ molecules along the *b*-axis that can provide a strictly one-dimensional electron-transport channel, which is related to the finding that no electron mobility is observed for blends with a $PC_{71}BM$ loading smaller than 50% (the ratio at which the bimolecular crystal forms).[7,16] Interestingly, there is also non-negligible electronic coupling between the polymer and $PC_{71}BM$ along the lamellar stacking direction (*a*-axis) at the interface.

In terms of molecular mixing using molecular modeling, we find that PBTTT-$C_{14}$ and $PC_{71}BM$ should mix favorably, leading to the formation of the bimolecular crystal. Our results show the strong binding energy between PBTTT and $PC_{71}BM$ arises principally from van der Waals interactions. This work offers an in-depth molecular picture of the relationship between the packing and charge-transport properties in the bimolecular

crystal. Knowing more about how molecules pack in bulk-heterojunctions will be useful to better understand the electronic processes in polymer-fullerene blends could enable the design of more efficient solar cells.

## 4.5 References


(1) Hoppe, H.; Sariciftci, N. S. *J. Mater. Chem.* **2006**, *16*, 45.

(2) Blom, P. W. M.; Mihailetchi, V. D.; Koster, L. J. A.; Markov, D. E. *Adv. Mater.* **2007**, *19*, 1551.

(3) Mayer, A. C.; Scully, S. R.; Hardin, B. E.; Rowell, M. W.; McGehee, M. D. *Mater. Today* **2007**, *10*, 28.

(4) Kippelen, B.; Bredas, J. L. *Energy Environ. Sci.* **2009**, *2*, 251.

(5) Moule, A. J.; Meerholz, K. *Adv. Funct. Mater.* **2009**, *19*, 3028.

(6) Parmer, J. E.; Mayer, A. C.; Hardin, B. E.; Scully, S. R.; McGehee, M. D.; Heeney, M.; McCulloch, I. *Appl. Phys. Lett.* **2008**, *92*, 113309.

(7) Mayer, A. C.; Toney, M. F.; Scully, S. R.; Rivnay, J.; Brabec, C. J.; Scharber, M.; Koppe, M.; Heeney, M.; McCulloch, I.; McGehee, M. D. *Adv. Funct. Mater.* **2009**, *19*, 1173.

(8) Rappe, A. K.; Casewit, C. J.; Colwell, K. S.; Goddard, W. A.; Skiff, W. M. *J. Am. Chem. Soc.* **1992**, *114*, 10024.

(9) Breiby, D. W.; Bunk, O.; Andreasen, J. W.; Lemke, H. T.; Nielsen, M. M. *J. Appl. Crystallogr.* **2008**, *41*, 262.

(10) Breiby, D. W.; Chin, P. T. K.; Andreasen, J. W.; Grimsrud, K. A.; Di, Z. Y.; Janssen, R. A. J. *Langmuir* **2009**, *25*, 10970.

(11) Frisch, M. J.; Trucks, G. W.; Schlegel, H. B.; Scuseria, G. E.; Robb, M. A.; Cheeseman, J. R.; Scalmani, G.; Barone, V.; Mennucci, B.; Petersson, G. A.; Nakatsuji, H.; Caricato, M.; Li, X.; Hratchian, H. P.; Izmaylov, A. F.; Bloino, J.; Zheng, G.; Sonnenberg, J. L.; Hada, M.; Ehara, M.; Toyota, K.; Fukuda, R.; Hasegawa, J.; Ishida, M.; Nakajima, T.; Honda, Y.; Kitao, O.; Nakai, H.; Vreven, T.; Montgomery, J., J. A.; Peralta, J. E.; Ogliaro, F.; Bearpark, M.; Heyd, J. J.; Brothers, E.; Kudin, K. N.; Staroverov, V. N.; Kobayashi, R.; Normand, J.; Raghavachari, K.; Rendell, A.; Burant, J. C.; Iyengar, S. S.; Tomasi, J.; Cossi, M.; Rega, N.; Millam, J. M.; Klene, M.; Knox, J. E.; Cross, J. B.; Bakken, V.; Adamo, C.; Jaramillo, J.; Gomperts, R.; Stratmann, R. E.; Yazyev, O.;

Austin, A. J.; Cammi, R.; Pomelli, C.; Ochterski, J. W.; Martin, R. L.; Morokuma, K.; Zakrzewski, V. G.; Voth, G. A.; Salvador, P.; Dannenberg, J. J.; Dapprich, S.; Daniels, A. D.; Farkas, Ö.; Foresman, J. B.; Ortiz, J. V.; Cioslowski, J.; Fox, D. J. In *Gaussian 09, Revision A.02*; Gaussian, Inc.: Wallingford, CT, 2009.

(12) Valeev, E. F.; Coropceanu, V.; da Silva, D. A.; Salman, S.; Bredas, J. L. *J. Am. Chem. Soc.* **2006**, *128*, 9882.

(13) Kjelstrup-Hansen, J.; Norton, J. E.; da Silva, D. A.; Bredas, J. L.; Rubahn, H. G. *Org. Electron.* **2009**, *10*, 1228.

(14) Kresse, G.; Furthmuller, J. *Comput. Mater. Sci.* **1996**, *6*, 15.

(15) Kresse, G.; Furthmuller, J. *Phys. Rev. B* **1996**, *54*, 11169.

(16) Miller, N. C.; Cho, E.; Junk, M. M. J.; Gysel, R.; Risko, C.; Kim, D.; Sweetnam, S.; Miller, C. E.; Richter, L. J.; Kline, R.; Heeney, M.; McCulloch, I.; Zhao, K.; Graham, K. R.; Amassian, A.; Acevedo-Feliz, D.; Knox, C.; Hansen, M. R.; Dudenko, D.; Chmelka, B. F.; Toney, M. F.; Bredas, J. L.; McGehee, M. D. *Adv. Mater.* **2012**, doi:10.1002/adma.201202293.

(17) Spiess, H. W. *Macromolecules* **2010**, *43*, 5479.

(18) Coropceanu, V.; Andre, J. M.; Malagoli, M.; Bredas, J. L. *Theor. Chem. Acc.* **2003**, *110*, 59.

(19) Coropceanu, V.; Cornil, J.; da Silva, D. A.; Olivier, Y.; Silbey, R.; Bredas, J. L. *Chem. Rev.* **2007**, *107*, 926.

(20) Cho, E.; Risko, C.; Kim, D.; Gysel, R.; Miller, N. C.; Breiby, D. W.; McGehee, M. D.; Toney, M. F.; Kline, R. J.; Bredas, J. L. *J. Am. Chem. Soc.* **2012**, *134*, 6177.

(21) Cheung, D. L.; Troisi, A. *J. Phys. Chem. C* **2010**, *114*, 20479.

(22) Donohue, J.; Goodman, S. H. *Acta Crystallogr* **1967**, *22*, 352.

(23) Napoles-Duarte, J. M.; Reyes-Reyes, M.; Ricardo-Chavez, J. L.; Garibay-Alonso, R.; Lopez-Sandoval, R. *Phys. Rev. B* **2008**, *78*, 285706.

(24) Tiller, A. R.; Gorella, B. *Polymer* **1994**, *35*, 3251.

(25) Abou-Rachid, H.; Lussier, L. S.; Ringuette, S.; Lafleur-Lambert, X.; Jaidann, M.; Brisson, J. *Propellants Explos. Pyrotech.* **2008**, *33*, 301.

(26) Jawalkar, S. S.; Adoor, S. G.; Sairam, M.; Nadagouda, M. N.; Aminabhavi, T. M. *J. Phys. Chem. B* **2005**, *109*, 15611.

(27) Hildebrand, J. H.; Scott, R. L. *The solubility of non-electrolytes*; 2nd ed.; Reinhold: New York, 1936.

(28) Belmares, M.; Blanco, M.; Goddard, W. A.; Ross, R. B.; Caldwell, G.; Chou, S. H.; Pham, J.; Olofson, P. M.; Thomas, C. *J. Comput. Chem.* **2004**, *25*, 1814.

(29) Groves, C.; Kimber, R. G. E.; Walker, A. B. *J. Chem. Phys.* **2010**, *133*.

(30) Israelachvili, J. N. *Intermolecular and surface forces*; 3rd ed.; Academic Press: London, 2011.

(31) Miller, N. C.; Cho, E.; Gysel, R.; Risko, C.; Coropceanu, V.; Miller, C. E.; Sweetnam, S.; Sellinger, A.; Heeney, M.; McCulloch, I.; Bredas, J. L.; Toney, M. F.; McGehee, M. D. *Adv. Energy Mater.* **2012**, doi:10.1002/aenm.201200392.

# CHAPTER 5

# THEORETICAL INVESTIGATION OF THE VIBRATIONAL, REDOX, AND OPTICAL PROPERTIES OF PBTTT AND FULLERENES

## 5.1 Introduction

Vibrational spectroscopies, such as infra-red (IR) and Raman, have been extensively used to characterize the structural properties of molecular systems and determine the degree of charge transfer in organic materials.[1-3] Recently these techniques have been exploited to understand charge transfer and morphological changes in polymer-fullerene blends used in bulk-heterojunction solar cells.[4] Barbour *et al.* studied charge transfer in a blend of poly-(2-methoxy-5-(2'-ethylhexyloxy)-1,4-(1-cyanovinylene)-phenylene) (CN-MEH-PPV) and $PC_{61}BM$ using IR spectroscopy.[5] They found a 5 $cm^{-1}$ up-shift in the frequency of the C=O stretching of $PC_{61}BM$ as $PC_{61}BM$ is closely located at the interface with the polymer chains. Falke *et al.* used Raman spectroscopy to evaluate characteristic features attributable to $PC_{61}BM$ in a blend of P3HT and $PC_{61}BM$.[6] They identified the pentagon pinch mode $A_g(2)$ of singly and doubly negatively charged $C_{60}$ molecules in the blend, which is an evidence of the fullerene inclusions in the blend. With that in mind, a systematic theoretical approach to study the intrinsic vibrational properties of pristine polymers and fullerenes can be valuable so as to provide a description of the vibrational properties related to neutral and charged structures. Moreover, it can provide further understanding of the spectroscopic changes in the polymer:fullerene blend.

In order to elucidate the relationship between the spectroscopic changes and the properties of the polymer:fullerene blend, we have performed a comprehensive theoretical study of the IR and Raman spectra of pristine PBTTT and a series of fullerenes in the neutral and charged states. The experimental Raman data presented here were provided by Prof. Michael D. McGehee at Stanford University. In the case of PBTTT, we evaluated the influence of the oligomer length (from monomer to tetramer) on the vibrational modes, as we cannot perform simulations for a full polymer, as well as the effects of oxidation. We also examined modifications to the vibrational spectrum of a series of fullerenes upon reduction: $C_{60}$ and $C_{70}$, phenyl-$C_{61}$-butyric acid methyl ester ($PC_{61}BM$) and phenyl-$C_{71}$-butyric acid methyl ester ($PC_{71}BM$), bis-$PC_{61}BM$ and bis-$PC_{71}BM$, and the indene adducts,[7] indene-$C_{60}$-monoadduct ($IC_{60}MA$) and indene-$C_{60}$-bisadduct ($IC_{60}BA$), (see Figure 5.1). As a part of this study, we also examined the redox and optical properties of PBTTT and the fullerenes.

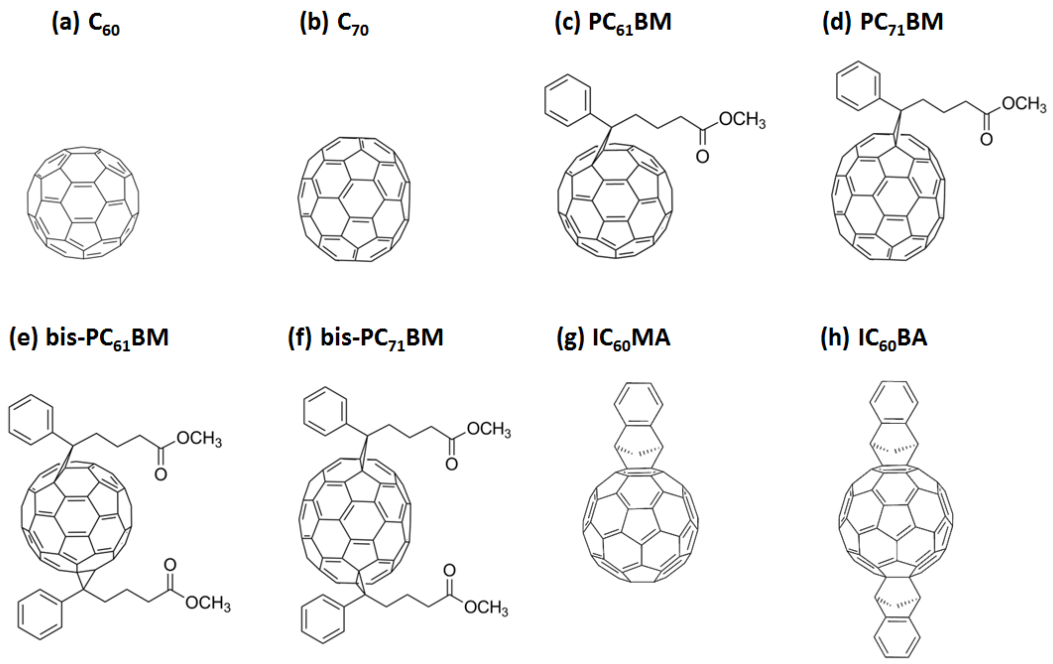


Figure 5.1 Chemical structures of (a) $C_{60}$, (b) $C_{70}$, (c) $PC_{61}BM$, (d) $PC_{71}BM$, (e) bis-$PC_{61}BM$, (f) bis-$PC_{71}BM$, (g) $IC_{60}MA$, and (h) $IC_{60}BA$.

## 5.2 Computational methodology

Density functional theory (DFT) calculations employing the B3LYP functional and a 6-31G(d,p) basis set were carried out with the *Gaussian 09* package[8] to determine the geometric, redox, and vibrational properties of the systems. Geometry optimizations of each molecule in the neutral and radical-ion states were performed, and were followed by frequency analysis to determine the IR and Raman vibrational spectra. Time-dependent DFT (TD-DFT) was used to obtain the optical absorption properties; 40 singlet states and the first three triplet states were considered.

To study these properties in PBTTT, we examined an oligomer series (n = 1 – 4) of the PBTTT backbone with ethyl side groups. This length for the alkyl side groups was

chosen as it was shown to be the smallest length that can reproduce the trends in torsion potential of full tetradecyl alkyl side chains (Figure 5.2).

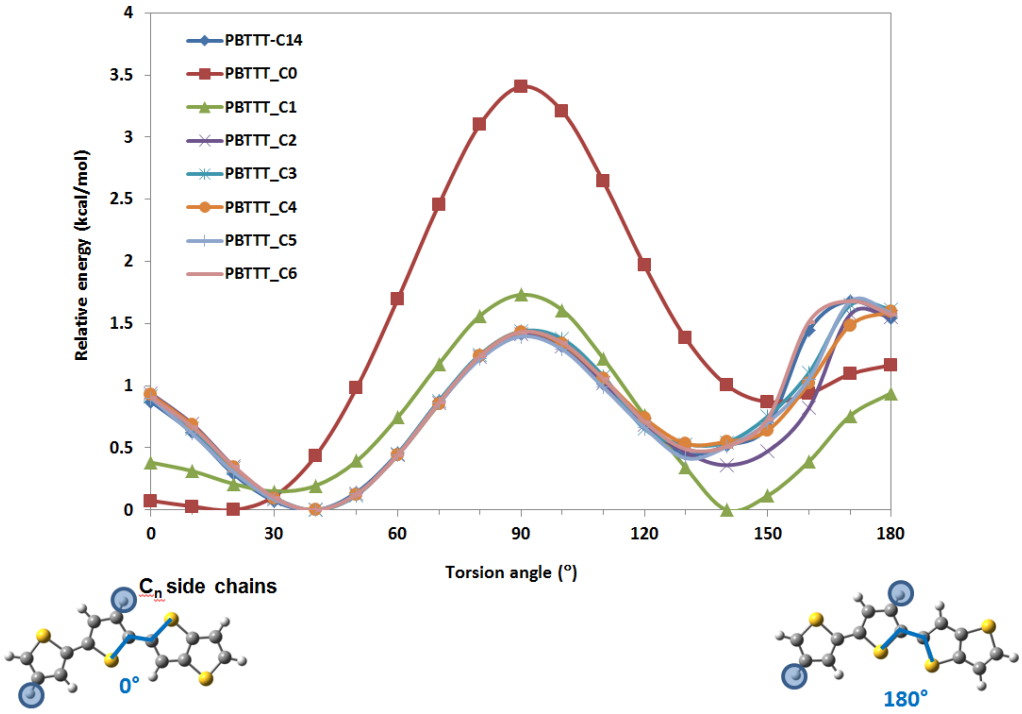


Figure 5.2 Potential surface of torsion between thienothiophenes and thiophene units for PBTTT monomer as a function of side-chain length. Calculations were performed at B3LYP/6-31G(d,p) level. 0° and 180° torsion angles represent anti-conformation and syn-conformation between the units, respectively.

For PBTTT, the monomer unit can be drawn in two distinct forms regarding the order of thiophene (T) and thienothiophene (T2) moieties. Here, the thiophene-thienothiophene-thiophene (T-T2-T) and thiophene-thiophene-thienothiophene (T-T-T2) structures are referred to as monomer A and monomer B (Figure 5.3). All calculated frequencies were uniformly scaled by a factor of 0.97.[9] The calculated Raman activities were plotted using a Gaussian broadening with a full-width at half-maximum (FWHM) of 15 $cm^{-1}$ and

normalized to directly compare with experiment. Note that intensities presented below are solely based on Raman activities, and thus do not take into account the effects of temperature, excitation frequency, and type of light detection in the spectrometer.[10-12]

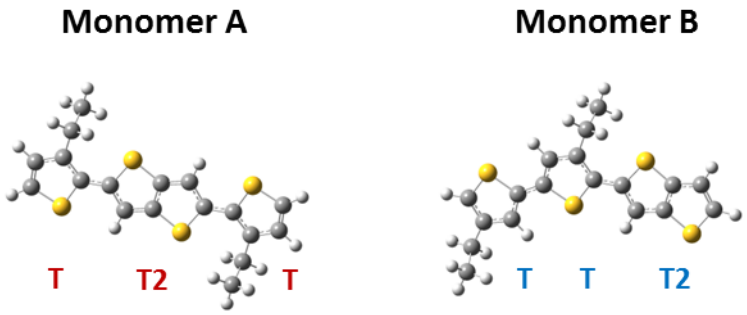


Figure 5.3 Chemical structures of two monomer units of PBTTT, monomer A (left) and monomer B (right).

For the fullerene series, the IR intensity and Raman activity upon reduction were expressed in km/mol and $Å^4$/amu, respectively, the values directly obtained by DFT frequency calculations, without normalization. All calculated frequencies regarding fullerenes presented here were scaled by 0.98 to compare with experimental frequencies, as this scaling factor has been shown by Stratmann *et al.*[13] to provide good agreement for vibrational frequencies of fullerene molecules.

Charge-carrier transport properties can be described as a self-exchange electron transfer process from a charged molecule to a neighboring neutral molecule. The charge-transport properties, thus, are influenced by electron-vibration couplings, which can be estimated from the intramolecular reorganization energy. The intramolecular reorganization energy was determined here by examination of the potential energy surfaces for the neutral (state

1) state and the charged (state 2) state (cation and anion states for polymer and fullerene, respectively) as depicted in Figure 5.4. The reorganization energy (λ) consists of two terms corresponding to the geometry relaxation energies within the respective potential energy surfaces of the neutral and charged state ($\lambda_{rel}^{(1)}$, $\lambda_{rel}^{(2)}$ ):

$$\lambda = \lambda_{rel}^{(1)} + \lambda_{rel}^{(2)} \tag{5.9}$$

$$\lambda_{rel}^{(1)} = E^{(2)}(M) - E^{(1)}(M) \tag{5.10}$$

$$\lambda_{rel}^{(2)} = E^{(2)}(M^-) - E^{(1)}(M^-) \tag{5.11}$$

where $E^{(1)}(M)$ and $E^{(1)}(M^-)$ are the ground-state energies of the neutral and charged states, respectively; $E^{(2)}(M)$ is the energy of the neutral molecule at the optimal charged geometry; $E^{(2)}(M^-)$ is the energy of the charged state at the optimal geometry of neutral molecule.

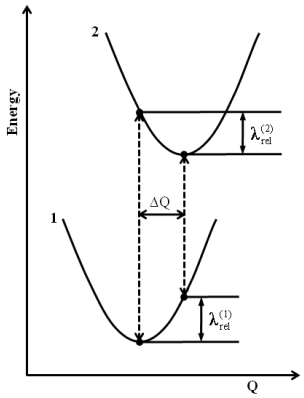


Figure 5.4 Schematic of potential energy surfaces for neutral state 1 and charged state 2, which displays the vertical transitions (dashed lines), normal mode displacement ΔQ, and the relaxation energies $\lambda_{rel}^{(1)}$ and $\lambda_{rel}^{(2)}$.

Another way to determine the intramolecular reorganization energy is through normal mode analysis. The contribution of each vibrational mode to the relaxation energy ($\lambda_{rel}$) can be obtained by expanding the potential energies of the neutral and charged states in a power series of the normal coordinates ($Q_i$). Using the harmonic approximation, the relaxation energy can be expressed as:

$$\lambda_{\mathrm{rel}} = \sum \lambda_i = \sum \hbar\, \omega_i S_i \tag{5.12}$$

$$\lambda_i = \frac{k_i}{2} \Delta \mathrm{Q_i^2}\,, \quad S_i = \frac{\lambda_i}{\hbar \omega_i} \tag{5.13}$$

where the summations run over all vibrational modes; $\Delta \mathrm{Q_i}$ denotes the displacement along normal mode i between the equilibrium positions of the two electronic states of interest; $k_i$ and $\omega_i$ are the force constants and vibrational frequencies; $S_i$ represents the Huang-Rhys factor corresponding to the electron-vibration coupling constant. We used the DUSHIN program[14] of Prof. Jeff Reimers at The University of Sydney to perform the decomposition into the contributions of each normal mode to the total relaxation energy of the molecules and to determine the Duschinsky matrices for the molecules.

## 5.3 Results and discussion

### 5.3.1 Vibrational properties of the pristine polymers

5.3.1.1 Molecular geometries

We can understand the impact of oxidation on the PBTTT geometry by evaluating the modifications to the bond-length alternation of the C-C bonds along the conjugated backbone, described in Figure 5.5. When PBTTT is oxidized, the C-C bonds with single-

bond-like character in the neutral state become shorter while the double C=C bonds elongate, corresponding to a transition from an aromatic type structure to a quinoid structure upon oxidation. As a result, the averaged C-C bond is shorten by 0.01~0.03 Å while the averaged C=C bond elongates by 0.01~0.03 Å upon oxidation, see Table 5.1. These changes in bond length will influence the vibrational modes in the IR and Raman spectra.

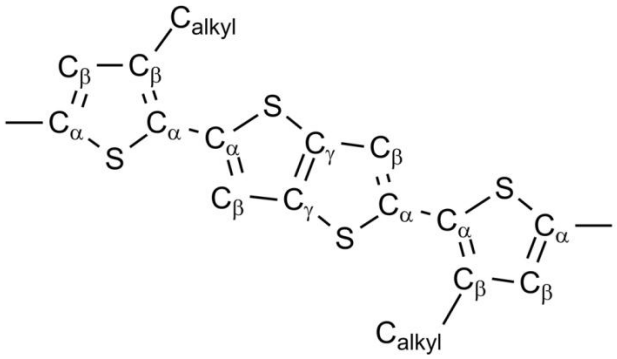


Figure 5.5 Representation of C-C/C=C bond labels and carbon atom type on PBTTT monomer A.

Table 5.1 Averaged bond lengths of PBTTT backbones on oxidation, from monomer to tetramer: these bonds are shown in Figure 5.5.

| Oligomers | Neutral | | Cation | |
|---|---|---|---|---|
| | C-C | C=C | C-C | C=C |
| Monomer | 1.435 | 1.379 | 1.407 | 1.403 |
| Dimer | 1.434 | 1.381 | 1.415 | 1.397 |
| Trimer | 1.433 | 1.382 | 1.419 | 1.374 |
| Tetramer | 1.433 | 1.383 | 1.422 | 1.391 |

5.3.1.2 Raman spectroscopy

We first examine the influence of the oligomer length of the PBTTT monomer A (T-T2-T) on the Raman spectra in the C=C-C ring stretch region.[15,16] Experimentally, four vibrational modes associated with the polymer are observed at 1393, 1418, 1463, and 1493 $cm^{-1}$, referred to as $\nu_1$ to $\nu_4$ in the order of increasing Raman frequency. The DFT evaluation of the Raman modes show good agreement with respect to these four characteristic vibrational modes for C=C-C stretching in the region 1350-1550 $cm^{-1}$ (Figure 5.6). The $\nu_1$ and $\nu_3$ peaks are mainly related to the $C_\beta$-$C_\beta$ stretching and $C_\alpha$-$C_\alpha$ stretching of thiophene rings in the backbone, respectively (see Figure 5.5 for carbon atom labeling). The $\nu_2$ and $\nu_4$ peaks are principally associated with the central $C_\gamma$=$C_\gamma$ stretching and $C_\alpha$=$C_\beta$ stretching of thienothiophene units in the backbone, respectively. The $\nu_1$ mode tends to be localized within the thiophene while the other modes are delocalized. We find that the $\nu_2$ and $\nu_4$ modes shift to lower frequency, while the $\nu_3$ mode shifts to higher frequency, as the oligomer length increases from monomer to tetramer. There is a dramatic decrease in the calculated intensities of the $\nu_2$ and $\nu_4$ vibrations and increase of the $\nu_1$ and $\nu_3$ vibrations on going from monomer to tetramer. The longer the oligomers become, the better the correspondence with experiment in terms of frequency. There are no significant changes in terms of the frequency and intensity when the number of the polymer repeat unit is greater than three, with the frequencies of the trimer and tetramer being the most consistent with experiment. However, there is some difference between computed and experimental intensities.

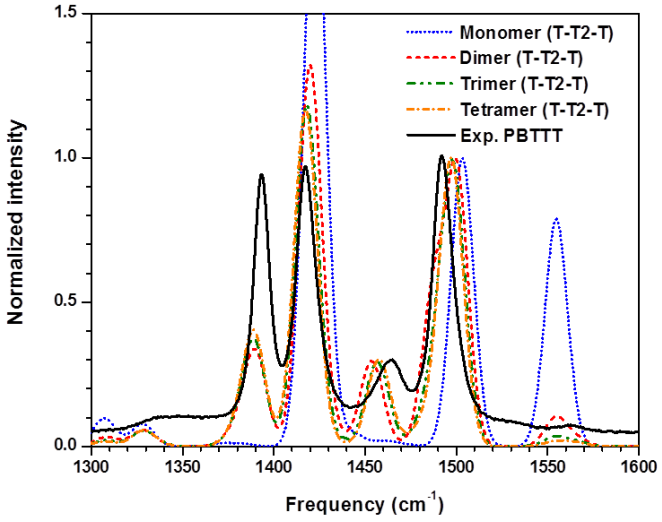


Figure 5.6 Calculated Raman spectra of PBTTT monomer A as a function of oligomer length, from monomer to tetramer, compared to experimental data. Calculations were performed at the B3LYP/6-31G(d,p) level. Intensities are normalized with respect to that of the $\nu_4$ mode.

The effect of the oligomer length on the Raman spectra of PBTTT monomer B (T-T-T2), was also studied (Figure 5.7). As the oligomer length increases, we find a red-shift of the $\nu_2$ and $\nu_4$ vibrational modes. Again, longer chain lengths provide good agreement with experiment. There are no notable changes in both frequency and intensity when the oligomer length is greater than the trimer, which is the same result as for PBTTT monomer A. In general, these results provide confidence that the trimer represents well the characteristics of the polymer.

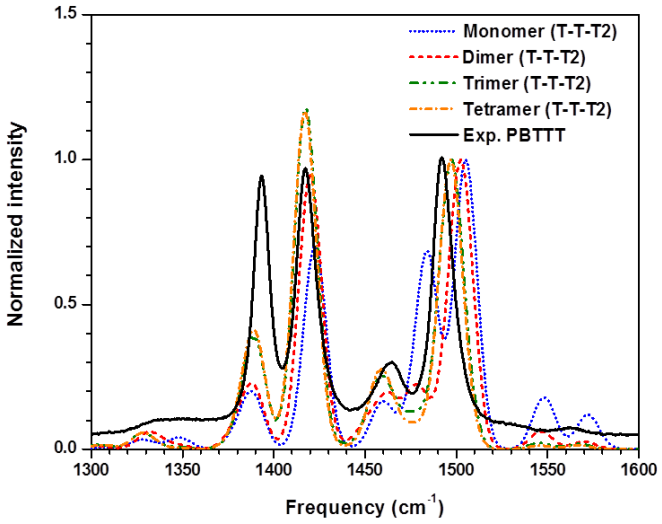


Figure 5.7 Calculated Raman spectra of PBTTT monomer B as a function of oligomer length, from monomer to tetramer, compared to experimental data. Calculations were performed at the B3LYP/6-31G(d,p) level. Intensities are normalized with respect to that of the $\nu_4$ mode.

To reveal the influence of the way of defining the monomer unit on the Raman spectra, PBTTT dimers with monomer A and B were compared (Figure 5.8). The notable differences with respect to the monomer type are the intensity of the $\nu_2$ mode and frequency of the $\nu_3$ mode. These differences result from the twist between thiophene and thiophene units induced by asymmetric end groups on the backbone when the oligomer length is short. Once the number of repeat units is greater than three, however, the influence of the way of defining the repeat unit of the polymer on the vibrational modes is negligible (Figure 5.9), which is consistent with the results with respect to the oligomer length.

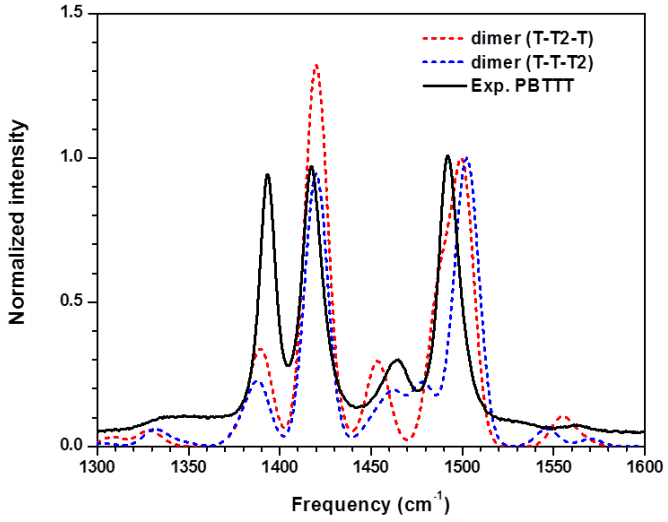


Figure 5.8 Calculated Raman spectra of the PBTTT dimer with two monomer types, compared to experimental data. Calculations were performed at the B3LYP/6-31G(d,p) level. Intensities are normalized with respect to that of the $\nu_4$ mode.

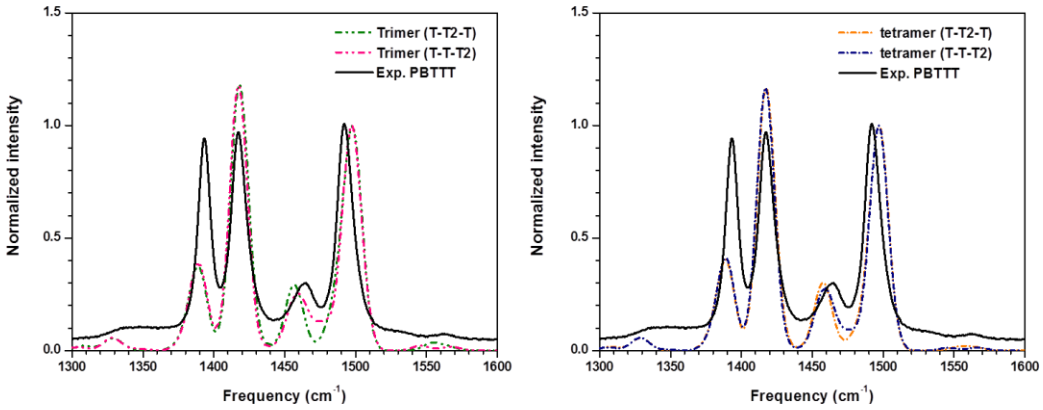


Figure 5.9 Calculated Raman spectra of PBTTT trimer (left) and tetramer (right) with two monomer types, compared to experimental data. Calculations were performed at the B3LYP/6-31G(d,p) level. Intensities are normalized with respect to that of the $\nu_4$ mode.

Our previous results on the structure of PBTTT in thin films suggest that the backbone should be planar.[17] In order to examine the effect of backbone planarity on the vibrational

modes, the Raman spectrum of the trimer based on monomer A with the planar backbone was compared to that of the twisted (optimized) trimer, Figure 5.10. There are notable differences in the intensities of the $\nu_1$ and $\nu_2$ modes. Red-shifts of the $\nu_1$, $\nu_2$, and $\nu_4$ modes are observed. The $\nu_3$ vibrational mode corresponding to $C_\alpha$-$C_\alpha$ stretching between thiophene rings is only minimally affected as the optimized (twisted) geometry has a nearly planar configuration between the thiophenes.

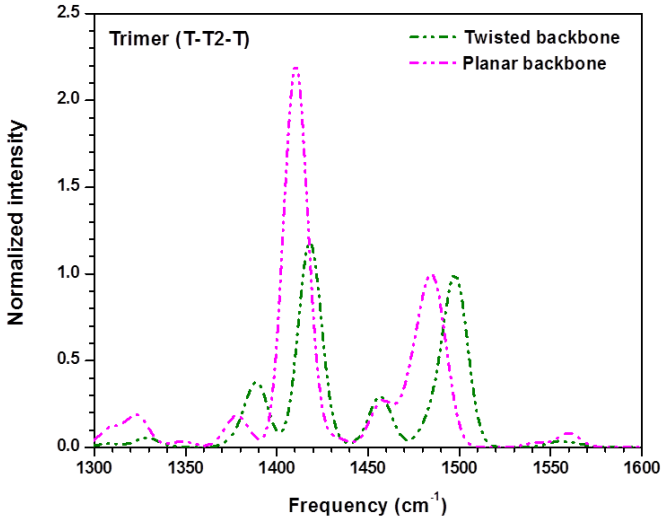


Figure 5.10 Calculated Raman spectra of PBTTT trimer based on monomer A with respect to backbone planarity. Calculations were performed at the B3LYP/6-31G(d,p) level. Intensities are normalized with respect to that of the $\nu_4$ mode.

Since the vibrational properties are sensitive to the electronic and structural changes in the environment, certain vibrational modes might shift upon reduction and oxidation. Thus, we examined the vibrational spectrum of the polymer in the cation state (as PBTTT and like polymers are primarily used as electron-donor materials in organic solar cells). Figure 5.11 shows the effect of oxidation on the Raman spectrum of the PBTTT trimer

based on monomer A. Oxidation causes a shortening of C-C bonds and lengthening of the C=C bonds in the polymer backbone, which leads to a more quinoidal structure of the backbone. As a result, we observe a large downshift of 15 $cm^{-1}$ for $\nu_1$ vibrational modes corresponding to $C_\beta$-$C_\beta$ stretching of thiophene rings. Thus, this vibration can be used to analyze the oxidized state of the PBTTT polymer in the Raman spectrum. There are also notable increases in intensities of the $\nu_1$, $\nu_2$, and $\nu_3$ vibrational modes upon oxidation.

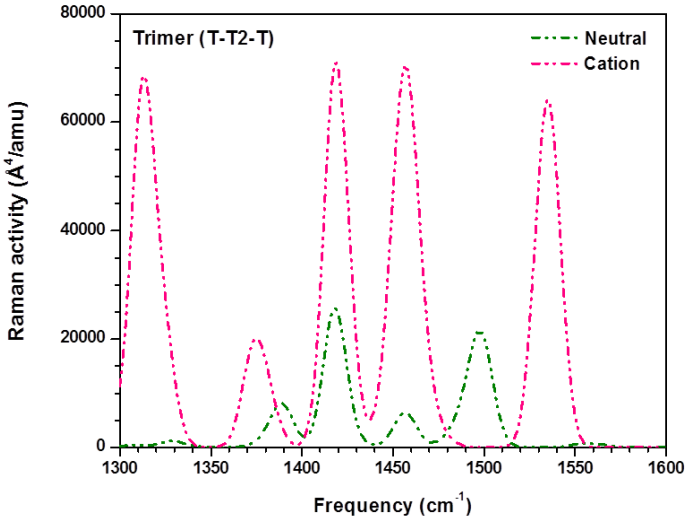


Figure 5.11 Calculated Raman spectra of PBTTT trimer based on monomer A with respect to the charge state, where Raman activities are plotted against frequency. Calculations were performed at the B3LYP/6-31G(d,p) level.

5.3.1.3 Infra-red (IR) spectroscopy

We also examined the IR spectra of the PBTTT trimer based on monomer A on going from the neutral to cation state. As shown in Figure 5.12 and Table 5.2, oxidation activates the vibrations at 1000-1500 $cm^{-1}$ corresponding to conjugated polymer backbone vibrations, which confirms that the hole resides on the backbone rather than

side chains. Upon oxidation, we observe notable downshifts of 6 and 13 $cm^{-1}$ for the aromatic C-H out of plane deformation at 820 $cm^{-1}$ and the symmetric C=C stretching around 1450-1550 $cm^{-1}$ to with increased intensity, respectively. Therefore, these vibrations can be used to analyze the oxidized state of the PBTTT polymer in the IR spectrum.

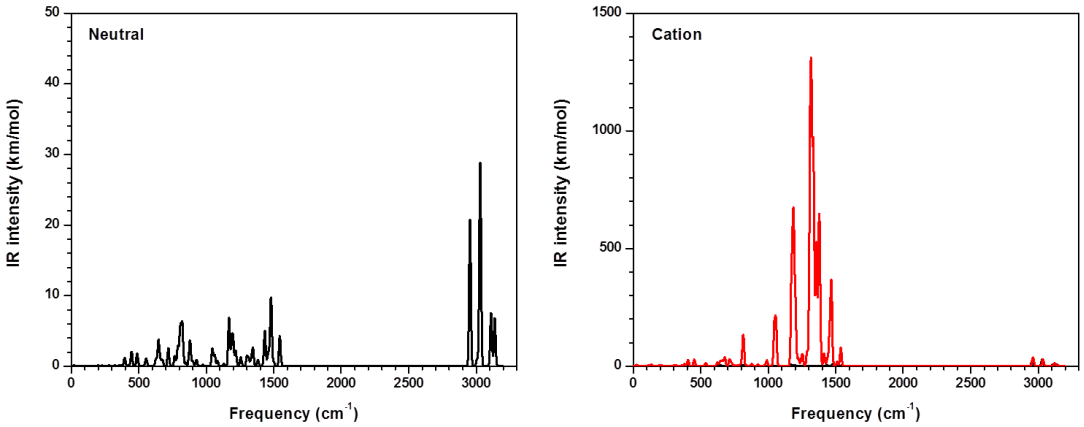


Figure 5.12 Calculated IR spectra of PBTTT trimer based on monomer A with respect to the charge state, as calculated at the B3LYP/6-31G(d,p) level.

Table 5.2 Lists of changes in intensity and frequency of characteristic peaks of PBTTT trimer molecule in the different charged state: IR intensities and frequencies are in km/mol and $cm^{-1}$, respectively; $\nu_C$-$\nu_N$ represents frequency difference between the cation (C) and neutral (N) states; $I_C/I_N$, the ratio of intensity (I) of the cation (C) to the neutral (N).

| Mode | Neutral | | Cation | | Comparison | |
|---|---|---|---|---|---|---|
| | Frequency | IR intensity | Frequency | IR intensity | $\nu_C$-$\nu_N$ | $I_C/I_N$ |
| aromatic C-H out-of-plane deformation | 820.6 | 6.39 | 814.8 | 134.38 | -5.8 | 21.03 |
| symmetric C=C stretching | 1479.3 | 9.76 | 1466.6 | 366.79 | -12.7 | 37.58 |
| anti-symmetric C=C stretching | 1544.24 | 4.28 | 1510.29 | 19.5 | -34.0 | 4.56 |

### 5.3.2 Vibrational properties of fullerenes and their derivatives

5.3.2.1 Molecular geometries

The highly symmetric $C_{60}$ molecule ($I_h$ point group)[18,19] has only two types of bonds: a double-like bond ($d_1$) connecting two hexagonal rings, and a single-like bond ($d_2$) connecting one pentagonal and one hexagonal ring (see Figure 5.13 for bond description). The bond lengths of optimized neutral $C_{60}$ are 1.396 Å for the double bond and 1.453 Å for the single bond. Upon addition of one electron to the three-fold degenerate LUMO, the $C_{60}$ molecule, as a result of a Jahn-Teller effect, is subject to geometrical distortion and a lowering of the symmetry.[20] The length of single or double bonds should no longer be the same and show deviations from the original bond length of the neutral $C_{60}$. In Table 5.3, for instance, the C=C bond ($d_1$) in is elongated by 0.012 Å and the C-C bond ($d_2$) shortens by 0.011 Å. The $C_{70}$ molecule has $D_{5h}$ symmetry and eight inequivalent bonds, shown in Figure 5.13.[19,21] Upon reduction, these bonds are also changed as shown in Table 5.3. In the five-membered rings, $d_1$ is elongated by 0.004 Å, while $d_3$ and $d_5$ are shortened by 0.008 and 0.014 Å, respectively. The $d_2$ and $d_4$, bonds connecting two five-membered rings, are elongated by 0.010 and 0.014 Å, respectively, from neutral to anion state. The $d_6$, $d_7$, and $d_8$ bonds are elongated by 0.020, 0.001, and 0.001 Å, respectively. These trends are in line with previous calculations for $C_{60}$ and $C_{70}$.[22,23] As we discuss below, these changes in the bond lengths influence the vibrational modes and their IR and Raman activities. Similar bond-length changes on reduction are also noted in the PCBM, bis-PCBM, and indene adductions of $C_{60}$ and $C_{70}$, though the lack of symmetry makes the discussion of these changes more complicated.

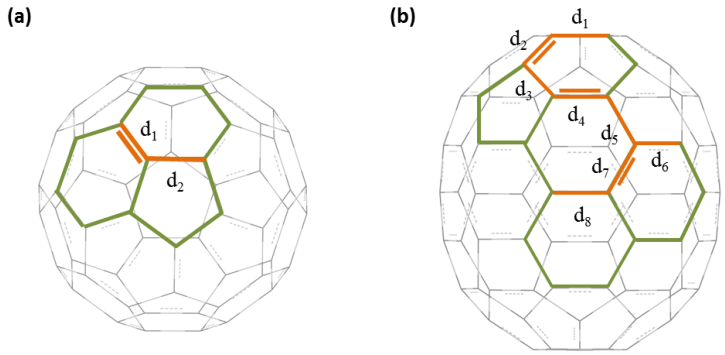


Figure 5.13 Representation of bonds in (a) $C_{60}$ and (b) $C_{70}$: all inequivalent bonds in the fullerenes are labeled and represented in orange.

Table 5.3 Lists of bond lengths of $C_{60}$ and $C_{70}$ as a function of charge state: bond labels are shown in Figure 5.13.

| Molecules | bonds | Distance (Å) | |
|---|---|---|---|
| | | Neutral | Anion |
| $C_{60}$ | $d_1$ | 1.396 | 1.408 |
| | $d_2$ | 1.453 | 1.442 |
| $C_{70}$ | $d_1$ | 1.452 | 1.456 |
| | $d_2$ | 1.397 | 1.407 |
| | $d_3$ | 1.448 | 1.440 |
| | $d_4$ | 1.388 | 1.402 |
| | $d_5$ | 1.449 | 1.435 |
| | $d_6$ | 1.434 | 1.454 |
| | $d_7$ | 1.421 | 1.422 |
| | $d_8$ | 1.471 | 1.472 |

Interestingly, we find two possible conformations for both $PC_{61}BM$ and $PC_{71}BM$ with respect to the orientation of the butyric acid methyl ester group appended to the fullerenes as shown in Figure 5.14. The orientations of the side groups on the PCBMs are labeled A and B, respectively: the A conformation has the $-CH_2CH_2-$ group and $-CH_2COOCH_3$

group of the functional group in the same plane, while the B conformation has those groups lying in different planes. The A conformation is more stable than B conformation by 0.04 eV (1.03 kcal/mol) and 0.05 eV (1.07 kcal/mol) for $PC_{61}BM$ and $PC_{71}BM$. In the case of bis-$PC_{61}BM$ and bis-$PC_{71}BM$, there could be several conformations with respect to the orientation of the functional group although we have not considered them in this study. We note that the two functional groups in bis-$PC_{61}BM$ and bis-$PC_{71}BM$ were considered to be the A conformations and B conformations, respectively.

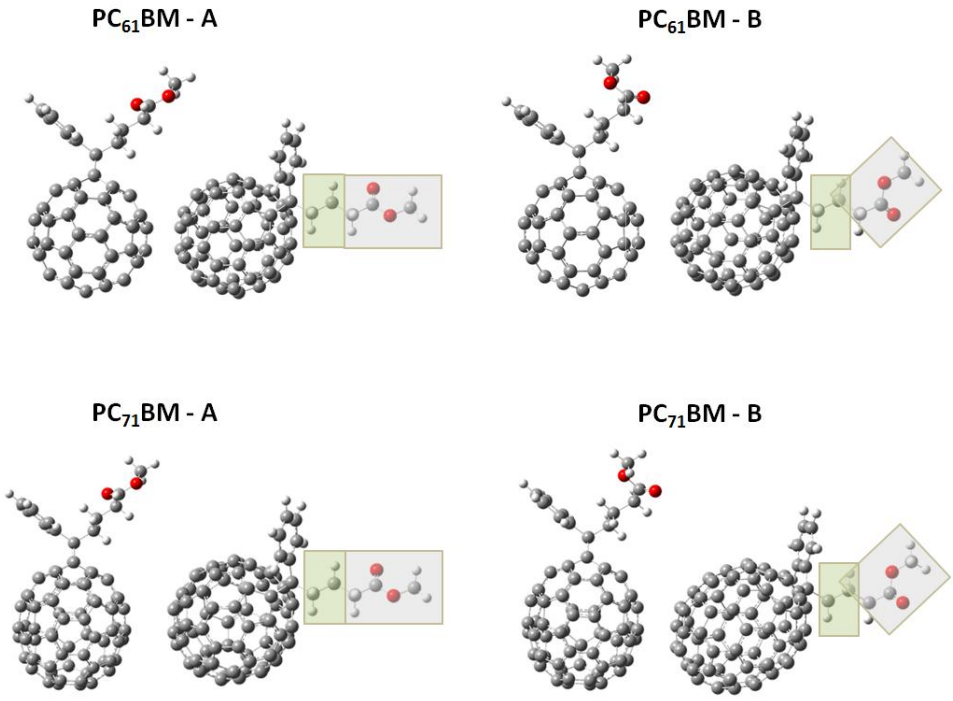


Figure 5.14 Representation of two orientations of side groups (A and B) attached on $PC_{61}BM$ (top) and $PC_{71}BM$ (bottom) from different side views; $-CH_2CH_2CH_2-$ group and $-COOCH_3$ group are located in the green plane and grey plane, respectively.

5.3.2.2 Raman spectroscopy

The highly symmetric $C_{60}$ molecule has two $A_g$ (fully symmetric) and eight $H_g$ (fivefold-degenerate) symmetry modes that are Raman active.[24,25] As shown in Figure 5.15 and Table 5.4, the strongest Raman activity of neutral $C_{60}$ comes mainly from the $A_g(2)$ mode at 1472 $cm^{-1}$, the totally-symmetric pentagon pinch mode corresponding to the symmetric stretching of C=C bonds on the $C_{60}$ cage.[26,27] Upon reduction, the most important change in Raman spectrum of $C_{60}$ is a 6 $cm^{-1}$ downshift of the pentagon pinch mode from 1472 to 1466 $cm^{-1}$, with slightly reduced intensity, in good agreement with several experimental data that show down-shifts of 6 $cm^{-1}$ upon reduction.[28-30] This effect is also observed in the Raman spectra of negatively charged $PC_{61}BM$-A and -B, bis-$PC_{61}BM$ and indene derivatives, which shows a downshift of 6 $cm^{-1}$ of the $A_g(2)$-like mode and a weaker intensity relative to the neutral molecule. Thus, we can infer that this vibrational mode is associated with the reduction of the $C_{60}$ cage. Note that there is no significant difference in Raman spectra between $PC_{61}BM$-A and –B upon reduction.

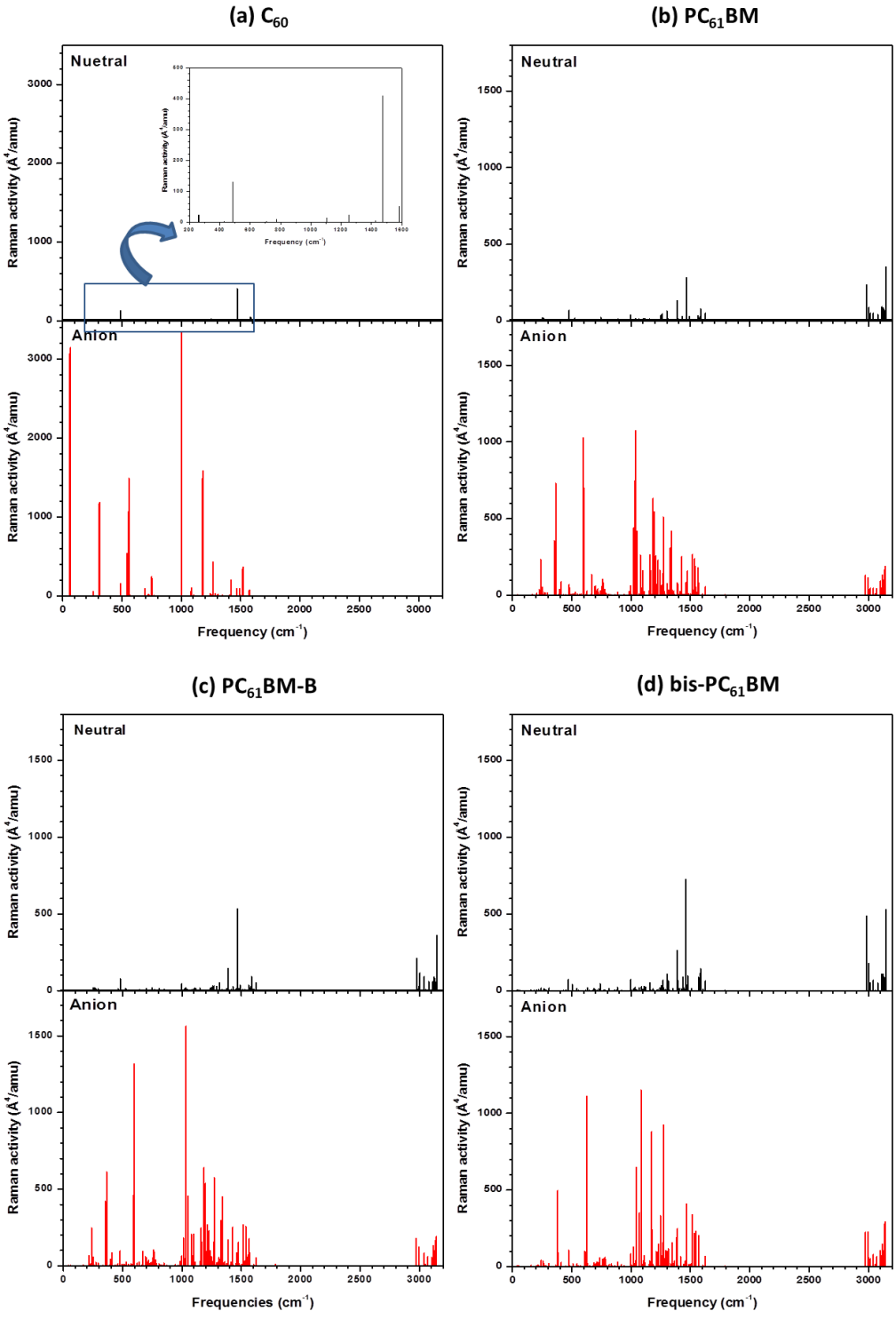
(a) C60
Nuetral
Anion
Raman activity (A4/amu)
Frequency (cm-1)
(b) PC61BM
Neutral
Anion
Raman activity (A4/amu)
Frequency (cm-1)
(c) PC61BM-B
Neutral
Anion
Raman activity (A4/amu)
Frequencies (cm-1)
(d) bis-PC61BM
Neutral
Anion
Raman activity (A4/amu)
Frequency (cm-1)

\

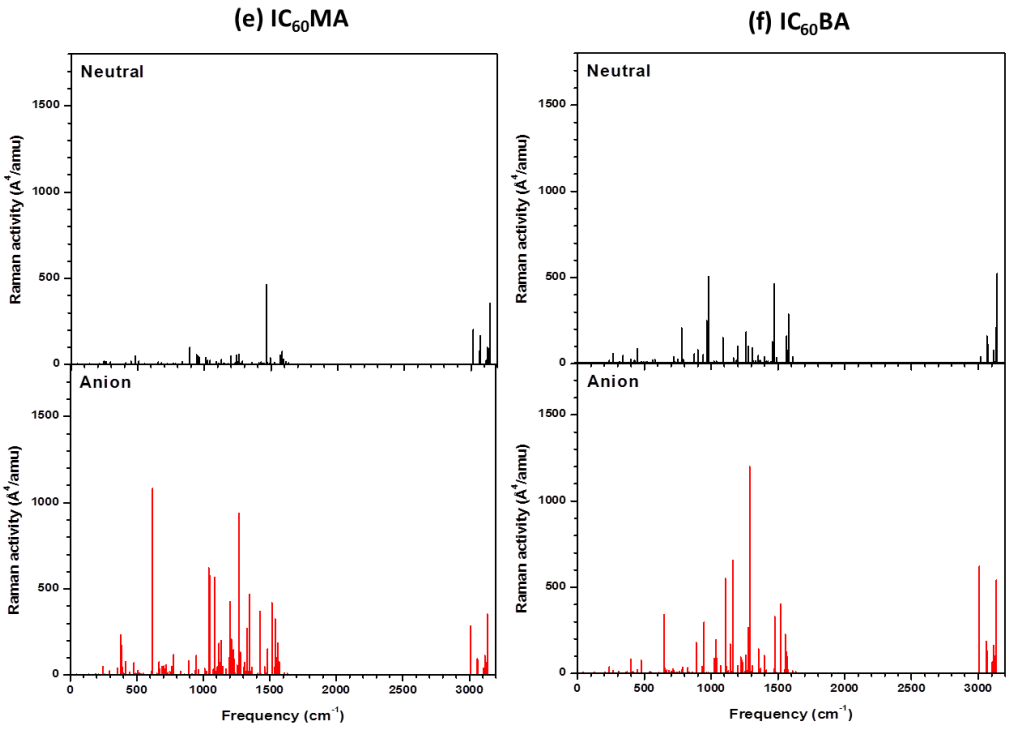


Figure 5.15 Raman spectra of (a) $C_{60}$, (b) $PC_{61}BM$-A, (c) $PC_{61}BM$-B, (d) bis-$PC_{61}BM$, (e) $IC_{60}MA$, and (f) $IC_{60}BA$ in the neutral (top-black line) and anion (bottom-red line) states, as calculated at the B3LYP/6-31G(d,p) level.

Table 5.4 Lists of changes in intensity and frequency of characteristic peaks in $C_{60}$ and its derivatives at the different charged state: Raman activities and frequencies are in Å/amu and $cm^{-1}$, respectively; $\nu_A$-$\nu_N$ represents frequency difference between the anion (A) and neutral (N) states; $I_A/I_N$, the ratio of intensity (I) of the anion (A) to the neutral (N).

| | | Neutral | | Anion | | Comparison | |
|---|---|---|---|---|---|---|---|
| Molecule | Mode | Frequency | Raman intensity | Frequency | Raman intensity | $\nu_A$-$\nu_N$ | $I_A/I_N$ |
| $C_{60}$ | Ag(2) | 1472.3 | 408.95 | 1465.7 | 90.97 | -6.6 | 0.22 |
| $PC_{61}BM$-A | Ag(2) of $C_{60}$ | 1467.8 | 283.79 | 1461.6 | 85.20 | -6.2 | 0.30 |
| $PC_{61}BM$-B | Ag(2) of $C_{60}$ | 1467.6 | 534.02 | 1461.6 | 85.61 | -6.0 | 0.16 |
| bis-$PC_{61}BM$ | Ag(2) of $C_{60}$ | 1461.7 | 726.32 | 1456.3 | 37.33 | -5.4 | 0.05 |
| $IC_{60}MA$ | Ag(2) of $C_{60}$ | 1466.2 | 464.94 | 1459.8 | 49.12 | -6.4 | 0.11 |
| $IC_{60}BA$ | Ag(2) of $C_{60}$ | 1458.7 | 507.33 | 1452.4 | 4.71 | -6.3 | 0.01 |

In $C_{70}$, the Raman active modes have $A_1'$, $E_2'$ and $E_1''$ symmetry.[31,32] As seen from Figure 5.16, in the case of the neutral $C_{70}$, the most intense Raman peaks are located at 1229 and 1575 $cm^{-1}$, that are assigned to the $A_1'$ modes.[31] The reduction of $C_{70}$ results in a downshift of most frequencies and leads to an enhanced Raman activity of the vibrational modes around 1000-1200 $cm^{-1}$, with the strongest effect on the 1032 and 1096 $cm^{-1}$ modes. Upon reduction of the $PC_{71}BM$-A, $PC_{71}BM$-B and bis-$PC_{71}BM$s, the Raman spectra also show enhancement of the Raman peaks around 1000-1200 $cm^{-1}$; the strongest effect is observed for the 1050 and 1134 $cm^{-1}$ modes in the case of both $PC_{71}BM$s and 1042 and 1124 $cm^{-1}$ in the case of bis-$PC_{71}BM$. Upon reduction, there is also no significant change in the Raman spectra of $PC_{71}BM$ in terms of the orientation of the functional group. In the case of $C_{70}$-based fullerene derivatives, it is difficult to select characteristic Raman peaks sensitive to the charging of the molecules.

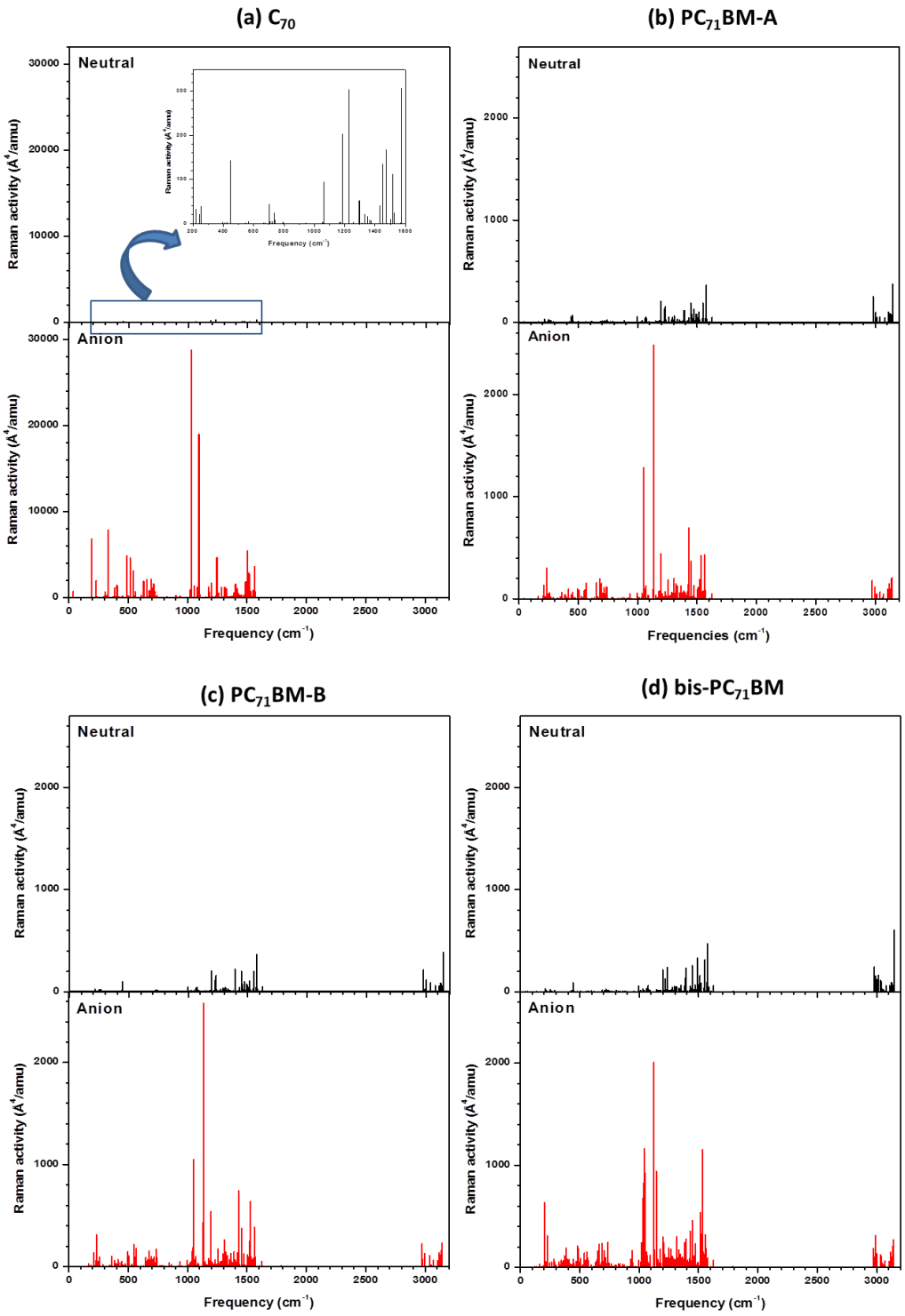


Figure 5.16 Raman spectra of (a) $C_{70}$, (b) $PC_{71}BM$-A, (c) $PC_{71}BM$-B, and (d) bis-$PC_{71}BM$ in the neutral (top-black line) and anion (bottom-red line) states, as calculated at the B3LYP/6-31G(d,p) level.

5.3.2.3 Infra-red (IR) spectroscopy

In $C_{60}$ only the $T_{1u}$ modes are IR active.[24,32] Upon reduction, as a result of symmetry lowering, more IR active modes are present. The main change upon reduction is a pronounced red-shift of $T_{1u}(4)$ three-fold degenerate mode at 1430 $cm^{-1}$ to 1386 $cm^{-1}$ with notable enhancement of the IR intensity (Figure 5.17 and Table 5.5). This means that this mode is quite sensitive with respect to the reduction of the molecule in terms of both frequency shift and intensity variation. This observation is in good agreement with the previous IR studies on the anion $C_{60}$.[14,33-37] This feature is also observed for $PC_{61}BM$ and indene derivatives. Thus for both $PC_{61}BM$-A and -B/bis-$PC_{61}BM$ and $IC_{60}MA$/$IC_{60}BA$, the IR peak around 1429 $cm^{-1}$ (corresponding to the $T_{1u}(4)$-like mode of $C_{60}$[38]) observed in the neutral molecules shifts upon reduction to 1385 $cm^{-1}$ and increases in intensity. These results support that the frequency change in the $T_{1u}(4)$-like mode can be used as an IR characteristic to probe the charge state of fullerene derivatives.

$PC_{61}BM$-A and -B, and bis-$PC_{61}BM$ molecules in the neutral state also show strong IR absorption around 1790 $cm^{-1}$ that is absent in $C_{60}$ and is attributed to the carbonyl (C=O) stretching in the butyric acid methyl ester on the $PC_{61}BM$ derivatives. However, the calculated frequency of the carbonyl mode of $PC_{61}BM$ is quite far from the frequency experimentally observed (about 1740 $cm^{-1}$).[5] It might be a result from the sensitivities of their carbonyl stretching mode to the local molecular/chemical environments.

Interestingly, we find a difference in frequency of the C=O stretching mode in terms of the conformation of the functional group of $PC_{61}BM$ upon reduction although there is no significant change in the intensity of the mode for both A and B conformations. There is

no significant frequency change in the carbonyl stretching mode of $PC_{61}BM$ in the A conformation, the lowest energy structure, when going from the neutral to the anion state (see Figure 5.17 and Table 5.5). On the other hand, the B conformation, the higher energy structure, exhibits a shift (-5 $cm^{-1}$) of the mode to lower frequency when adding an electron. Therefore, this result supports that in the gas phase, $PC_{61}BM$ molecules might have two possible conformations of the functional group. However, one might see average of the two conformations in experiment, since their energy difference (0.04 eV) is similar to KT at room temperature (~ 0.03 eV). In the case of bis-$PC_{61}BM$, there is no change in the frequency of the C=O stretching mode upon reduction since two functional groups both present A conformations.

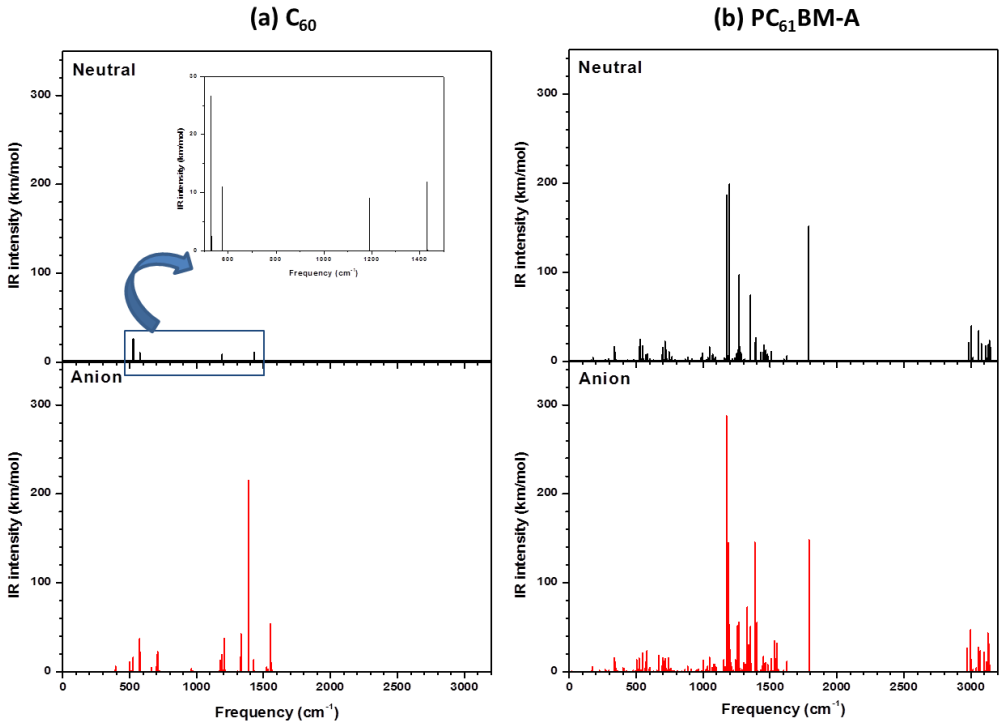

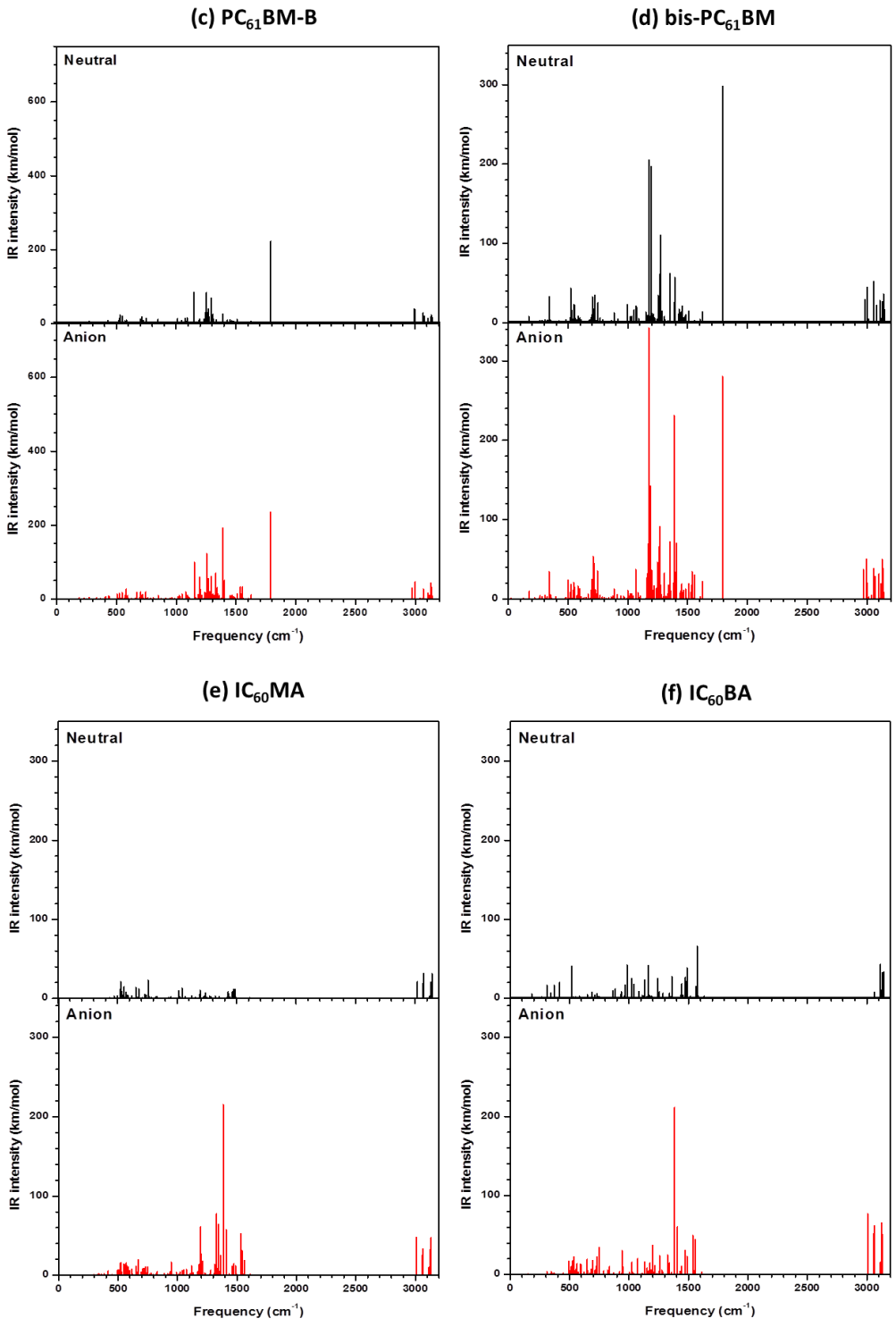


Figure 5.17 IR spectra of (a) $C_{60}$, (b) $PC_{61}BM$-A, (c) $PC_{61}BM$-B, (d) bis-$PC_{61}BM$, (e) $IC_{60}MA$, and (f) $IC_{60}BA$ in the neutral (top-black line) and anion (bottom-red line) states, as calculated at the B3LYP/6-31G(d,p) level.

Table 5.5 Lists of changes in intensity and frequency of characteristic peaks in $C_{60}$ and its derivatives at the different charged state: IR intensities and frequencies are in km/mol and $cm^{-1}$, respectively; $\nu_A$-$\nu_N$ represents frequency difference between the anion (A) and neutral (N) states; $I_A/I_N$, the ratio of intensity (I) of the anion (A) to the neutral (N).

| Molecule | Mode | Neutral | | Anion | | Comparison | |
|---|---|---|---|---|---|---|---|
| | | Frequency | IR intensity | Frequency | IR intensity | $\nu_A$-$\nu_N$ | $I_A/I_N$ |
| $C_{60}$ | $T_{1u}(4)$ | 1429.7 | 11.78 | 1386.1 | 215.28 | | |
| | | 1430.0 | 11.79 | 1386.6 | 213.16 | | |
| | | 1430.4 | 11.72 | | | | |
| | Avg. | 1430.0 | 35.29 | 1386.4 | 428.44 | -43.6 | 12.14 |
| $PC_{61}BM$-A | $T_{1u}(4)$ of $C_{60}$ | 1429.4 | 9.39 | 1385.2 | 145.97 | | |
| | | 1429.8 | 10.26 | | | | |
| | Avg. | 1429.6 | 19.65 | 1385.2 | 145.97 | -44.4 | 7.43 |
| | C=O stretching | 1789.0 | 151.59 | 1789.5 | 148.40 | 0.5 | 0.98 |
| $PC_{61}BM$-B | $T_{1u}(4)$ of $C_{60}$ | 1429.5 | 9.12 | 1384.7 | 192.55 | | |
| | | 1429.9 | 10.54 | | | | |
| | Avg. | 1429.7 | 19.66 | 1384.7 | 192.55 | -45.0 | 9.79 |
| | C=O stretching | 1792.5 | 223.04 | 1787.1 | 236.46 | -5.4 | 1.06 |
| bis-$PC_{61}BM$ | $T_{1u}(4)$ of $C_{60}$ | 1427.8 | 17.32 | 1384.0 | 233.19 | -43.8 | 13.46 |
| | C=O stretching | 1789.4 | 298.36 | 1789.0 | 249.16 | -0.4 | 0.84 |
| $IC_{60}MA$ | $T_{1u}(4)$ of $C_{60}$ | 1428.7 | 8.68 | 1385.2 | 215.81 | -43.5 | 24.86 |
| $IC_{60}BA$ | $T_{1u}(4)$ of $C_{60}$ | 1426.9 | 12.40 | 1383.9 | 211.50 | -43.0 | 17.06 |

For $C_{70}$, only the $E_1'$ and $A_2''$ modes are IR active.[31,32] As shown in Figure 5.18 and Table 5.6, the neutral $C_{70}$ molecule exhibits a strong IR peak at 1432 $cm^{-1}$ corresponding to the $E_1'$symmetry mode.[27,31,39-41] The reduction of $C_{70}$ causes a notable downshift of the two-fold degenerate mode at 1432 $cm^{-1}$ for the neutral to 1391 $cm^{-1}$ for the anion, a trend similar to those found in $C_{60}$. The fact that the vibrational mode at 1391 $cm^{-1}$ could be related to symmetry reduction upon charging was previously confirmed by experimental studies.[42,43] Like in $C_{60}$, this mode is sensitive to the charge state of the molecule.

In the case of $PC_{71}BM$, we also find a difference in frequency change in the C=O stretching mode between the A and B conformation upon reduction. Recall the A and B conformations have the $-CH_2CH_2-$ group and $-CH_2COOCH_3$ group of the functional group in the same plane and in different planes, respectively. There is no change of the C=O stretching mode in $PC_{71}BM$-A while the downshift by 5 $cm^{-1}$ of the mode is observed for $PC_{71}BM$-B, which is the same trend as those found in $PC_{61}BM$. Therefore, this result also supports that in the gas phase, $PC_{71}BM$ molecules might have two possible conformations of the functional group. Again, one might see average of the two conformations in experiment, since their energy difference (0.05 eV) is similar to KT at room temperature (~ 0.03 eV). For the bis-$PC_{71}BM$, two carbonyl stretching modes exist that are also downshifted upon reduction since the two functional groups both present B conformations.

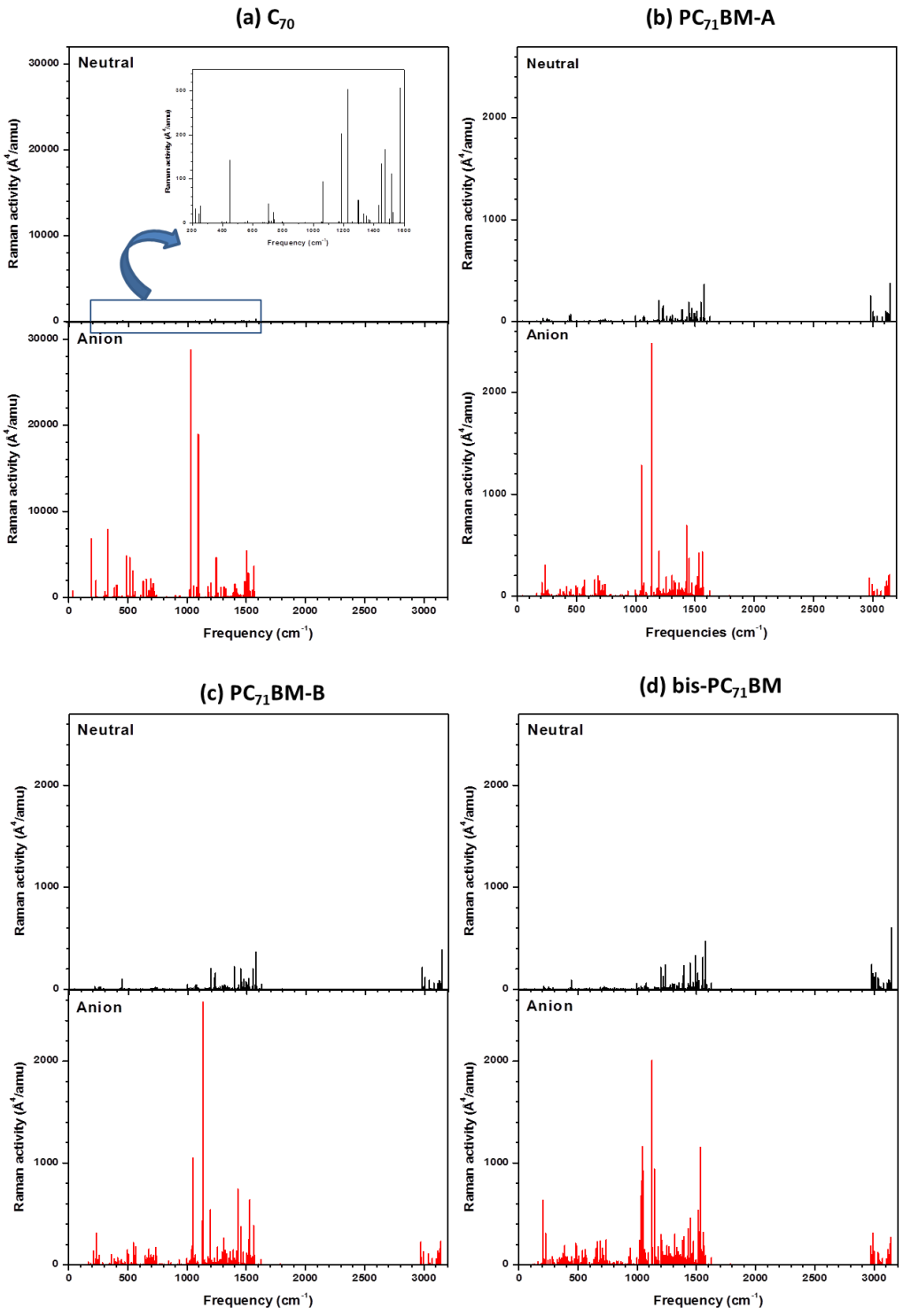


Figure 5.18 IR spectra of (a) $C_{70}$, (b) $PC_{71}BM$-A, (c) $PC_{71}BM$-B, and (d) bis-$PC_{71}BM$ in the neutral (top-black line) and anion (bottom-red line) states, as calculated at the B3LYP/6-31G(d,p) level.

Table 5.6 Lists of changes in intensity and frequency of characteristic peaks in $C_{70}$ and its derivatives molecule at the different charged state: IR intensities and frequencies are in km/mol and $cm^{-1}$, respectively; $\nu_A$-$\nu_N$ represents frequency difference between the anion (A) and neutral (N) states; $I_A/I_N$, the ratio of intensity (I) of the anion (A) to the neutral (N).

| Molecule | Mode | Neutral | | Anion | | Comparison | |
|---|---|---|---|---|---|---|---|
| | | Frequency | IR intensity | Frequency | IR intensity | $\nu_A$-$\nu_N$ | $I_A/I_N$ |
| $C_{70}$ | $E_1'$ | 1432.2 | 100.52 | 1391.2 | 117.62 | | |
| | | 1432.3 | 100.20 | | | | |
| | Avg. | 1432.3 | 200.72 | 1391.2 | 117.62 | -41.1 | 1.71 |
| $PC_{71}BM$-A | C=O stretching | 1789.1 | 149.14 | 1790.3 | 146.90 | 1.2 | 0.98 |
| $PC_{71}BM$-B | C=O stretching | 1792.6 | 225.26 | 1787.4 | 238.72 | -5.2 | 1.06 |
| bis-$PC_{71}BM$ | C=O stretching | 1792.3 | 223.17 | 1788.0 | 236.35 | -4.3 | 1.06 |
| | | 1788.1 | 212.19 | 1781.9 | 220.73 | -6.2 | 1.04 |

In order to consider the solvent effects on the vibrational spectra, we evaluated the IR spectra of $PC_{61}BM$ and $PC_{71}BM$ in the A and B conformations in the presence of a dielectric medium by using the polarizable continuum model (PCM). We used *o*-dichlorobenzene (ODCB) as the solvent for PCBM since this is widely used in the processing of organic electronic devices. The optimized PCBM structures in the A and B conformations remain nearly the same when the dielectric medium is considered. Interestingly, in Figure 5.19 and Table 5.7, there are no changes in the frequency and intensity of the C=O stretching mode of both $PC_{61}BM$ and $PC_{71}BM$ with different side group conformations (A and B) in the presence of the solvent when going from the neutral state to the anion. This might come from the fact that the dielectric medium surrounding the PCBM molecules shield the influence of different orientations of the

functional group on the stretching mode. From these calculations, we can conclude that there is no frequency change in the carbonyl stretching mode of PCBM derivatives upon reduction.

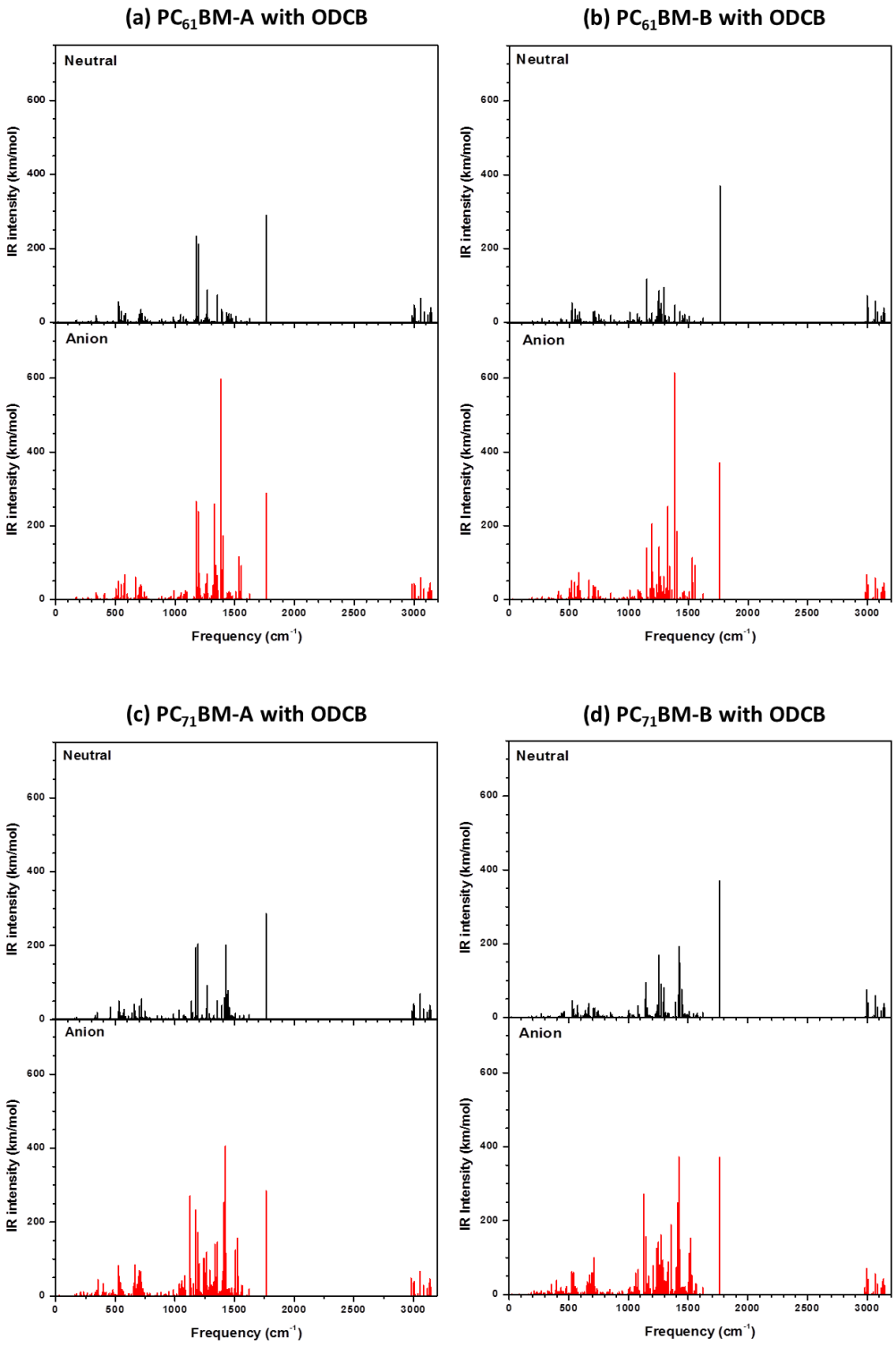


Figure 5.19 IR spectra of (a) $PC_{61}BM$-A, (b) $PC_{61}BM$-B, (c) $PC_{71}BM$-A, and (d) $PC_{71}BM$-B in the presence of o-dichlorobenzene (ODCB) in the neutral (top-black line) and anion (bottom-red line) states, as calculated at the B3LYP/6-31G(d,p) level.

Table 5.7 Lists of frequency and intensity of the carbonyl (C=O) stretching mode in PCBM derivatives at the different charged state: IR intensities and frequencies are in km/mol and $cm^{-1}$, respectively; $\nu_A$-$\nu_N$ represents frequency difference between the anion (A) and neutral (N) states; $I_A/I_N$, the ratio of intensity (I) of the anion (A) to the neutral (N).

| Molecules with solvent | Neutral | | Anion | | Comparison | |
|---|---|---|---|---|---|---|
| | Frequency | IR intensity | Frequency | IR intensity | $\nu_A$-$\nu_N$ | $I_A/I_N$ |
| $PC_{61}BM$-A | 1762.7 | 289.88 | 1762.4 | 289.05 | -0.3 | 0.98 |
| $PC_{61}BM$-B | 1762.7 | 370.46 | 1761.9 | 370.30 | -0.8 | 1.00 |
| $PC_{71}BM$-A | 1762.8 | 286.60 | 1763.1 | 284.08 | 0.3 | 0.99 |
| $PC_{71}BM$-B | 1762.6 | 371.23 | 1761.6 | 372.14 | -1.0 | 1.00 |

### 5.3.3 Redox and optical properties of the pristine polymers and fullerenes

#### 5.3.3.1 Redox properties

In most bulk-heterojunction solar cells studied to date, the conjugated polymers have served as the electron donor (hole transport) materials while the fullerenes and their derivatives act as the electron acceptor (electron transport) materials. Thus, we mainly focused on the ionization potential (IP) of the PBTTTs and electron affinity (EA) of the fullerene molecules to evaluate the redox properties of the polymer:fullerene system.

For the PBTTTs, we considered the planar backbone geometry as well as the twisted one (optimized geometry without any constraints); we expect the conjugated backbone of PBTTT to be planar in the solid state. Increasing the oligomer length makes the HOMO and LUMO energies destabilize and stabilize, respectively, leading to a reduced HOMO-LUMO gap in both instances (Table 5.8). We found a notable difference (~0.45 eV) in the HOMO-LUMO gap between the planar and twisted polymers, which will lead to

different absorption characteristics of the polymer in solution and in the solid state. The backbone planarity induces a better delocalization of electrons along the backbone, and stabilizes HOMO level and destabilizes LUMO level. The vertical and adiabatic ionization potentials (VIP and AIP, respectively) also decrease as the oligomer length increases.

Table 5.8 Calculated vertical and adiabatic ionization potentials (VIP and AIP), LUMO and HOMO energies, and HOMO-LUMO gap ($E_g$) of PBTTT as a function of oligomer length, from monomer to tetramer, for planar and twisted backbone geometries.

| Oligomer length | Backbone geometry | HOMO [eV] | LUMO [eV] | VIP [eV] | AIP [eV] | $E_g$ [eV] |
|---|---|---|---|---|---|---|
| Monomer | Planar | -4.94 | -1.69 | 6.26 | 6.10 | 3.25 |
| | Twisted | -5.21 | -1.49 | 6.54 | 6.19 | 3.72 |
| Dimer | Planar | -4.66 | -2.15 | 5.58 | 5.46 | 2.51 |
| | Twisted | -4.89 | -1.97 | 5.84 | 5.59 | 2.92 |
| Trimer | Planar | -4.58 | -2.29 | 5.31 | 5.23 | 2.29 |
| | Twisted | -4.81 | -2.09 | 5.57 | 5.38 | 2.73 |
| Tetramer | Planar | -4.55 | -2.36 | 5.16 | 5.10 | 2.19 |
| | Twisted | -4.78 | -2.14 | 5.42 | 5.27 | 2.64 |

The calculated intramolecular relaxation energies for PBTTT evaluated from the potential energy surfaces are collected in Table 5.9. As the oligomer length increases, the reorganization energy decreases due to the greater charge delocalization in longer oligomers. The planar structures have smaller reorganization energy (about 0.2~0.3 eV) compared to the twisted ones, since the optimal cation geometries are nearly planar.

Table 5.9 Estimates of relaxation energies for the neutral state and cation state, $\lambda_{rel}^{(1)}$ (meV) and $\lambda_{rel}^{(2)}$ (meV), and reorganization energy, $\lambda$ (meV), in PBTTT obtained from the adiabatic potential (AP) surfaces of the neutral and anion states.

| Oligomer length | Backbone geometry | Adiabatic potential (AP) surface | | |
|---|---|---|---|---|
| | | $\lambda_{rel}^{(1)}$ (meV) | $\lambda_{rel}^{(2)}$ (meV) | $\lambda$ (meV) |
| Monomer | Planar | 155 | 155 | 310 |
| | Twisted | 235 | 355 | 590 |
| Dimer | Planar | 119 | 114 | 233 |
| | Twisted | 208 | 244 | 452 |
| Trimer | Planar | 91 | 85 | 176 |
| | Twisted | 175 | 193 | 367 |
| Tetramer | Planar | 67 | 63 | 131 |
| | Twisted | 144 | 144 | 288 |

In the case of fullerenes, the EA of $C_{60}$ is similar to that of $C_{70}$ as shown in Table 5.10. Similar trends in EAs are obtained for $PC_{61}BM$ and $PC_{71}BM$, and bis-$PC_{61}BM$ and bis-$PC_{71}BM$. There is no significant change in the vertical electron affinity (VEA) and the adiabatic electron affinity (AEA) when the phenyl butyric acid methyl ester (PBM) functional group is attached onto $C_{60}$ and $C_{70}$. For instance, the VEA and AEA values decrease very little, by about 0.08 and 0.06 eV, when going from $PC_{61}BM$ to bis-$PC_{61}BM$, respectively. This suggests that the addition of the PBM functional groups onto the fullerenes have negligible effects on the redox properties. In the case of the indene adducts, the electron affinity is slightly lower than the corresponding $PC_{61}BM$ and bis-$PC_{61}BM$. Overall the electronic characteristics of indene-fullerenes are very similar to that of the PCBM family.

Table 5.10 Calculated vertical and adiabatic electron affinities (VEA and AEA), LUMO and HOMO energies, and HOMO-LUMO gap ($E_g$) for fullerenes, $C_{60}$ and $C_{70}$, their derivatives, PCBM, bis-PCBM, indene adducts.

| System | HOMO [eV] | LUMO [eV] | VEA [eV] | AEA [eV] | $E_g$ [eV] |
|---|---|---|---|---|---|
| $C_{60}$ | -3.23 | -5.99 | 2.00 | 2.06 | 2.76 |
| $C_{70}$ | -3.23 | -5.92 | 2.08 | 2.15 | 2.69 |
| $PC_{61}BM$ | -3.09 | -5.66 | 1.92 | 2.00 | 2.57 |
| $PC_{71}BM$ | -3.09 | -5.62 | 1.99 | 2.08 | 2.54 |
| bis-$PC_{61}BM$ | -2.97 | -5.45 | 1.86 | 1.94 | 2.47 |
| bis-$PC_{71}BM$ | -2.92 | -5.36 | 1.87 | 1.98 | 2.44 |
| $IC_{60}MA$ | -5.61 | -3.07 | 1.89 | 1.96 | 2.54 |
| $IC_{60}BM$ | -5.37 | -2.93 | 1.80 | 1.87 | 2.44 |

Attaching one functional group to the fullerenes, however, leads to a large decrease in the HOMO-LUMO gap ($E_g$), by about 0.2 eV for $C_{60}$ and 0.15 eV for $C_{70}$. Further functionalization decreases $E_g$ by 0.1 eV compared to PCBM. This is the result of a larger energetic destabilization of the HOMO relative to that seen for the LUMO.

Figure 5.20 displays the vertical electron affinity (VEA) as a function of LUMO energy in order to establish a relationship between the data. As expected, there is a strong linear relationship between the VEA and LUMO energy for each fullerene-based derivative family, *i.e.*, when going from fullerene to either PCBM derivatives or indene adducts. It clearly confirms that the deeper the LUMO level, the larger the AEA and VEA.

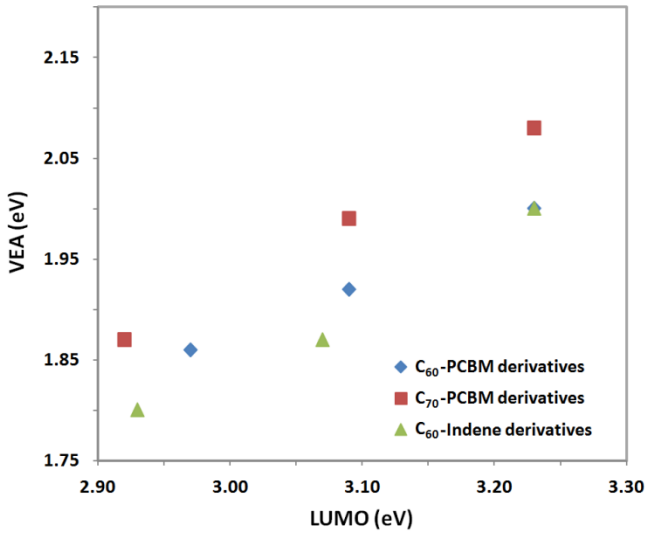


Figure 5.20 Plot of vertical electron affinity (VEA) of a series of fullerenes as a function of LUMO energy.

The reorganization energy and relaxation energy upon reduction are listed in Table 5.11. The results obtained both from adiabatic potential (AP) surface and normal mode (NM) analyses are in good agreement. The estimated reorganization energy of $C_{60}$, 0.135 eV, is consistent with the results of previous calculation, 0.132 eV[44] and 0.140 eV.[45] On adding the phenyl butyric acid methyl ester functional group on $C_{60}$, there is a little change in the relaxation energy in the neutral (or anion) state. In the case of $C_{70}$-based fullerene molecules, on the other hand, the relaxation energy increases very slightly, 0.02 eV, upon adding the functional group. The reorganization energy of $IC_{60}MA$ and $IC_{60}BA$ is very close to that of $C_{60}$ and slightly smaller than in $PC_{61}BM$. These small reorganization energies of fullerenes and their derivatives can provide for efficient electron transfer.[46]

Table 5.11 Estimates of relaxation energies for neutral state and anion state, $\lambda_{rel}^{(1)}$ (meV) and $\lambda_{rel}^{(2)}$ (meV), and reorganization energy, $\lambda$ (meV), in two different fullerenes, $C_{60}$ and $C_{70}$, and their derivatives obtained from adiabatic potential (AP) surface of both neutral and anion states and normal mode (NM) analysis.

| | Adiabatic potential (AP) surface | | | Normal mode (NM) analysis | | |
|---|---|---|---|---|---|---|
| | $\lambda_{rel}^{(1)}$ (meV) | $\lambda_{rel}^{(2)}$ (meV) | $\lambda$ (meV) | $\lambda_{rel}^{(1)}$ (meV) | $\lambda_{rel}^{(2)}$ (meV) | $\lambda$ (meV) |
| $C_{60}$ | 70 | 65 | 135 | 68 | 67 | 135 |
| $C_{70}$ | 80 | 67 | 147 | 80 | 77 | 157 |
| $PC_{61}BM$ | 75 | 75 | 150 | 75 | 74 | 149 |
| $PC_{71}BM$ | 95 | 90 | 185 | 95 | 94 | 189 |
| bis-$PC_{61}BM$ | 79 | 80 | 159 | 80 | 82 | 162 |
| bis-$PC_{71}BM$ | 105 | 116 | 221 | 106 | 105 | 211 |
| $IC_{60}MA$ | 69 | 68 | 137 | 69 | 69 | 138 |
| $IC_{60}BM$ | 69 | 68 | 137 | 70 | 69 | 139 |

Figure 5.21 shows the decomposition of the relaxation energies into contributions from the normal modes of the molecules in the neutral and anion states. The results of normal mode calculations confirm that the relaxation energy of $C_{60}$, $PC_{61}BM$, bis-$PC_{61}BM$, $IC_{60}MA$, and $IC_{60}BA$ mainly arises from high-energy vibrations (1400-1600 $cm^{-1}$), while $C_{70}$, mono-$PC_{71}BM$, and bis-$PC_{71}BM$ also display modest contributions from vibrations in two distinct ranges, 200-800 $cm^{-1}$ and 1200-1800 $cm^{-1}$.

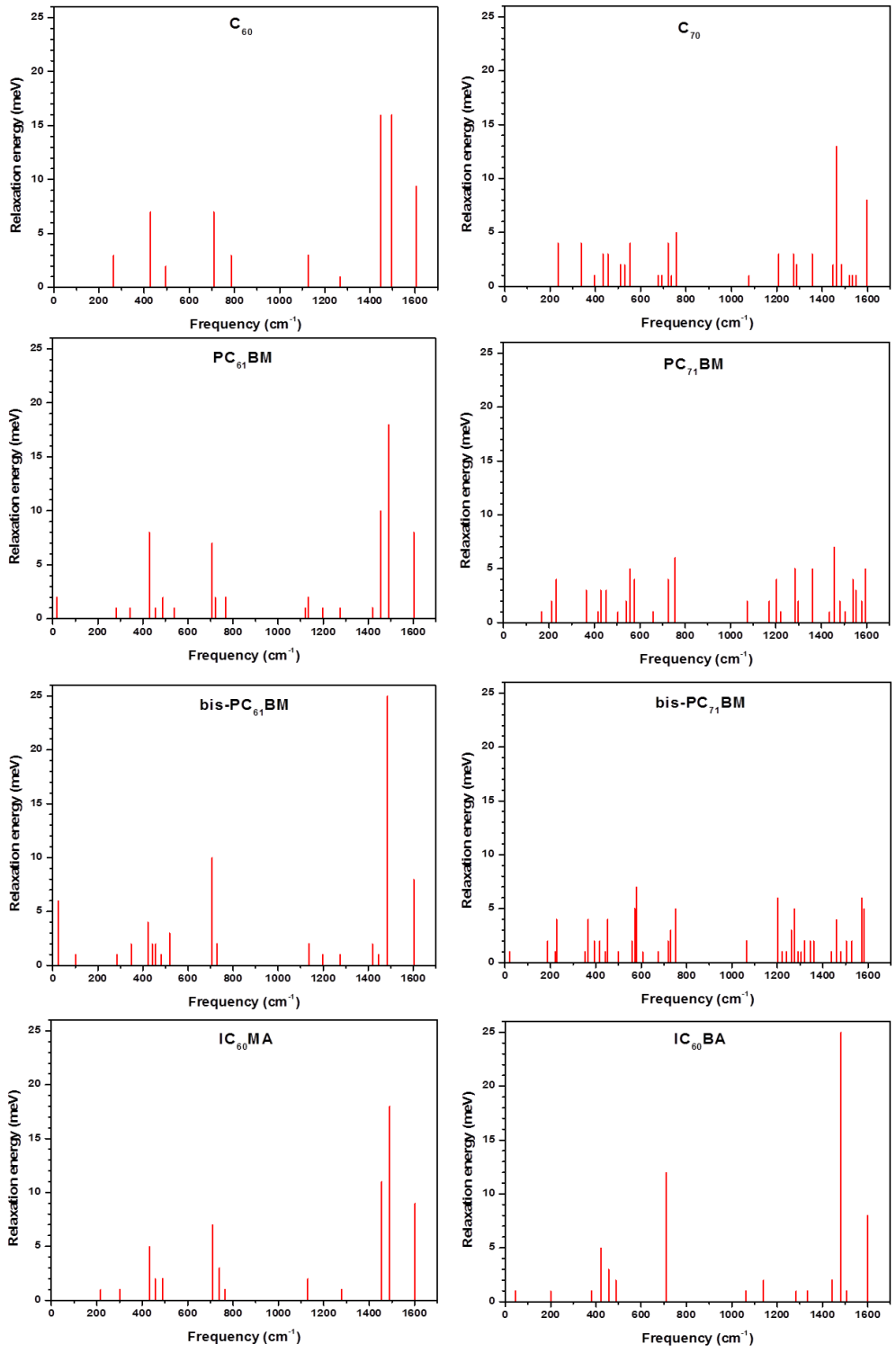


Figure 5.21 Individual contributions of the normal modes in $C_{60}$ and $C_{70}$, and their derivatives at the anion state to the relaxation energy from normal mode calculations.

For the PCBM derivatives, interestingly, we find that upon adding the functional groups to $C_{60}$, the contribution of the vibrational mode around 1472 $cm^{-1}$ to the total relaxation energy increases from 21% to 26 % and 29%, and the frequency is downshifted to 1468 $cm^{-1}$ and 1462 $cm^{-1}$. These are associated with the strongest Raman-active modes in the neutral state ($A_g(2)$ mode) corresponding to a symmetric C=C stretching mode on the $C_{60}$ cage. Other large contributions appear around 430, 705, 1425, and 1584 $cm^{-1}$ and are related to $H_g$ symmetry,[47] active in the anion state due to geometry distortion. Previous studies on the $C_{60}$ anion[48,49] revealed a large electron-phonon coupling constant for the $H_g$ modes, mostly at 437, and 1428, and 1575 $cm^{-1}$, in agreement with our calculated data except for 1472 $cm^{-1}$. For the indene adducts, the strongest contribution also originates from the Ag(2) Raman active mode corresponding to the C=C symmetric stretch on the $C_{60}$ cage, similar to that for PCBM. Thus, the strongest relaxation process is related to the geometrical distortion along this vibrational mode.

5.3.3.2 Optical properties

As we have noted earlier that substitution introduces a significant change in the HOMO-LUMO gap, similar changes – assuming that the lowest-lying transition is HOMO→LUMO – should be observed for the lowest-lying excitation energy. Table 5.12 collects the TDDFT excitation energies of the first singlet ($S_1$) and triplet ($T_1$) excited states of PBTTT as a function of oligomer length and backbone geometries. As the oligomer length increases from monomer to tetramer in the neutral state, the $S_1$ excitation energies decrease from 3.06 to 1.88 eV for the planar structure and from 3.41 to 2.26 eV for the twisted structures. The $T_1$ excitation energies in the neutral state also shift to lower

energies for longer oligomer lengths for both backbone geometries. In addition, the energy difference between $S_1$ and $T_1$ decreases as well from 1.21 to 0.65 eV for the planar structures and from 1.21 to 0.67 eV for the twisted structures when going from monomer to tetramer. As expected, backbone planarity induces a red shift (by about 0.4 eV) of the $S_1$ and $T_1$ energies due to the decrease in the conjugation length by the quinoidal character of the backbone.

Upon oxidation (positive polaron formation), the optimized structure becomes planar and there is subsequent increase in the quinoidal character across the backbones. This leads to the first doublet ($D_1$) excitation energies at 0.5 ~ 1.5 eV, which is in agreement with experimental observation in the oxidized conjugated polymers: there are two strong absorption bands at ~0.5 and ~1.5 eV, characteristics of cation radicals (polarons).[50-52]

Table 5.12 Excitation energies of the first singlet ($S_1$), doublet ($D_1$), and triplet ($T_1$) excited states for the optimized neutral and cation PBTTT states as a function of backbone geometry.

| Oligomer length | Backbone geometry | Neutral | Cation | Neutral |
|---|---|---|---|---|
| | | $S_1$ [eV] | $D_1$ [eV] | $T_1$ [eV] |
| Monomer | Planar | 3.06 | 1.54 | 1.78 |
| | Twisted | 3.41 | | 2.20 |
| Dimer | Planar | 2.25 | 0.83 | 1.37 |
| | Twisted | 2.58 | | 1.70 |
| Trimer | Planar | 1.99 | 0.58 | 1.27 |
| | Twisted | 2.36 | | 1.62 |
| Tetramer | Planar | 1.88 | 0.41 | 1.23 |
| | Twisted | 2.26 | | 1.59 |

Table 5.13 collects the characteristics of electronic absorption to the first singlet ($S_1$) and triplet ($T_1$) excited states for the fullerene series. We found that adding the functional group on fullerenes has very minor effect on the $S_1$ and $T_1$ energies in neutral state. Comparing to the PCBM family, the absorption properties of indene-fullerenes are similar to those of PCBM. Experimental absorption spectra of $C_{60}$ and $C_{70}$ present similar onset,[53] at about 635 nm for $C_{60}$ and 650 nm for $C_{70}$, the same trend in $S_1$ energy from our calculations. Upon reduction (negative polaron formation), we found the first doublet ($D_1$) energies for fullerene series at 0.2 ~ 0.3 eV.

Table 5.13 Excitation energies of the first singlet ($S_1$), doublet ($D_1$), and triplet ($T_1$) excited states for $C_{60}$, $C_{70}$, $PC_{61}BM$, $PC_{71}BM$, bis-$PC_{61}BM$, bis-$PC_{71}BM$, $IC_{60}MA$, and $IC_{60}BA$ in the neutral and anion states.

| System | Neutral | Anion | Neutral |
|---|---|---|---|
| | $S_1$ [eV] | $D_1$ [eV] | $T_1$ [eV] |
| $C_{60}$ | 2.09 | 0.16 | 1.59 |
| $C_{70}$ | 2.11 | 0.19 | 1.52 |
| $PC_{61}BM$ | 1.93 | 0.21 | 1.52 |
| $PC_{71}BM$ | 2.01 | 0.27 | 1.48 |
| bis-$PC_{61}BM$ | 1.83 | 0.26 | 1.49 |
| bis-$PC_{71}BM$ | 1.86 | 0.23 | 1.43 |
| $IC_{60}MA$ | 1.91 | 0.19 | 1.53 |
| $IC_{60}BM$ | 1.80 | 0.18 | 1.52 |

## 5.4 Conclusions

We have investigated the IR and Raman properties of pristine PBTTT and a series of fullerenes. In the case of pristine PBTTT, the calculated C=C-C stretching modes of the backbones are consistent with experiment. When the number of repeat units is greater than three, both the frequency and intensity hardly change with respect to oligomer length and repeat-unit conformation. This indicates that the PBTTT trimer is sufficient to well represent the vibrational properties of the polymer. We find red shifts of the vibrational modes in the Raman spectra as the backbone either becomes planar or is oxidized. For the IR active modes, we also found notable downshifts of aromatic C-H out of plane deformation and symmetric/antisymmetric C=C stretching modes. Therefore, these vibrations can be used as a tool to analyze the presence of hole carriers in PBTTT.

For the fullerene derivatives, we found that reduction affects the bond-length variations and the vibration modes active in IR and Raman spectra. The calculated Raman spectra show a downshift of the strong pentagon pinch mode ($A_g(2)$) of $C_{60}$ for $C_{60}$-based fullerenes and derivatives upon reduction while overall downshifts of the frequencies are observed for $C_{70}$-based fullerenes and derivatives. From the calculated IR spectra, we determined the characteristic vibrational modes sensitive to reduction, the $T_{1u}(4)$ mode of $C_{60}$ and $E_{1'}$ mode of $C_{70}$. Therefore, these vibrations can be used as a tool to analyze the charge state of fullerenes. An interesting observation is that reduction might result in the frequency downshift of the C=O stretching IR peaks in PCBM and bis-PCBM according to the relative orientation of butyric acid group on the fullerene cage in the gas phase, although it does not affect the intensity of those peaks. In the presence of a dielectric

medium, however, this frequency is nearly the same in the neutral and anion states due to shielding effects.

Regarding the redox and optical properties of PBTTT, we determined the influence of the oligomer length and backbone geometry on their properties. Upon increasing the oligomer length from monomer to tetramer, the ionization potential decreases by about 0.4 eV. The backbone planarity contributes to a decrease of 0.1-0.3 eV in the ionization potential and a red-shift of 0.45 eV in HOMO-LUMO gap. The reorganization energy decreases for longer chains due to the greater charge delocalization in longer oligomers. TD-DFT calculations confirm that backbone planarity leads to red-shifts by 0.4 eV of the first singlet and triplet excitation energies. Upon oxidation, the first doublet excitation energies are obtained at 0.5 ~ 1.5 eV, related to positive polaron formation.

The fullerenes and their derivatives have relatively large electron affinities and small reorganization energies, which make them ideal candidates as electron-transport materials in organic electronic applications. The results of normal-mode calculations indicate that the relaxation energy of $C_{60}$ and its PCBM derivatives is mainly due to high-energy vibrations (1400-1600 $cm^{-1}$), while $C_{70}$ and its PCBM derivatives also have modest contributions from vibrations in two distinct ranges, 200-800 $cm^{-1}$ and 1200-1800 $cm^{-1}$. In the case of $C_{60}$-based molecules, we find that the largest contribution to the relaxation process of charge transfer in the $C_{60}$-based molecules is coming from a Raman active $A_g(2)$ vibrational mode. TD-DFT calculations show that the first singlet and triplet excitation energies of fullerene derivatives are similar to those of fullerenes. Upon

reduction, negative polaron formation leads to the first doublet excitation energies of fullerenes and their derivatives at 0.2 ~ 0.3 eV.

This work provides useful guidelines to understand the evolution of the vibrational and electronic spectra as a function of charging of the molecules in the blend upon oxidation and reduction.

## 5.5 References


(1) Chappell, J. S.; Bloch, A. N.; Bryden, W. A.; Maxfield, M.; Poehler, T. O.; Cowan, D. O. *J. Am. Chem. Soc.* **1981**, *103*, 2442.

(2) Rao, A. M.; Eklund, P. C.; Bandow, S.; Thess, A.; Smalley, R. E. *Nature* **1997**, *388*, 257.

(3) Claye, A.; Rahman, S.; Fischer, J. E.; Sirenko, A.; Sumanasekera, G. U.; Eklund, P. C. *Chem. Phys. Lett.* **2001**, *333*, 16.

(4) Elliott, A. B. S.; Horvath, R.; Gordon, K. C. *Chem. Soc. Rev.* **2012**, *41*, 1929.

(5) Barbour, L. W.; Hegadorn, M.; Asbury, J. B. *J. Am. Chem. Soc.* **2007**, *129*, 15884.

(6) Falke, S.; Eravuchira, P.; Materny, A.; Lienau, C. *J. Raman Spectrosc.* **2011**, *42*, 1897.

(7) He, Y. J.; Chen, H. Y.; Hou, J. H.; Li, Y. F. *J. Am. Chem. Soc.* **2010**, *132*, 5532.

(8) Frisch, M. J.; Trucks, G. W.; Schlegel, H. B.; Scuseria, G. E.; Robb, M. A.; Cheeseman, J. R.; Scalmani, G.; Barone, V.; Mennucci, B.; Petersson, G. A.; Nakatsuji, H.; Caricato, M.; Li, X.; Hratchian, H. P.; Izmaylov, A. F.; Bloino, J.; Zheng, G.; Sonnenberg, J. L.; Hada, M.; Ehara, M.; Toyota, K.; Fukuda, R.; Hasegawa, J.; Ishida, M.; Nakajima, T.; Honda, Y.; Kitao, O.; Nakai, H.; Vreven, T.; Montgomery, J., J. A.; Peralta, J. E.; Ogliaro, F.; Bearpark, M.; Heyd, J. J.; Brothers, E.; Kudin, K. N.; Staroverov, V. N.; Kobayashi, R.; Normand, J.; Raghavachari, K.; Rendell, A.; Burant, J. C.; Iyengar, S. S.; Tomasi, J.; Cossi, M.; Rega, N.; Millam, J. M.; Klene, M.; Knox, J. E.; Cross, J. B.; Bakken, V.; Adamo, C.; Jaramillo, J.; Gomperts, R.; Stratmann, R. E.; Yazyev, O.; Austin, A. J.; Cammi, R.; Pomelli, C.; Ochterski, J. W.; Martin, R. L.; Morokuma, K.; Zakrzewski, V. G.; Voth, G. A.; Salvador, P.; Dannenberg, J. J.; Dapprich, S.; Daniels, A. D.; Farkas, Ö.; Foresman, J. B.; Ortiz, J. V.; Cioslowski, J.; Fox, D. J. In *Gaussian 09, Revision A.02*; Gaussian, Inc.: Wallingford, CT, 2009.

(9) Tsoi, W. C.; James, D. T.; Kim, J. S.; Nicholson, P. G.; Murphy, C. E.; Bradley, D. D. C.; Nelson, J. *J. Am. Chem. Soc.* **2011**, *133*, 9834.

(10) Kato, T. *J. Chem. Phys.* **1971**, *54*, 5398.

(11) McCreey, R. L. *Handbook of vibrational spectroscopy*; Wiley: New York, 2002; Vol. 1.

(12) Michalska, D.; Wysokinski, R. *Chem. Phys. Lett.* **2005**, *403*, 211.

(13) Stratmann, R. E.; Scuseria, G. E.; Frisch, M. J. *J. Raman Spectrosc.* **1998**, *29*, 483.

(14) Fu, K. J.; Karney, W. L.; Chapman, O. L.; Huang, S. M.; Kaner, R. B.; Diederich, F.; Holczer, K.; Whetten, R. L. *Phys. Rev. B* **1992**, *46*, 1937.

(15) Gao, Y. Q.; Grey, J. K. *J. Am. Chem. Soc.* **2009**, *131*, 9654.

(16) Gao, Y. Q.; Martin, T. P.; Thomas, A. K.; Grey, J. K. *J. Phys. Chem. Lett.* **2010**, *1*, 178.

(17) Cho, E.; Risko, C.; Kim, D.; Gysel, R.; Miller, N. C.; Breiby, D. W.; McGehee, M. D.; Toney, M. F.; Kline, R. J.; Bredas, J. L. *J. Am. Chem. Soc.* **2012**, *134*, 6177.

(18) Johnson, R. D.; Meijer, G.; Bethune, D. S. *J. Am. Chem. Soc.* **1990**, *112*, 8983.

(19) Andreoni, W. *Annu. Rev. Phys. Chem.* **1998**, *49*, 405.

(20) Boulas, P.; Dsouza, F.; Henderson, C. C.; Cahill, P. A.; Jones, M. T.; Kadish, K. M. *J. Phys. Chem.* **1993**, *97*, 13435.

(21) Johnson, R. D.; Meijer, G.; Salem, J. R.; Bethune, D. S. *J. Am. Chem. Soc.* **1991**, *113*, 3619.

(22) Choi, C. H.; Kertesz, M.; Mihaly, L. *J. Phys. Chem. A* **2000**, *104*, 102.

(23) Sun, G. Y.; Kertesz, M. *J. Phys. Chem. A* **2002**, *106*, 6381.

(24) Kroto, H. W.; Allaf, A. W.; Balm, S. P. *Chem. Rev.* **1991**, *91*, 1213.

(25) Lannoo, M.; Baraff, G. A.; Schluter, M.; Tomanek, D. *Phys. Rev. B* **1991**, *44*, 12106.

(26) Bethune, D. S.; Meijer, G.; Tang, W. C.; Rosen, H. J. *Chem. Phys. Lett.* **1990**, *174*, 219.

(27) Bethune, D. S.; Meijer, G.; Tang, W. C.; Rosen, H. J.; Golden, W. G.; Seki, H.; Brown, C. A.; Devries, M. S. *Chem. Phys. Lett.* **1991**, *179*, 181.

(28) Haddon, R. C.; Hebard, A. F.; Rosseinsky, M. J.; Murphy, D. W.; Duclos, S. J.; Lyons, K. B.; Miller, B.; Rosamilia, J. M.; Fleming, R. M.; Kortan, A. R.; Glarum, S. H.; Makhija, A. V.; Muller, A. J.; Eick, R. H.; Zahurak, S. M.; Tycko, R.; Dabbagh, G.; Thiel, F. A. *Nature* **1991**, *350*, 320.

(29) McGlashen, M. L.; Blackwood, M. E.; Spiro, T. G. *J. Am. Chem. Soc.* **1993**, *115*, 2074.

(30) Kuzmany, H.; Pfeiffer, R.; Hulman, M.; Kramberger, C. *Philos. Trans. R. Soc. Lond. Ser. A-Math. Phys. Eng. Sci.* **2004**, *362*, 2375.

(31) Schettino, V.; Pagliai, M.; Cardini, G. *J. Phys. Chem. A* **2002**, *106*, 1815.

(32) Nakamoto, K. *Infrared and raman spectra of inorganic and coordination compounds part a*; John Wiley: New York, 1922.

(33) Kamaras, K.; Tanner, D. B.; Forro, L.; Martin, M. C.; Mihaly, L.; Klos, H.; Gotschy, B. *J. Supercond.* **1995**, *8*, 621.

(34) Semkin, V. N.; Spitsina, N. G.; Krol, S.; Graja, A. *Chem. Phys. Lett.* **1996**, *256*, 616.

(35) Kupser, P.; Steill, J. D.; Oomens, J.; Meijer, G.; von Helden, G. *Phys. Chem. Chem. Phys.* **2008**, *10*, 6862.

(36) Giannozzi, P.; Andreoni, W. *Phys. Rev. Lett.* **1996**, *76*, 4915.

(37) Kuzmany, H.; Winkler, R.; Pichler, T. *J. Phys.-Condes. Matter* **1995**, *7*, 6601.

(38) Wei, Q. S.; Tajima, K.; Tong, Y. J.; Ye, S.; Hashimoto, K. *J. Am. Chem. Soc.* **2009**, *131*, 17597.

(39) Vonczarnowski, A.; Meiwesbroer, K. H. *Chem. Phys. Lett.* **1995**, *246*, 321.

(40) Nemes, L.; Ram, R. S.; Bernath, P. F.; Tinker, F. A.; Zumwalt, M. C.; Lamb, L. D.; Huffman, D. R. *Chem. Phys. Lett.* **1994**, *218*, 295.

(41) Bowmar, P.; Hayes, W.; Kurmoo, M.; Pattenden, P. A.; Green, M. A.; Day, P.; Kikuchi, K. *J. Phys.-Condes. Matter* **1994**, *6*, 3161.

(42) Lobach, A. S.; Goldshleger, N. F.; Kaplunov, M. G.; Kulikov, A. V. *Chem. Phys. Lett.* **1995**, *243*, 22.

(43) Lawson, D. R.; Feldheim, D. L.; Foss, C. A.; Dorhout, P. K.; Elliott, C. M.; Martin, C. R.; Parkinson, B. *J. Phys. Chem.* **1992**, *96*, 7175.

(44) Nelson, J.; Kwiatkowski, J. J.; Kirkpatrick, J.; Frost, J. M. *Acc. Chem. Res.* **2009**, *42*, 1768.

(45) Cheung, D. L.; Troisi, A. *J. Phys. Chem. C* **2010**, *114*, 20479.

(46) Imahori, H.; Hagiwara, K.; Akiyama, T.; Aoki, M.; Taniguchi, S.; Okada, T.; Shirakawa, M.; Sakata, Y. *Chem. Phys. Lett.* **1996**, *263*, 545.

(47) Zhang, Y.; Edens, G.; Weaver, M. J. *J. Am. Chem. Soc.* **1991**, *113*, 9395.

(48) Antropov, V. P.; Gunnarsson, O.; Liechtenstein, A. I. *Phys. Rev. B* **1993**, *48*, 7651.

(49) Gunnarsson, O.; Handschuh, H.; Bechthold, P. S.; Kessler, B.; Gantefor, G.; Eberhardt, W. *Phys. Rev. Lett.* **1995**, *74*, 1875.

(50) Kim, Y. H.; Spiegel, D.; Hotta, S.; Heeger, A. J. *Phys. Rev. B* **1988**, *38*, 5490.

(51) Voss, K. F.; Foster, C. M.; Smilowitz, L.; Mihailovic, D.; Askari, S.; Srdanov, G.; Ni, Z.; Shi, S.; Heeger, A. J.; Wudl, F. *Phys. Rev. B* **1991**, *43*, 5109.

(52) Kao, C. Y.; Lee, B.; Wielunski, L. S.; Heeney, M.; McCulloch, I.; Garfunkel, E.; Feldman, L. C.; Podzorov, V. *Adv. Funct. Mater.* **2009**, *19*, 1906.

(53) Ajie, H.; Alvarez, M. M.; Anz, S. J.; Beck, R. D.; Diederich, F.; Fostiropoulos, K.; Huffman, D. R.; Kratschmer, W.; Rubin, Y.; Schriver, K. E.; Sensharma, D.; Whetten, R. L. *J. Phys. Chem.* **1990**, *94*, 8630.

# CHAPTER 6

# CONCLUSIONS

## 6.1 Synopsis

The field of organic photovoltaics has been rapidly growing due to its potential in offering sustainable/renewable energy resources. Tremendous efforts are paid to improve the performance of organic photovoltaics and understand the physical mechanisms involved in the photoconversion process. From a computational/theoretical perspective, it is important to elucidate the structure-property relationships at the molecular scale in the polymer:fullerene blends widely used in organic solar cells. This can provide insight into aspects related to device performance that are not attainable experimentally. In this dissertation, the relationships between geometric structure, packing mode, electronic states, and vibrational modes of an intercalated polymer:fullerene blend were investigated using a wide range of computational methods.

First, the three-dimensional orientation of PBTTT-$C_{14}$ films was determined using a combination of 2D grazing incidence X-ray diffraction (GIXD) experiments and computational modeling. It was shown that the conjugated polymer backbones are coplanar and have relatively short intermolecular distances. The alkyl side chains are interdigitated amongst neighboring side chains, which contributes to a large degree of structural ordering by forming a lamellar structure. In-plane GIXD simulations were carried out for the first time in this work and very reasonable agreement between experiment and theory was obtained. Moreover, the modeling allowed us to further

examine the influences of the molecular packing parameters and of the individual polymer components to the GIXD pattern. The geometric and packing structures of polymers with side chains of varying size, from $C_{12}$ to $C_{16}$, were also determined. Quantum-chemical calculations confirm the possibility of efficient intra- and inter-chain charge transport along between the polymer backbones regardless of the side-chain length. These results lead to a better understanding of the relationship between polymer packing and electronic structure and are an important step forward in unraveling the complexity of conjugated polymers. Therefore, the combination of computational and experimental techniques exploited in our work can foster rational design concepts for new molecular and polymeric materials for organic electronic applications.

Second, we determined the detailed packing configuration of the intercalated polymer:fullerene bimolecular crystal using a series of molecular modeling techniques; the structures were refined against available solid-state NMR and GIXD data. Good agreement amongst results from the various experimental techniques supported the accuracy and validity of our proposed structural model for the bimolecular crystal, and suggested that the combination of these experimental and computational techniques could be applied to other complicated bulk-heterojunction systems. It was revealed that the conformation of the polymer chains are significantly disrupted upon incorporation of the fullerene molecules; the latter induce twists and bends along the polymer backbones and present quasi one-dimensional fullerene channels for electron transport. These results suggest that the strong polymer:fullerene interactions affect the local structure of the blend, and thus have an impact on important processes in organic solar cells. Therefore,

this work provides a first detailed insight into how conjugated polymers interact/assemble with fullerene molecules in intercalated polymer:fullerene blends and offers an in-depth molecular picture of the relationship between packing and charge-transport properties in the bimolecular crystal. In addition, calculations of interaction/binding energies and cohesive energy density provide useful details regarding molecular mixing.

Finally, we determined the intrinsic vibrational, redox, and optical properties of the polymers and fullerenes. Our comprehensive theoretical study of the IR and Raman spectra points to a series of characteristic vibrations that can be used as a tool to probe the extent of charge on the system; this provides a valuable guide for better understanding the relationship between the spectroscopic changes and the properties of the polymer:fullerene blends.

### 6.2 Further considerations

The theoretical results in this dissertation have provided a step toward in a comprehensive understanding of the relationships between geometric structure, packing mode, electronic states, and vibrational modes of intercalated polymer:fullerene blends. In order to gain an even deeper insight into elucidating these relationships, several aspects are worthy of further investigations:

(i) Regarding the structural determination of the pristine polymer or the intercalated polymer:fullerene blend, we have considered initially a single unit cell with periodic boundary conditions. To evaluate the thermodynamic disorder, we carried out molecular

dynamics (MD) simulations on medium-sized supercells. However, this choice might bring limitations in order to capture all possible disorders, such as various orientations of the $PC_{71}BM$ molecules, different conformations of the polymers, or vicinity of $PC_{71}BM$. Thus, it would be useful to be able to perform large-scale MD simulations with various molar ratios to characterize the microstructure morphology of the system. In addition, it is also important to extend the X-ray simulation software to describe the GIXD patterns of the supercell including the peak broadening and diffuse scattering.

(ii) We determined the interaction energies and free energy of mixing based on the crystal unit cell of the polymer, $PC_{71}BM$, and polymer:$PC_{71}BM$ blend. Since there is no available $PC_{71}BM$ crystal structure, we proposed a model using molecular mechanics simulations. It is known that PCBM is amorphous at room temperature. Thus, it would be helpful to evaluate interaction energy of amorphous $PC_{71}BM$ to provide for more direct/robust insight in terms of energy of mixing.

(iii) In Chapter 5, we analyzed the IR and Raman spectra of the pristine polymers modeled by oligomers and of fullerene derivatives using DFT calculations where the calculated vibrational properties were obtained in a gas phase. It would be valuable to perform vibrational calculations on the crystal unit cell of the polymer:fullerene blend with periodic boundary conditions. This could yield features that cannot be captured by simulations of individual molecules, and therefore aid in the understanding of the complicated spectroscopic changes observed in the blends.

(iv) In the polymer:fullerene blend, there might occur some degree of ground-state charge transfer (CT) arising from overlaps of the wavefunctions between the polymers and fullerenes. Future theoretical studies will have to evaluate the amount of charge transfer in the PBTTT-$C_{14}$:$PC_{71}BM$ blend and other systems. Two approaches can be used to obtain the degree of charge transfer: one is based on the evaluation of the transfer integral representing the intermolecular overlap of electronic wavefunctions between the polymer and $PC_{71}BM$; the other is based on the evaluation of the optical charge-transfer transitions performed in the framework of the generalized Mulliken-Hush (GMH) model. Such theoretical results would provide an important description of ground-state charge transfer in polymer:fullerene blends and help in determining the origin of the spectroscopic changes upon blend formation.